HIGH MANGANESE PRESS HARDENABLE STEEL FOR AUTOMOTIVE SAFETY APPLICATIONS

HIGH MANGANESE PRESS HARDENABLE STEEL FOR AUTOMOTIVE SAFETY APPLICATIONS

By

SARA KHEIRI

A Thesis

Submitted to the School of Graduate Studies

In Partial Fulfillment of the Requirements

For the Degree

Master of Science

McMaster University

McMaster University	Master of Science (2023)
Hamilton, Ontario	(Materials Science & Engineering)

TITLE:	High Manganese Press Hardenable Steel for Automotive Safety Applications
AUTHOR:	Sara Kheiri, B.Sc. (University of Tehran)
SUPERVISOR:	Dr. Joseph R. McDermid
NUMBER OF PAGES:	vii, 107

Lay Abstract

The forming process of the steels used in the automotive industry is not suitable for zinc coatings because it requires pressing at high temperatures to ensure obtaining strong steels. Thus, zinc coatings cannot be utilized despite the desirable cathodic corrosion protection properties they can provide. This study aimed to determine a suitable process window for a zinc-coated prototype steel that would have both high strength and desirable corrosion protection. The zinc-coated prototype steel was pressed at lower temperatures. It was observed that the target mechanical properties were met for all the temperatures tested. Moreover, robust cathodic corrosion protection is expected for all the temperatures. Furthermore, pilot-scale tests yielded comparable results to those obtained in the laboratory, indicating that this process can be successfully applied in the industry as it possesses a sufficiently large process window.

Abstract

In recent years, there has been an increase in the use of press hardened steel (PHS) in the body-in-white of automobiles, namely in parts such as side impact beams, roof rails, engine firewalls, and the floor area. As these parts are expected to possess corrosion resistance, Al-Si coatings are utilized on them. The implementation of Zn coatings is limited, despite possessing improved corrosion resistance attributed to cathodic corrosion protection, due to the detrimental effects of liquid metal embrittlement (LME) and microcracking. LME can be mitigated if stamping occurs at a temperature lower than the Fe-Zn peritectic temperature of 782 °C, as this ensures that the conditions of LME are not met and the cathodically-protective Γ-Fe_3Zn_{10} phase is formed. The objective of this work was to determine a process window for stamping at lower temperatures for a GA80-coated prototype steel (steel K) with the composition of 0.19C-1.92Mn-0.20Si-0.003B-0.03Ti (wt.%). The target mechanical properties in this process window were UTS ≥ 1400 MPa, and YS ≥ 1000 MPa. To achieve robust cathodic corrosion protection, more than 15 vol% of Γ-Fe_3Zn_{10} in the coating was desired. Furthermore, it was aimed to determine the robustness of this process and the industrial feasibility of it through pilot-scale trials for the GA80-coated prototype steel.

To this end, a bare prototype steel (steel I) with the composition of 0.20C-1.96Mn-0.25Si-0.003B-0.01Ti was compared to GA-coated steel K. It was found that stamping a direct hot press forming (DHPF) temperature of 650 °C produced similar mechanical properties such as tensile strengths and ductilities. Microstructural analysis of laboratory-scale DHPF for steel K showed that both the coating and the substrate microstructures were not a strong function of the DHPF temperatures of 550 – 700 °C. The substrate predominantly consisted of martensite with small amounts of ferrite and the coating consisted of α-Fe(Zn) and ≥ 15 vol.% Γ-Fe_3Zn_{10}. Based on the fraction of Γ-

Fe_3Zn_{10} and the coating thickness, robust cathodic corrosion protection is expected from GA80-coated steel K. Furthermore, no evidence of LME or severe microcracking was observed in the microstructure for DHPF temperatures of 550–700 °C for steel K and ductile fracture was observed in tensile coupons. Tensile testing for laboratory-scale DHPF for steel K showed that the mechanical properties such as YS, UE and PUE were not significantly affected by DHPF temperatures of 550-700 °C. Moreover, the targets of UTS ≥ 1400 MPa, and YS ≥ 1000 MPa were met for all DHPF temperatures of 550 – 700 °C. Through pilot-scale tensile testing of steel K, it was determined that the targets for tensile strengths (UTS and YS), were achieved across various conditions involving austenitization at 890 °C for 60 – 240 s and DHPF temperatures ranging from 550 – 700 °C. These findings strongly suggest that industrial feasibility is attainable for DHPF of GA-coated steel K at lower temperatures, enabling the attainment of desirable mechanical properties and robust corrosion protection. Thus, it can be concluded that the process window yielding desirable properties for steel K was determined to be austenitization at 890 °C for 60 – 240 s and DHPF temperatures between 550 – 700 °C.

Acknowledgements

First and foremost, I am incredibly grateful for the invaluable guidance and mentorship provided by my supervisor, Dr. Joseph McDermid. His support and expertise have been instrumental in navigating challenges in my project. It was an honor and pleasure to be able to work with such a talented professor on this research. I would also like to express my appreciation to Dr. Hatem Zurob for his continuous guidance and insightful feedback which has greatly contributed to the quality of my research. I would like to thank Dr. Joey Kish for his helpful comments throughout this project.

I extend my sincere thanks to the dedicated individuals at McMaster who have trained me in various facilities. I would like to thank Dr. Mike Bruhis for helping me operate facilities at the mechanical testing laboratory and his constructive feedback. I want to genuinely thank Bita Pourbahari for helping me with cold rolling and providing helpful input for my research. Additionally, I express my appreciation to Chris Butcher and Jhoynner Martinez from CCEM for my training in SEM techniques. I acknowledge Victoria Jarvis and Dr. Jim Britten for their support and training in XRD. I would like to thank Dr. Beth McNally for dilatometry training and all her support. I am grateful for my colleagues at CAMC for their valuable feedback, and their unwavering support throughout my project.

I would also like to acknowledge Gestamp for their collaboration and execution of pilot-scale trials. The financial support from International Zinc Association – Galvanized Autobody Partnership (IZA-GAP) and the in-kind donation of galvannealed prototype steel (K) from Voestalpine have also been instrumental in the success of this project. Furthermore, I extend my appreciation to US Steel for their supply of prototype steel (I).

Last but not least, I would like to deeply thank my parents and my sister for their constant support through daily calls during my years studying abroad. I would also like to thank my friends for empowering and encouraging me.

Table of Contents

Table of Figures

List of Tables

1 Introduction

There has been an increase in the utilization of ultra-high strength steels (UHSS) in the body-in-white (BIW) of cars, aiming to optimize crash resistance to promote passenger safety, and enhance fuel efficiency by reducing CO_2 emissions through their lighter weight. UHSSs are primarily used for structural reinforcement and anti-intrusion components, including side impact beams, roof rails, engine firewalls, and the floor area [1], [2]. The 2021 Ford Mustang Mach-E BIW [3], shown in Figure 1.1, is a prime example of this trend where the utilization of advanced high strength steels (AHSSs) and press hardening steels (PHSs) is significant in areas such as A-pillars and B-pillars.

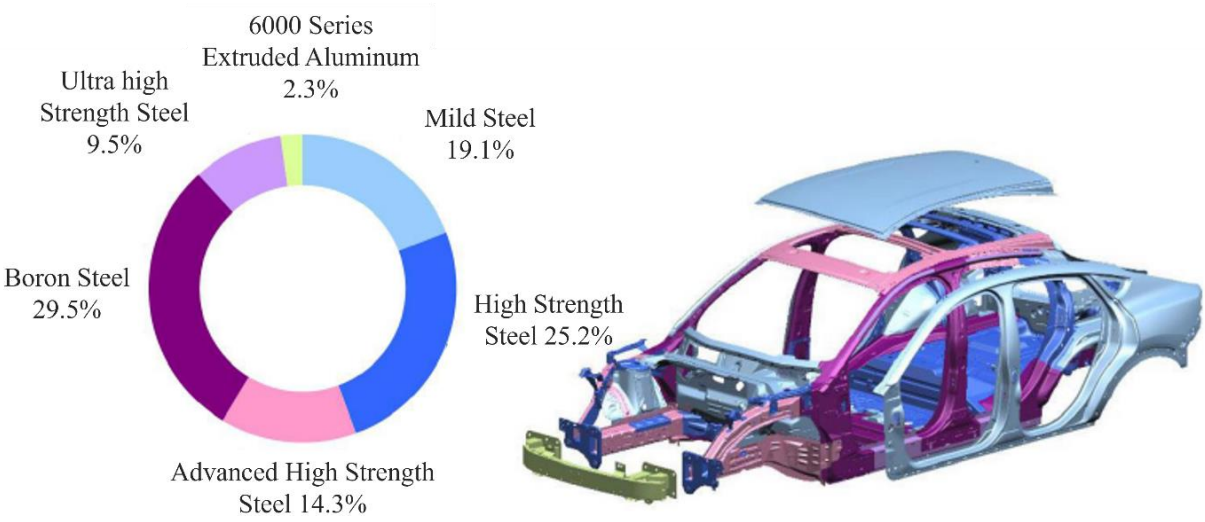

Figure 1.1: Advanced high strength steels (AHSS) and press-hardened martensitic steels (labelled boron steel) use in the 2021 Ford Mustang Mach-E BIW [3].

Martensitic steels, produced through direct hot-press forming (DHPF), have become a popular choice enabling the production of complex shapes with minimal spring back. Currently, the most widely utilized grade for the DHPF process is 22MnB5, which has a standard composition of 0.22C-1.2Mn-0.25Si-0.005B (wt.%) [2]. DHPF consists of two main steps of austenitization, and press forming. Austenitization is usually performed in a furnace under ambient atmosphere at

temperatures between 850°C-950°C. After austenitization, the parts are transferred to a water-cooled die set, where they undergo simultaneous stamping and die quenching with cooling rates exceeding 75 °C/s [4]. The transfer typically occurs as quickly as possible, and the blank temperature does not decrease significantly prior to forming and quenching. The resultant microstructure consists of lath martensite with small fractions of ferrite [5].

One of the key considerations in automotive applications is having corrosion resistance without compromising structural integrity. Thus, PHS commonly possesses a metallic coating to attain corrosion protection by leveraging both barrier type and cathodic protection mechanisms. Al-Si alloys with near-eutectic compositions of 7-11 wt.% Si are presently the most commonly used coatings for 22MnB5 [2], [6]. When subjected to DHPF, Al-Si coatings react with the substrate and form layers of brittle intermetallics. Since these intermetallics are brittle, they are prone to cracking during press forming which exposes the substrate to the environment [2], [7], [8]. These microcracks significantly reduce the corrosion resistance as Al-Si intermetallics can only provide barrier corrosion protection. Consequently, the utilization of PHS in corrosion prone areas of the BIW, where cathodic corrosion resistance is necessary, is prevented. Thus, there is a demand for coating systems that can deliver both barrier and cathodic protection [2], [4].

Zn-based coatings are known to provide cathodic corrosion protection for steel substrates. However, their utilization in DHPF is avoided due to the relatively low melting temperature of zinc, which can result in liquid metal embrittlement (LME) [9], [10]. During austenitization, the Zn coating alloys with the substrate and transforms into a Zn-enriched ferrite (α-Fe(Zn)) solid solution layer, a Zn-rich Fe-Zn liquid ($Zn(Fe)_{liq}$), and an oxide layer on the surface of the coating [2], [6]. During press forming, the coating possesses $Zn(Fe)_{liq}$ which can cause LME and thus, catastrophic brittle failure. Furthermore, the coating undergoes the Fe-Zn peritectic reaction of

$\alpha\text{-Fe(Zn)} + \text{Zn(Fe)}_{liq} \rightarrow \alpha\text{-Fe(Zn)} + \Gamma\text{-Fe}_3\text{Zn}_{10}$ upon quenching [2], [11]. If the austenitization time is extended to eliminate the presence of the liquid alloy, the robustness of cathodic corrosion protection may be compromised as it has been stated that a volume fraction of at least 15% Γ-Fe_3Zn_{10} is necessary for robust cathodic corrosion protection [12], [13]. LME can be effectively mitigated, while still maintaining robust cathodic corrosion protection, by intentionally extending the transfer time from the austenitization furnace to the forming dies [14]–[16]. This deliberate extension eliminates the liquid alloy during the forming process as it goes through the peritectic reaction for form Γ-Fe_3Zn_{10}. However, to obtain a fully martensitic microstructure with optimal mechanical properties, it is necessary to utilize grades that have increased hardenability [15], [17].

The objective of this research was to determine the feasibility of using an extended transfer time for a GA-coated prototype PHS steel with an increased Mn content, the composition of which was 0.19C-1.92Mn-0.2Si-0.003B (wt.%). To this end, it was aimed to establish a process window and determine the potential for scaling through pilot-scale trials. The main target properties for this alloy were to have a fully martensitic substrate which would reach an ultimate tensile strength (UTS) of ≥ 1400 MPa, and a yield strength (YS) of ≥ 1000 MPa. Additionally, it was aimed for the coating to provide robust cathodic corrosion protection by containing ≥ 15 vol% Γ-Fe_3Zn_{10} in the final coating microstructure. Firstly, The DHPF properties of the GA-coated steel were compared to a bare prototype steel with a composition of 0.20C-1.96Mn-0.25Si-0.003B-0.01Ti (wt.%). Then, the mechanical properties of the GA-coated steel were evaluated by tensile testing and correlated with the microstructural evolution of the substrate as a function of DHPF temperature. Furthermore, the mechanical properties of pilot-scale trials were compared to the laboratory-scale testing. Subsequently, the potential of providing robust cathodic corrosion

protection for the coating was determined for laboratory-scale tests for the GA-coated steel and related to the coating microstructure.

2 Literature Review

2.1 Press Hardening Steel

In order to optimize car body design for crash resistance and weight reduction, the automotive industry has increasingly turned to high strength steels in critical structures such as side impact beams, roof rails, engine fire walls and the floor area. While traditional approaches using thicker gauge medium-high strength steels have resulted in excessive weight and packaging issues, the utilization of ultra high strength steels has allowed for the use of thinner gauges and the omission of reinforcements. These steels not only satisfy safety standards for crash performance, but also environmental regulations pertaining to fuel efficiency and CO_2 emissions due to their lower weight. Martensitic steels, produced through hot stamping, have become a popular solution due to their high strength and formability, enabling the production of complex structural components with minimal spring back. The hot stamping process, which is explained in §2.3, involves two critical steps: austenitization and press forming. Initially, the blanks are heated in a furnace to reach full austenitization, and subsequently, are shaped using press forming.

Currently, the 22MnB5 family of alloys, a boron steel also known as carbon–manganese–boron low alloy steel, are used in the industry [1], [2], [6]. Other alloys based on 22MnB5 have been developed for these applications. Most notably, ArcelorMittal has developed an Al-Si coated boron steel (22MnB5) commercialized under the trade name of Usibor 1500P [18]. The composition of 22MnB5 can be seen in Table 2.1[2]. The primary alloying elements of 22MnB5 are C, Mn, Si, B, and Cr [19]. The low carbon and alloy content, which is a defining feature of boron steels such as 22MnB5, can provide economic benefits and facilitate cold and hot formability, coatability, and weldability [6]. The effects of alloying elements on the 22MnB5 CCT diagram can be seen in Figure 2.1. These effects are discussed below.

Table 2.1: Chemical composition of 22MnB5 hot stamped steel (wt.%) [2].

	C	Si	Mn	Cr	B	Al	Ti
22MnB5	0.22	0.23	1.20	0.16	0.005	0.04	0.03

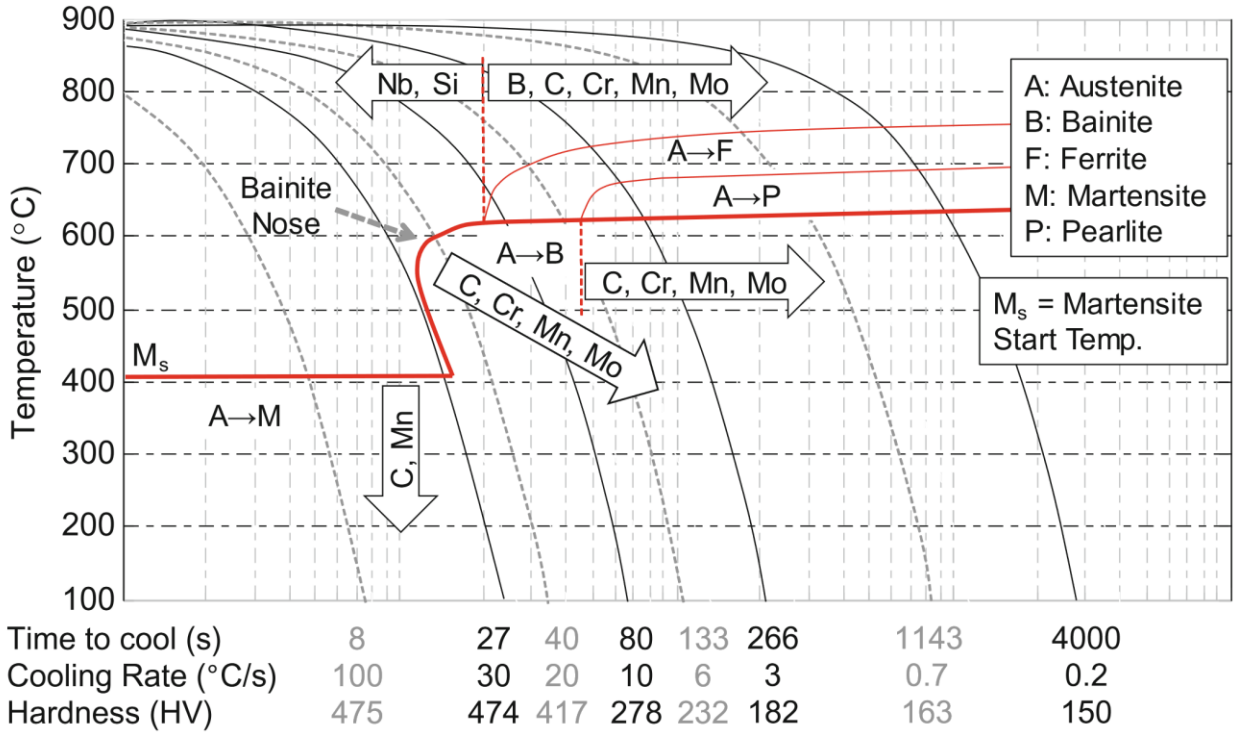

Figure 2.1: Effects of alloying elements on CCT diagram for 22MnB5 steel [8].

The strength and hardness of 22MnB5 can be controlled by adjusting its carbon content. However, an increase in carbon content can lead to reduced weldability and ductility [1], [8]. Additionally, a higher carbon content reduces the critical cooling rate required for full martensitic transformation. Carbon also acts as an austenite stabilizer and strengthens the martensite via interstitial solute strengthening [2]. A Mn addition greatly impacts phase transformation temperatures, which can be seen in Figure 2.1. Mn reduces martensite-start temperature similar to C, but it should be noted that it is not as effective. Mn addition can retard bainite formation if the

carbon level is low. However, it is important to note that high amounts of Mn can promote macro-segregation. This causes banding in the microstructure where ferrite and pearlite grains appear as layers. This can have a negative impact on the mechanical properties [11], [20]. Cr increase hardenability, as shown in Figure 2.1, without having an adverse effect [6], [8], [11]. Moreover, the addition of Mn reduces the austenitization temperature, thereby potentially enabling lower furnace temperatures in the hot stamping process. This could result in energy savings and reduced carbon emissions during heating [8], [11]. It is worth noting that Mn additions exceeding 5 wt.% lead to the development of a complex microstructure with austenite present at room temperature. Thus, it can be observed that the typical Mn content of steels employed in hot stamping falls within the range of 0.8 to 1.3 wt.%, with 1.2 wt.% being the most commonly used concentration [8].

Boron is the most efficient element in increasing the hardenability of steel [8], [21], [22]. As shown by Figure 2.1, the addition of B delays the formation of ferrite and pearlite considerably. Similar effects have also been observed for the austenite to bainite transformation. About 10 to 20 wt. ppm addition of B in low-C steels improves the hardenability considerably [23], [24]. For example, such a small addition of B is equivalent to the addition of 0.4 % Cr, or 1.25 % Ni (all in wt.%) in enhancing the hardenability of a 0.4 wt. % C steel. Thus, B is a cost-effective element for increasing the hardenability of steel [24]. The mechanism responsible for this strengthening phenomenon is currently the subject of research. However, it is generally accepted that solute boron in an austenite solid solution segregates to austenite grain boundaries. The presence of B in the grain boundary reduces its surface energy; thus, increasing the activation energy for nucleation in the grain boundary on cooling. This effect retards ferrite nucleation and, therefore, increases the hardenability [25]. Moreover, research has shown that having small amounts of carbo-boride precipitation $Fe_{23}(C,B)_6$ plays a role in retarding ferrite nucleation as well. Although it should be

noted that its effect is not as pronounced as some models have suggested and it should not exceed a certain amount [24], [26], [27]. Carbo-boride precipitation suppresses ferrite nucleation through the nucleation site competition mechanism [24]. In order to ensure that B stays in solid solution instead of forming BN, Ti and Al are added. They form TiN and AlN instead of BN [6].

The addition of chromium as an alloying element serves to enhance hardenability of the press-hardenable steel. Niobium can inhibit grain growth during austenitizing if Nb(CN) is formed, which enhances strength and toughness in low carbon steels as it affects the prior austenite grain size (PAGS) [8]. During the steel-making process, silicon is commonly used as a deoxidizer. This addition can lead to solid solution strengthening on the ferrite phase [8]. Research has indicated that high levels of silicon concentration can result in selective oxidation during galvanizing. This, in turn, reduces the reactive wetting of the zinc coating, leading to poor adherence of the coating [4]. Aluminum is an effective element for inhibiting austenite grain growth during the heating process before quenching, particularly when compared to other elements such as Ti that have similar effects [8].

2.2 Continuous Galvanizing

The majority of zinc-coated sheet products are produced through Sendzimir-type hot-process continuous coating lines, thoroughly explained by Marder [28]. A schematic of this process is presented in Figure 2.2 [29]. This process includes a cleaning section, which is not included in this schematic, prior to the heating and dipping section. However, to promote coating adherence and to prevent contaminants, particularly iron fines, from infiltrating the galvanizing bath, steel sheets are typically subjected to a pre-cleaning process.

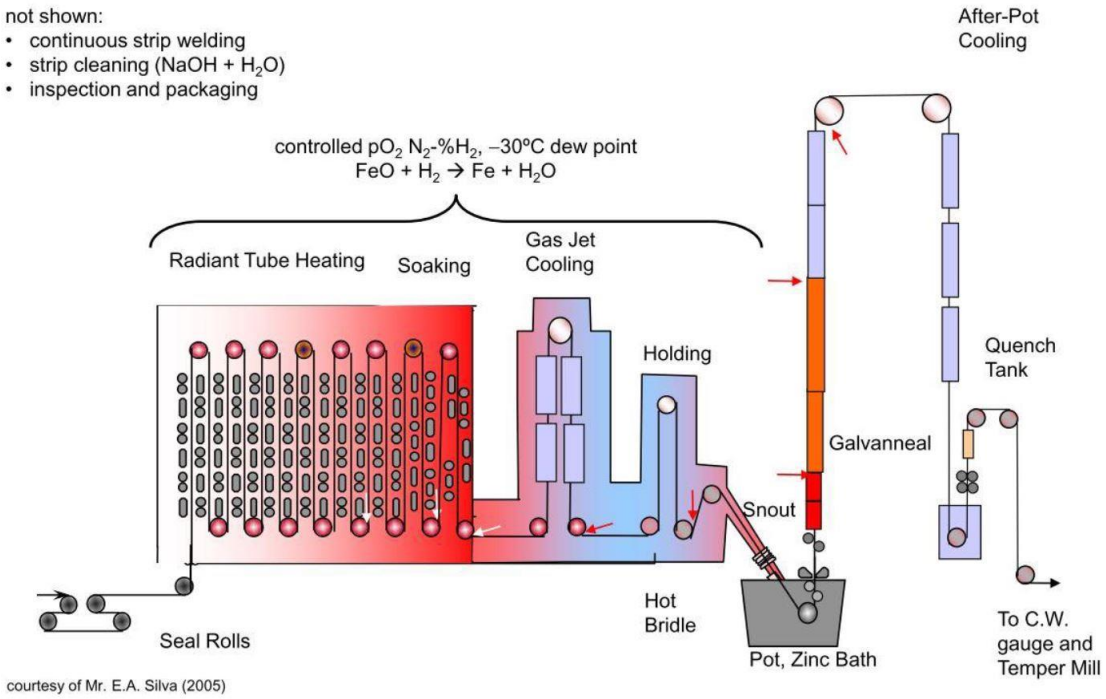

Figure 2.2: Schematic of a continuous galvanizing line [29].

Following cleaning, the sheet is transported to the heating and holding zones of the furnace, where it is annealed at a temperature above the recrystallization temperature of the steel (usually exceeding 700 °C) to produce the desirable ferrite-pearlite microstructure. To achieve full recrystallization at faster line speeds, higher annealing temperatures would be necessary. The process uses a N_2/5-20 vol% H_2 atmosphere with a regulated dewpoint (or the partial pressure of water vapor (pH_2O)) of between –30°C to –10°C. During this step, oxidation products such as Fe-oxide and Fe-hydroxide will be reduced; however, selective surface oxidation of alloying elements (such as Mn, Si, Al, V, and Ti) will occur. For example, in the case of Mn, the resultant MnO surface oxide layer can directly affect reactive wetting. In other words, these oxides might interfere with the coating process [28].

After leaving the furnace, the strip is exposed to a gas jet cooling section which has the capability of rapidly reducing the strip's temperature at 15-20 °C/s to the zinc bath temperature, which is 460

°C for galvanized coatings [28], [30]. To promote the formation of the necessary $Fe_2Al_5Zn_x$ interfacial layer that inhibits the formation of brittle Fe-Zn intermetallics, a small amount of Al (typically 0.2 – 0.3 wt.%) is added to the bath [28], [31], [32]. In the next step, planar gas jet streams (commonly referred to as air knives) use high-pressure air or nitrogen to remove excess coating, achieving the desired coating thickness. The achieved coating is a typical galvanized coating which only needs to be cooled and coiled. For the case of galvannealed coatings, an additional heat treatment step is required which is usually carried out in an induction furnace with a holding section. Important process parameters in the galvannealing step are heating rate, holding temperature and cooling rate. In a typical galvannealing furnace, a heating rate of 15 °C/s is used to achieve the holding temperature of 500 °C for about 8-9s. The strip is then cooled by air coolers to a temperature below 350 °C at a rate over 17 °C/s to produce the desired microstructure [28].

2.3 Hot Press Forming

Hot press forming (HPF), also known as press hardening, is a forming technique that has garnered significant attention in the production of advanced high strength steels (AHSSs) for automotive applications. HPF can be divided into two categories: direct hot press forming (DHPF), and indirect hot press forming. Each of these comprises an austenitization and quenching step to achieve the desired microstructure in the HPF component. A schematic of these two can be seen in Figure 2.3 [1]. This section aims to discuss these routes.

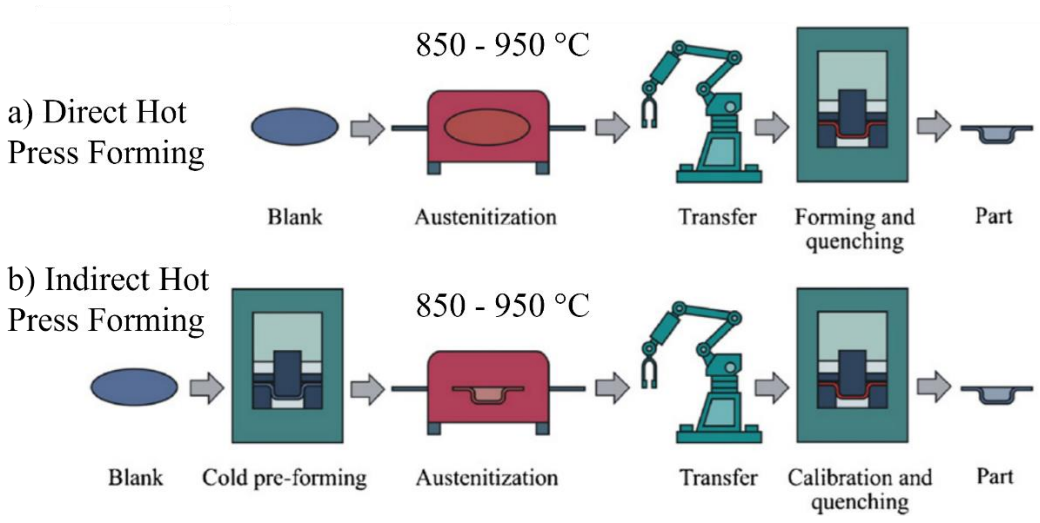

Figure 2.3: Hot press forming routes (a) direct (or DHPF) (b) indirect [1].

The target mechanical properties of the final product for 22MnB5 are ultimate tensile strength (UTS) of ≥ 1500 MPa and total elongation (TE) of 5-7 % [2], [5], [6], [25]. Thus, the desired final substrate microstructure is martensite which can achieve the mechanical properties targets. Figure 2.4 shows the substrate microstructure before and after HPF. As can be seen in Figure 2.4 (a), the initial microstructure consists of ferrite and pearlite that is likely elongated as a result of prior cold rolling [1], [33]. The initial microstructure has a moderate strength with UTS = 600 MPa and 25% elongation [2]. The desirable fully martensitic final microstructure is shown in Figure 2.4 (b). In some instances, for example if cooling is not uniform or if the cooling rate is not high enough, ferrite islands can appear in the substrate. If the ferrite content is high enough, UTS decreases; therefore, it is not desirable [5], [25].

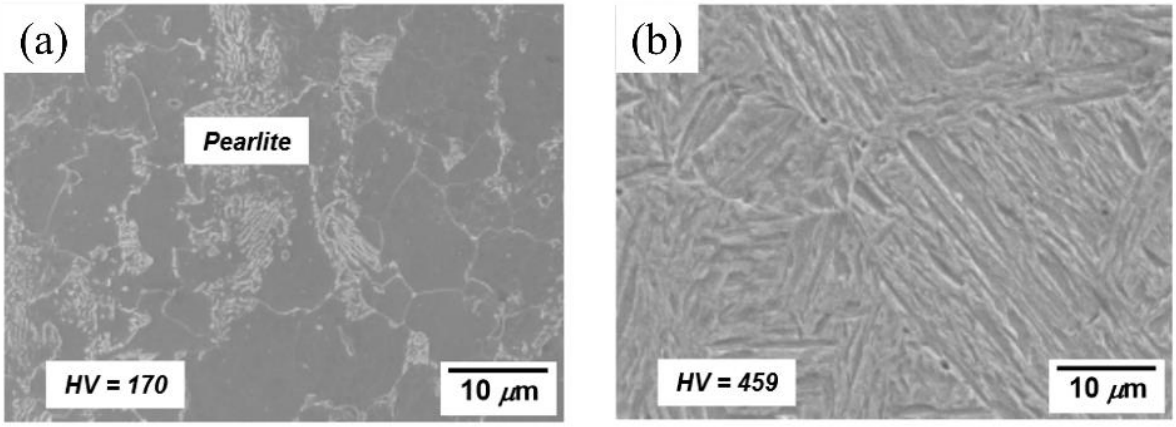

Figure 2.4: Substrate microstructure (a) before HPF (ferrite and pearlite), (b) after HPF (martensite) [5].

2.3.1 Direct Press Forming

In the DHPF process, Figure 2.3 (a), the blank initially enters the austenitization furnace. The main goal of this step is to achieve a fully austenitic microstructure. Austenitization is commonly carried in a roller hearth furnace with a temperature of 850-950°C. The specific parameters used here, such as temperature and time, are dependent on the composition of the steel being press hardened. Austenitization temperature can be determined using dilatometry, from which Ac_1 and Ac_3 temperatures can be calculated. It has been discovered that an austenitization temperature of 850 – 950°C is needed to obtain a fully austenitic microstructure for the frequently utilized hot stamping grade, 22MnB5 (composition outlined in Table 2.1) [1], [34]. The austenitization duration can be determined based on the blank's thickness [1], [34]. Austenitic microstructures at 850 – 950°C are more ductile than ferrite-pearlite structures, resulting in greater steel formability and less spring back, leading to more precise shaping [1], [8].

The blank is, subsequently, transferred to water cooled dies, where it is simultaneously formed and quenched. Thus, it both acquires the desired shape and a martensitic microstructure in one step.

The important process parameter is the cooling rate. To obtain a fully martensitic microstructure exhibiting the desired mechanical properties (UTS≥ 1500 MPa) a critical cooling rate must be met. The critical cooling rate for a specific alloy can be determined via its CCT diagram. Some researchers have mentioned that a minimum critical cooling rate of –27°C/s is enough for 22MnB5 [1], [8], [35]–[37], although others agree on a higher cooling rate of –50 °C/s [11], [38]. This rate should be fixed in a manner that avoids bainitic transformations as well. Hence, a cooling rate of –75 °C/s is the most reliable option [38].

2.3.2 Indirect hot press forming

Indirect hot press forming can be seen in Figure 2.3 (b). As can be seen in this figure, the blank is initially cold formed to approximately 90-95% of its desired final shape before being placed in the austenization furnace, which typically has a temperature of 850-950 °C [5]. The most significant advantage of this method is that a large portion of the deformation is carried out at room temperature, primarily on the highly ductile pure Zn coating. This eliminates the presence of liquid during forming, effectively preventing the occurrence of LME. The pre-forming stage also enables the production of more intricate and larger parts. As the part is almost completely formed when it reaches the forming and quenching dies, the contact and heat conduction are improved, leading to better temperature homogeneity during quenching. In addition, the indirect approach results in lower levels of high temperature deformation of the coating, potentially reducing coating cracks [16].

Nevertheless, this processing technique is not commonly utilized due to several drawbacks that outweigh its benefits [5]. The additional forming step necessitates more time and cost since an extra die set must be produced and maintained [4]. Moreover, conducting the forming step at room

temperature restricts the material to conventional cold forming boundaries, nullifying one of the primary advantages of press hardening [28].

2.4 Coatings for Press Hardening Steels

Originally, bare steel was used in hot stamping. In this case, iron oxide scale forms after press hardening, which adversely affects the heat transfer between the steel and the dies. The oxide scales increase the friction between the steel and the dies and can damage dies by attaching to them. After HPF, the scale needs to be removed either manually or by shot blasting or peening, depending on the shape of the final part [2]. Due to this inconvenience and the need for corrosion protection in the BIW of cars, coated steels are utilized. Usibor® Al-(9-11 wt.%)Si, introduced by ArcelorMittal, is a frequently employed metallic coating for hot stamped components [2], [39]. However, there has been increasing interest in the utilization of Zn coatings owing to their capability of providing more robust corrosion protection in comparison to Al-Si coatings [4], [39]. Thus, it is important to understand the impact of press hardening on each of these coatings.

2.4.1 Al-Si Coatings

Currently, there are two primary categories of industrially produced hot-dipped aluminized coatings. Type 1 aluminized coating is commonly used on hot stamped steel, automotive exhaust systems, and heat shields as it offers resistance to both corrosion and elevated temperature oxidation . The coating consists of an Al–Si alloy with a near-eutectic composition containing 7–11 wt.% Si. Type 2 aluminized coating is pure Al, without Si addition. This type is mostly used in building cladding panels, because its surface is highly reflective [2], [40]. Type 1 is of interest for the purposes of this study.

The common practice for aluminizing 22MnB5 steel involves immersing it in a molten aluminum alloy bath at approximately 675 °C. The bath typically consists of 88 wt.% Al, 9 wt.% Si, and 3

wt.% Fe with the Si serving to create a τ_5-Fe_2SiAl_7 inhibition layer at the interface between the coating and the substrate. A microstructure of a type 1 aluminized coating highlighting the inhibition layer is showed in Figure 2.5 (a) [2]. This layer prevents the rapid formation of Fe_2Al_5 during the aluminizing process and inhibits the formation of intermetallic phases at temperatures below 550 °C. However, because DHPF is carried out at higher temperatures, the Fe-Al reaction can occur. In the absence of an inhibition layer, Fe_2Al_5 intermetallic can grow into the substrate resulting in a wavy interface which affects coating adhesion [2], [40], [41].

Figure 2.5 (b) shows an aluminized microstructure after annealing at 930 °C for 5 min and rapid quenching. The layer on top of the coating, marked with a rectangle, is an Al_2O_3 layer which acts as a barrier preventing further oxidation. The initial layer is $FeAl_2$, which forms due to the transformation of Fe_2Al_5 with increasing Fe content in the coating. The second layer is identified as τ_1-Fe_2SiAl_2, which also appears as particles in the first layer. The third layer is identified as $FeAl_2$, and the fourth layer is similar to the second layer. The fifth layer, known as the diffusion layer, has an increasing Fe content towards the substrate steel. Moreover, Figure 2.5 (b) reveals the presence of several Kirkendall voids, which can be attributed to the diffusion of Al atoms either inward or outward [2], [7], [42], [43].

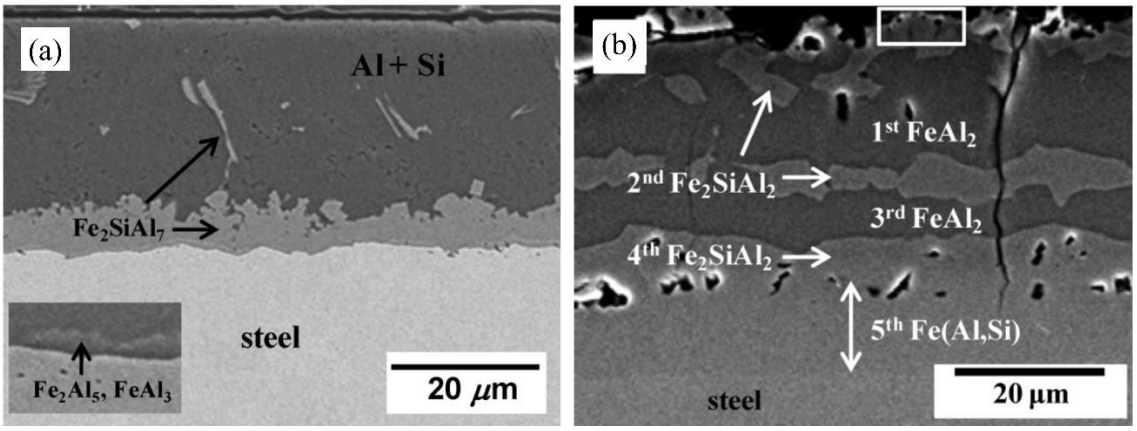

Figure 2.5: Cross-sectional SEM micrographs of (a) type 1 aluminized sample (b) aluminized sample heated at 930 °C for 5 min with a heating rate of 10 $°Cs^{-1}$ in air [2].

Corrosion protection of this alloy is linked with the layers described. The first and third $FeAl_2$ layers have slightly lower electrochemical potentials in comparison to the substrate steel. However, the entire coating exhibits an electrochemical potential similar to that of the substrate. Hence, it only provides barrier corrosion protection, and cannot provide robust cathodic corrosion protection. The uncoated areas such as cut edges are a potential drawback as they are not protected [2], [4], [39].

Moreover, studies have shown that laser welded Al-Si coatings can cause ferrite formation in the martensite substrate in DHPF. The coating melts and alloys with the molten weld pool during welding, which in turn causes the formation of ferrite islands in the martensite matrix during the austenitization step in DHPF. Studies have suggested that in-situ alloying of ferrite suppressing carbides and austenite stabilizing elements in electro-spark deposition, an additive manufacturing technique, prior to laser welding can mitigate this issue [44].

2.4.2 Zinc Coatings

Galvanized (GI) or galvannealed (GA) coatings are used on cold rolled sheet steel because of their appearance, adequate formability, physiological harmlessness and, most importantly, their excellent barrier and cathodic corrosion protection [2]. Moreover, it has been shown that galvanized PHS has greater hydrogen embrittlement resistance in comparison to Al-Si coatings due to the Zn coating effectively preventing hydrogen uptake and inhibiting the hydrogen generation reaction and transport [45]. Galvanized coatings, such as GI70, usually have a coating weight of 70 g/m^2. This coating weight is equivalent to a coating thickness of approximately 10 μm [46]. After undergoing continuous hot dip galvanizing, GI coatings are primarily composed of nearly pure zinc. However, there are also minor quantities of iron in the solid solution (known as η-Zn) present within the coating. Whereas GA coatings have a more complex microstructure of Γ-Fe_3Zn_{10}, δ-$FeZn_{10}$, or ζ-$FeZn_{13}$ phases based on the amount of alloying elements [28], [47].

These coatings are mostly used in indirect press hardening as opposed to DHPF because of the austenitization step of the process [4]. Since the austenitization temperature in DHPF is higher than the Fe-Zn peritectic temperature of 782 °C, Figure 2.6, the coating melts and is replaced by Fe-Zn intermetallic compounds by reacting with the substrate [2], [4], [48]. Thus, the microstructural evolution of the coating during austenitization is of interest. Moreover, if stamping happens at temperatures above the peritectic temperature, liquid metal embrittlement (LME) can occur [49]. This phenomenon will be discussed in §2.5.

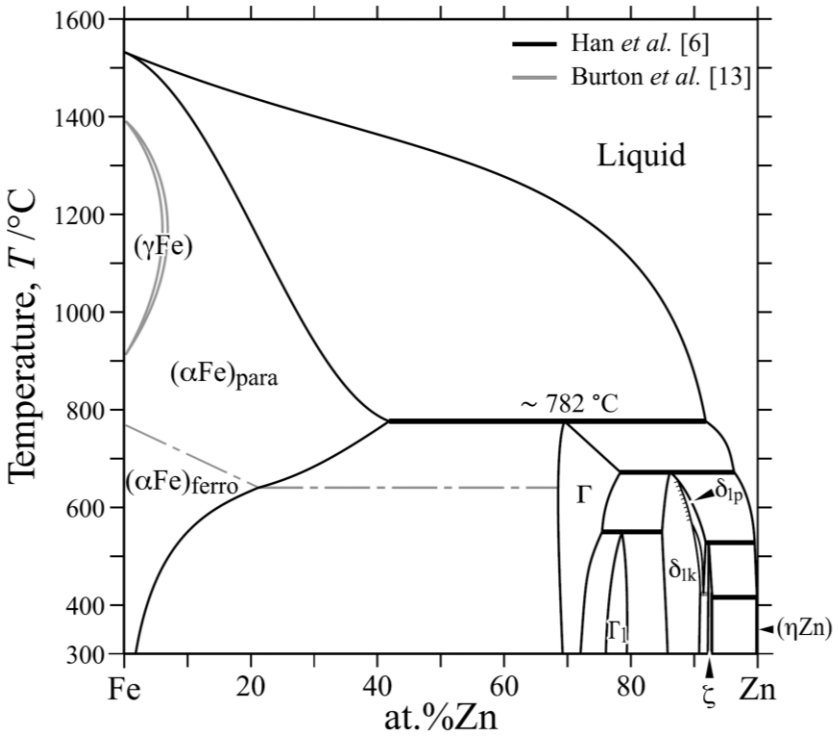

Figure 2.6: Fe-Zn phase diagram [48].

Figure 2.7 shows microstructural evolution of a GI 22MnB5 coating with a substrate thickness of 1.5 mm and an average coating weight of 70 g/m^2 during austenitization. The SEM images correspond to a temperature range of 400-900 °C without soaking quenched in water. The heating rate used was 4–7 °C/s, therefore, it should be emphasized that the changes that occur in phases at those temperatures cannot be accurately predicted by relying exclusively on thermodynamics [50]. As can be seen in Figure 2.7, the coating initially consists of η-Zn. The $Fe_2Al_{5-x}Zn_x$ inhibition layer starts breaking down at 400 °C and finishes transforming at 450 °C. This layer is destroyed by the ζ-$FeZn_{13}$ phase, proved by XRD [50]. At 500 °C, the interfacial layer was fully destroyed, and the coating consisted of ζ-$FeZn_{13}$ and δ-$FeZn_{10}$. It can be observed in Figure 2.7 that the coating transformed into δ-$FeZn_{10}$ at 550 °C. As the temperature increased to 600 °C and 650 °C, the coating transformed into a dual-phase composition, combining both δ-$FeZn_{10}$ and Γ-Fe_3Zn_{10}. The

transformation of Γ-Fe_3Zn_{10} was observed to be complete at 700 °C. As the temperature increases, diffusion of Zn into Fe occurs, causing the coating to form a layer of Zn rich Fe phase which is referred to as α-Fe(Zn). Heating above the peritectic temperature of 782 °C causes the coating to undergo the peritectic reaction (Eq. (2.1)), thus being comprised of liquid Zn phase that is rich in Fe and α-Fe(Zn). Upon quenching, the liquid phase turns into Γ-Fe_3Zn_{10}. Thus, Γ-Fe_3Zn_{10} phase can be seen as islands in the α-Fe(Zn) phase [50].

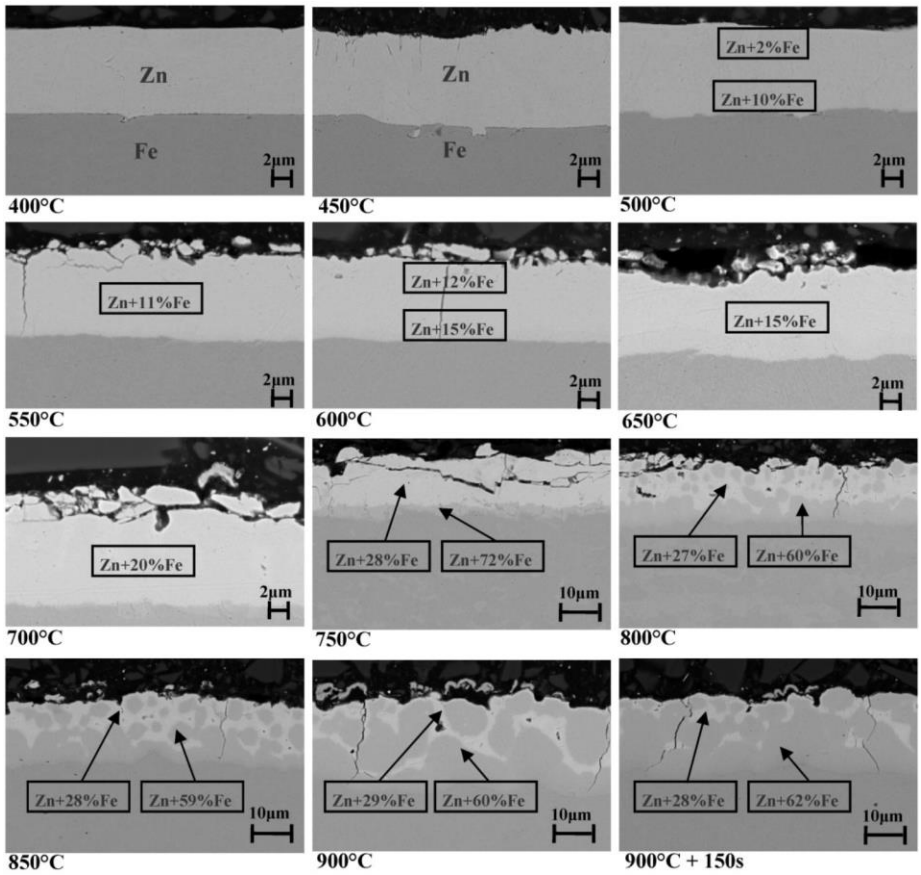

Figure 2.7: Cross sectional SEM micrographs of GI steel after annealing at mentioned temperatures; concentrations are expressed in wt.% [50].

$$\alpha\text{-Fe(Zn)} + \text{Zn(Fe)}_{liq} \rightarrow \alpha\text{-Fe(Zn)} + \Gamma - \text{Fe}_3(\text{Zn})_{10} \quad (2.1)$$

The influence of austenitization time on coating microstructural evolution has been studied by Dever [13]. Figure 2.8 shows bulk composition as a function of austenitization time. It can be seen that annealing for extended times results in further alloying of the coating with the substrate. Figure 2.9 shows the phase fractions of the coating as a function of austenitization time. It can be seen that for extended austenitization times, the amount of Γ-Fe_3Zn_{10} phase decreases rapidly, and the coating is mostly comprised of α-Fe(Zn). The coating is completely transformed into α-Fe(Zn) after annealing 900 °C for 240 s. Further annealing resulted in an increased coating thickness, which adversely affected the mechanical properties by reducing the martensite fraction [13]. Figure 2.10 shows microstructural evolution of GI70 22MnB after annealing at 900 °C for two different temperatures. It can be seen that after 30 s of annealing (Figure 2.10(a)) the coating consisted of mostly α-Fe(Zn) with some Γ-Fe_3Zn_{10}. After 780 s of annealing (Figure 2.10(b)), it has fully transformed into α-Fe(Zn) [51]. These results are in agreement with the results obtained by XRD by Dever [13].

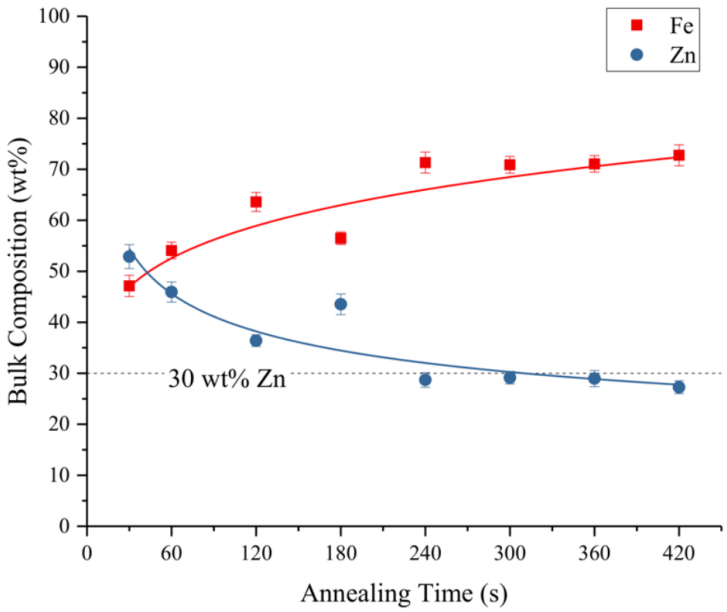

Figure 2.8: Bulk composition of a GI70 coating at 900 °C as a function of austenization time determined by XRD [13].

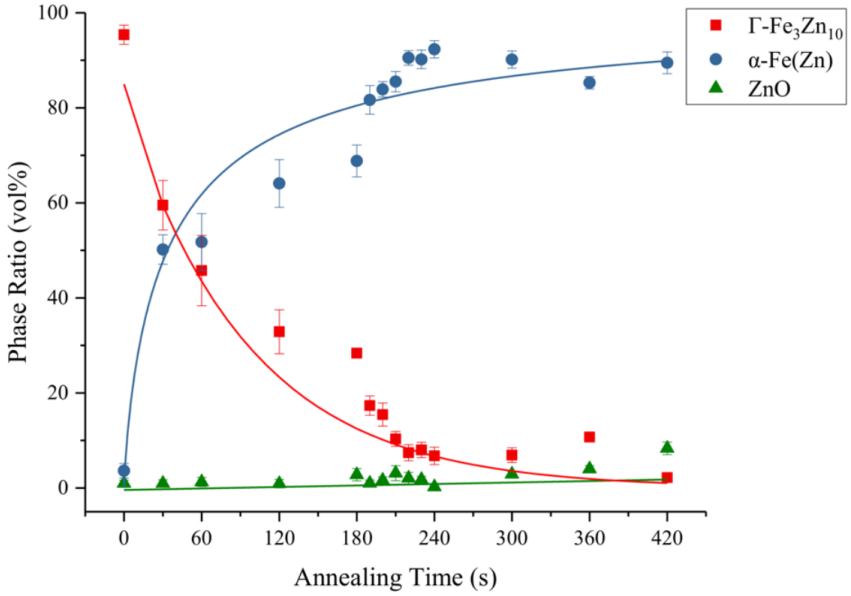

Figure 2.9: GI70 coating phase evolution at 900 °C as a function of austenization time measured by XRD [13].

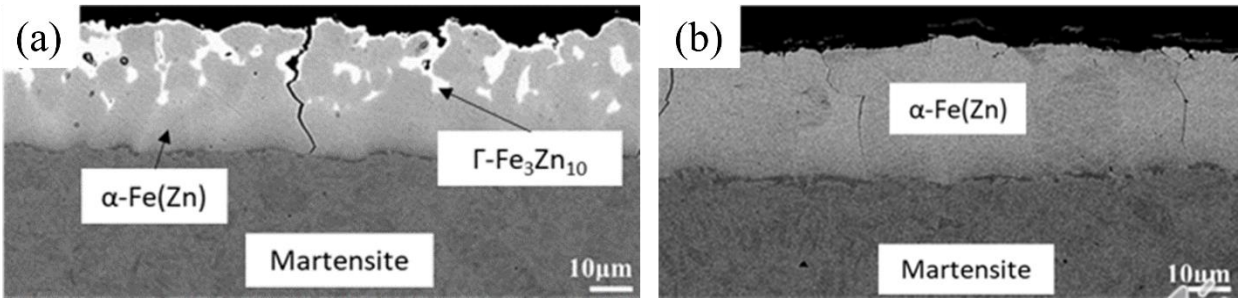

Figure 2.10: Microstructural evolution of GI70 coating (a) austenitized at 900 ℃ for 30 s and (c) austenitized at 900 ℃ for 780 s [51].

2.5 Liquid Metal Embrittlement

Liquid metal embrittlement (LME) is described as brittle fracture or loss of ductility of a metal or alloy due to the penetration of another liquid metal or alloy into its microstructure. This occurs rapidly either along the grain boundaries in polycrystalline materials or along sub-grain boundaries in a single crystal of the material, resulting in transgranular or intergranular decohesion [10]. This phenomenon has been observed in several systems including: Al-Ga, Al-Hg, Fe-Zn, Cu-Hg, Cu-Li, Cu-Bi and Ni-Bi [52]–[57]. In Zn-coated PHS, LME induced cracking can cause catastrophic failure while press forming at elevated temperatures. At those temperatures, Zn can diffuse along the austenite grain boundaries causing a brittle intergranular fracture [34], [58], [59]. Thus, it is important to understand this phenomenon to be able to mitigate it in DHPF.

Various mechanisms have been suggested for LME which can be divided into three different categories: crack tip brittle fracture, dislocation activity, and grain boundary diffusion. They are comprehensively summarized in a variety of reviews [9], [10], [49], [60]. Three requirements are essential for LME. Razmpoosh et al. [9] have expressed these requirements in Figure 2.11 as a susceptible material, tensile stress, and an aggressive liquid metal. Aggressive liquid metal has

also been regarded as grain boundary wetting in the literature [61]. These factors and the role of different variables on them are described in this section.

Figure 2.11: The requirements for liquid metal embrittlement [9]

2.5.1 Susceptible Material

It has been reported that, in a classic LME system, such as Cu-Hg, low mutual solid solubility and a lack of intermetallic compounds is observed [62], [63]. In other words, the metals in the LME system do not form reaction products and enable grain boundary wetting. However, Zn and Fe have significant mutual solubility for the case of zinc coated PHS. According to the Fe-Zn phase diagram in Figure 2.6, below the peritectic temperature of 782 °C several intermetallic compounds are formed, and above this temperature, α-Fe(Zn) in addition to a liquid with high Fe solubility is present, as discussed earlier. Based on these, LME should not occur.

To understand why LME is still present in the Fe-Zn system, the role of alloying elements such as Si should be considered. Small Si additions can significantly reduce the Fe solubility in the Fe-Zn system [64]. The low Fe solubility in the system raises the activity of Zn on both sides of the

substrate/coating interface. It is known that Fe-Zn intermetallic phases have low solubility for Si [64], [65]. Thus, the Si is rejected to the liquid in order for any Fe-Zn intermetallics to form [65]–[68]. As a result, LME will occur in an Fe-Zn system if other conditions of it are met.

Bhatracharya et al. [69] studied the role of Si on Zn-LME susceptibility in AHSS. They used two different AHSS grades with similar compositions except for Si content, with one being 0.98 wt.% and the other being 0.06 wt.%. Figure 2.12 shows a time-of-flight secondary ion mass spectrometry (TOF-SIMS) map for the alloy containing 0.98 wt.% Si. Whereas Figure 2.13 shows TOF-SIMS map for the alloy with 0.06 wt.% Si. By comparing these two maps, Si enrichment in the coating/substrate interface was more significant for the case of the steel with higher Si content, hinting at higher LME susceptibility. Moreover, hot tension tests proved that LME occurred over a broader range of temperatures and strain rates for the steel with a higher Si content, thus further validating the observations. It should be noted, however, that LME was not as strong at lower strain rates due to the increased time available for Fe-Zn reactions to occur [69].

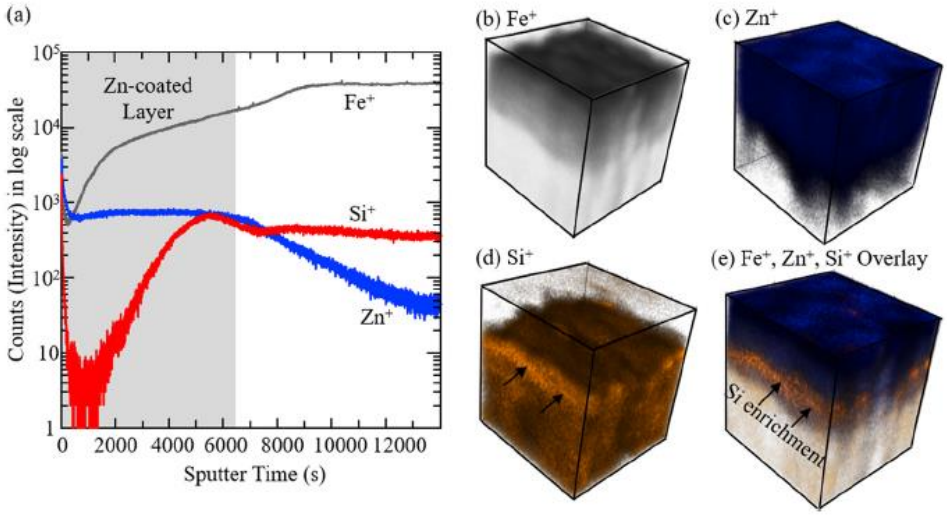

Figure 2.12: TOF-SIMS maps of the steel containing 0.98 wt.% Si [69].

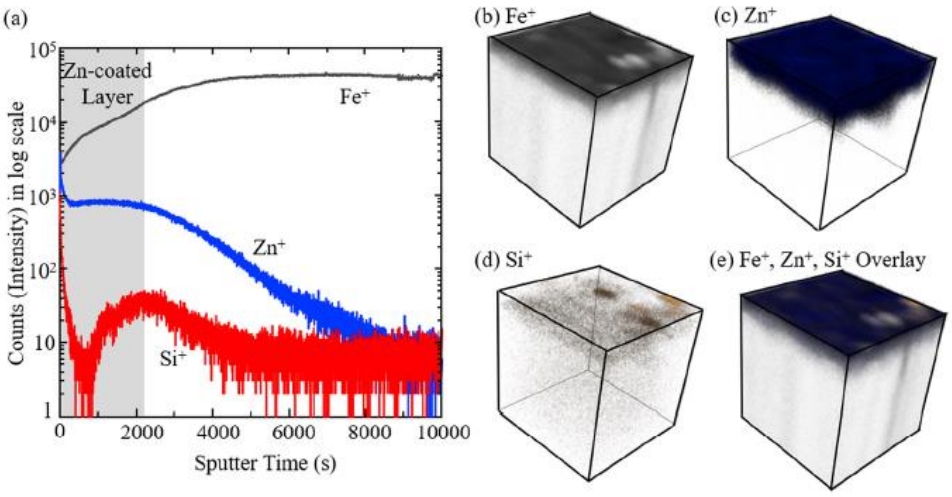

Figure 2.13: TOF-SIMS maps of the steel containing 0.06 wt.% Si [69].

2.5.2 Grain Boundary Wetting

Grain boundary wetting of a solid metal by a liquid metal is defined as the substitution of the initial grain boundary with a liquid film, which leads to the formation of two solid/liquid interfaces. This process does not need external stress to occur [61]. Instead, it can be said that the driving force arises from the reduction in the total energy of the interfaces. The driving force, therefore, is described in Equation (2.2), where γ_{GB} is the grain boundary energy and γ_{SL} is the surface energy of the solid/liquid interface [61]. If Equation (2.2), is positive, grain boundary wetting is favorable. If not, there is not a good incentive to form the two solid/liquid interfaces. This is shown by Figure 2.14.

$$\gamma_{GB} - 2\gamma_{SL} \tag{2.2}$$

Spontaneous wetting at grain boundaries happens at or above a transitional wetting temperature (T_W) where Equation (2.2) is greater than zero. This temperature is higher than the melting

temperature of the wetting alloy [61], [70]. It can be said that grain boundary penetration will happen above T_W, where the grain boundaries of the base metal can be wetted by the liquid metal.

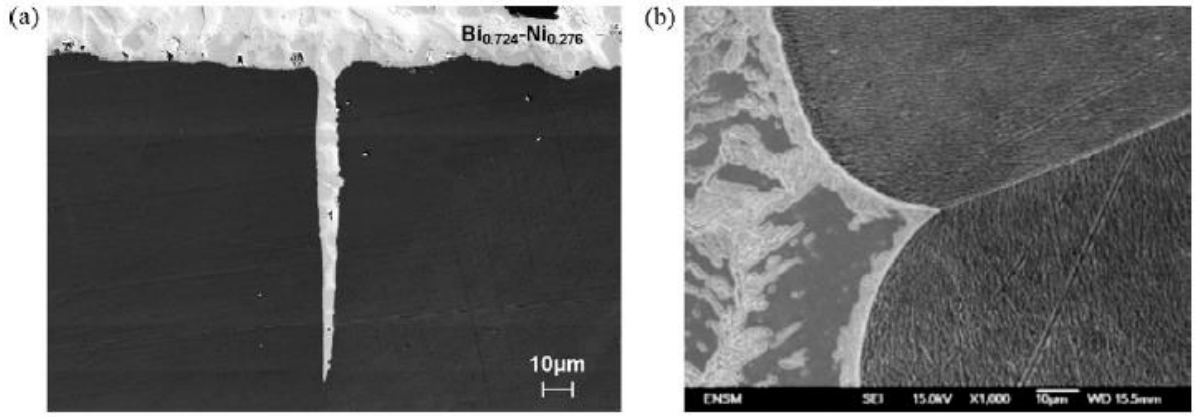

Figure 2.14: (a) Ni polycrystalline specimen after 1 h of direct contact with Bi–Ni liquid alloy at 700 °C which is above the wetting temperature of this system and grain boundary wetting occurs, (b) Cu polycrystalline specimen after 46 h of direct contact with Bi–Cu liquid alloy at 500 °C which is below the wetting temperature of this system and grain boundary grooving occurs [61].

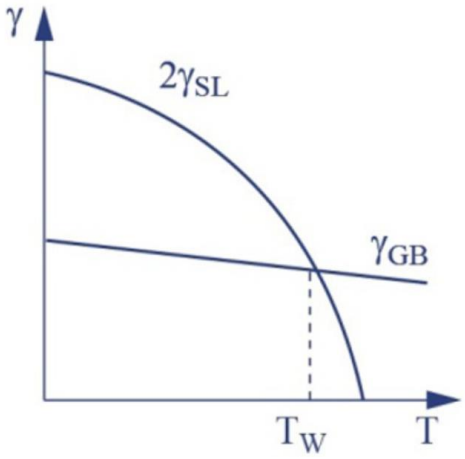

Figure 2.15: Qualitative evolution of grain boundary energy and solid-liquid interface energy as a function of temperature [70].

Moreover, the role of grain boundary angle should be discussed as it can affect T_W which in turn enables LME at lower temperatures. High angle grain boundaries have a higher grain boundary energy in comparison to low angle grain boundaries. Consequently, they are significantly more susceptible to LME [71], [72].

2.5.3 Applied Tensile Stress

The last requirement for LME is applied tensile stress. In the Fe-Zn system present in DHPF, these stresses are either draw stresses or bending stresses that are applied by the die in the forming process [8]. There appears to be a direct correlation between strain rate and susceptibility to LME. Specifically, increasing the strain rate has been found to result in a corresponding increase in LME susceptibility [69], [73].

2.5.4 LME Mitigation

In order to effectively leverage the improved corrosion-resistant properties of Zn coatings in PHS, it is imperative to mitigate LME. LME will not occur if its requirements are not met. A few methods can be strategically used to either lower LME susceptibility or prevent it all together. One approach would be to reduce the grain boundary wettability. The addition of interstitial alloying elements is a proposed method in literature [74]. Boron addition was suggested as a potential LME prevention strategy. In this case, B will act as a cohesion enhancing alloying element, thus reducing the grain boundary energy and, therefore, LME susceptibility [74].

An alternative approach to address this issue would involve the elimination of liquid metal in the system. One obvious solution would be to use indirect hot press forming to eliminate the liquid metal from the system. However, this method has disadvantages such as higher costs and formability limitations which have already been discussed (§2.3.2). Another method would be to

create a fully solid coating consisting of α-Fe(Zn) in the DHPF process by either increasing the austenitization time or using thinner initial coatings [34], [75]–[77]. It was shown that only having a α-Fe(Zn) phase in the coating will effectively prevent LME [75]. Nonetheless, it is crucial to consider the corrosion properties of the coating. While it may offer some corrosion protection, it will not provide robust cathodic corrosion protection, as its electrochemical potential will be similar to that of the substrate steel [13], [16]. This topic will be elaborated on in §2.7.

Another way to eliminate the liquid metal would be to employ a pre-cooling step prior to press hardening by using extended transfer times between the austenitization furnace to the forming dies [2], [14], [78], [79]. The pre-cooling step allows the coating to undergo the peritectic reaction (Equation (2.1) forming solid Γ-Fe_3Zn_{10} and α-Fe(Zn) phases. This method is shown to provide robust cathodic corrosion protection [13] and ensure desirable formability. However, careful consideration needs to be given to the mechanical properties side. The hardenability of the standard 22MnB5 grade is not sufficient to produce a fully martensitic microstructure after DHPF below the peritectic temperature by using a pre-cooling step [14], [80], [81]. The hardenability of the substrate can be tailored by adjusting the chemical composition. It has been shown that added Mn content can improve the hardenability significantly, Figure 2.16 [14], [17]. Thomsen et al. [17] have developed two prototype grades that have increased hardenability, which will be discussed in §2.8. Overall, this approach appears to be the most promising in yielding all desirable properties in Zn coated DHPF steels.

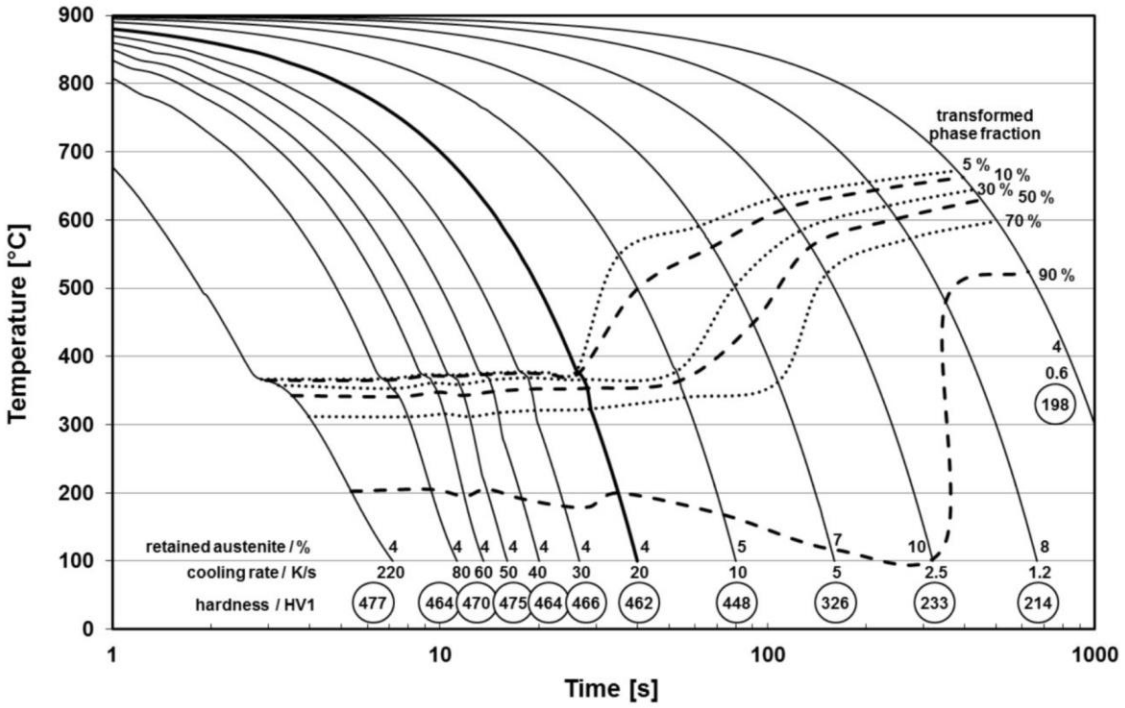

Figure 2.16: CCT curve of 20MnB8, with a composition of 0.195C-0.19Si-1.98Mn-0.003B (wt.%) [14].

2.6 Microcracking

Microcracking, also known as solid metal embrittlement (SME), is defined as an embrittlement induced by a solid-state diffusion-based phenomenon [75], [82]. Microcracking must not be confused with LME as it does not have the three requirements previously stated §2.5. Instead, it requires sufficient time for diffusion at the crack tip and applied stress [75], [82]. Since this process is diffusion controlled, it is not catastrophic; nonetheless, it results in defective parts and necessitates an understanding for effective control [75], [82]–[85]. The notion that the kinetics of crack propagation are controlled by diffusion aligns with experimental evidence. It has been shown that crack growth accelerates with increased temperature. Moreover, it decelerates with increased crack length as the diffusion distance would be increased [93].

Janik et al. [75] have proposed a mechanism for microcracking in Zn-coated PHS, shown by Figure 2.17. They stated that Zn diffuses from the coating into the substrate during austenitization by forming Zn rich pockets that expand (Figure 2.17 (b)). If austenitization is stopped when Zn rich pockets are present, and tensile stress is applied, deep sharp cracks form as a result (Figure 2.17 (c)). However, by allowing austenitization to happen over a longer period of time, the coating will become thicker, and the Zn rich pockets will homogenize (Figure 2.17 (d)). In this case, by applying tensile stress, the cracks are blunted because there is not enough Zn to support microcracking (Figure 2.17 (e)) [75].

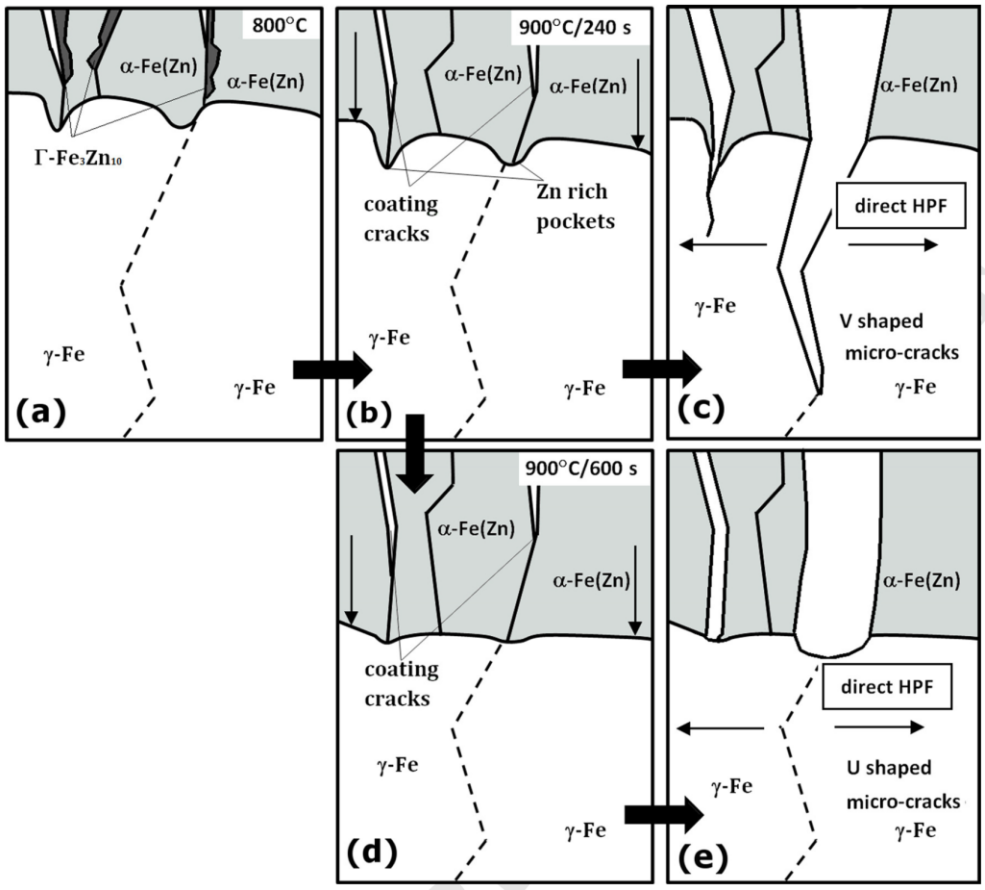

Figure 2.17: Schematic mechanism of microcracking in Zn-coated PHS [75].

Maleki et al. [51], [86] have advanced a slightly different mechanism on the origin of microcracking. Figure 2.18 is a schematic mechanism for solid state diffusion of Zn along coincident α-Fe(Zn)/γ-Fe(Zn) grain boundaries derived from Scanning Transmission Electron Microscopes Electron Energy Loss Spectroscopy (STEM-EELS) results [48]. It shows that after annealing a GI 22MnB5 at 900 °C for 780 s, the coating is transformed into α-Fe(Zn), and Zn had diffused into the austenitic substrate, forming more α-Fe(Zn). More importantly, it is shown that austenite grain boundaries act as an accelerated diffusion path for Zn, which results in the creation of Zn-enriched grain boundaries [48].

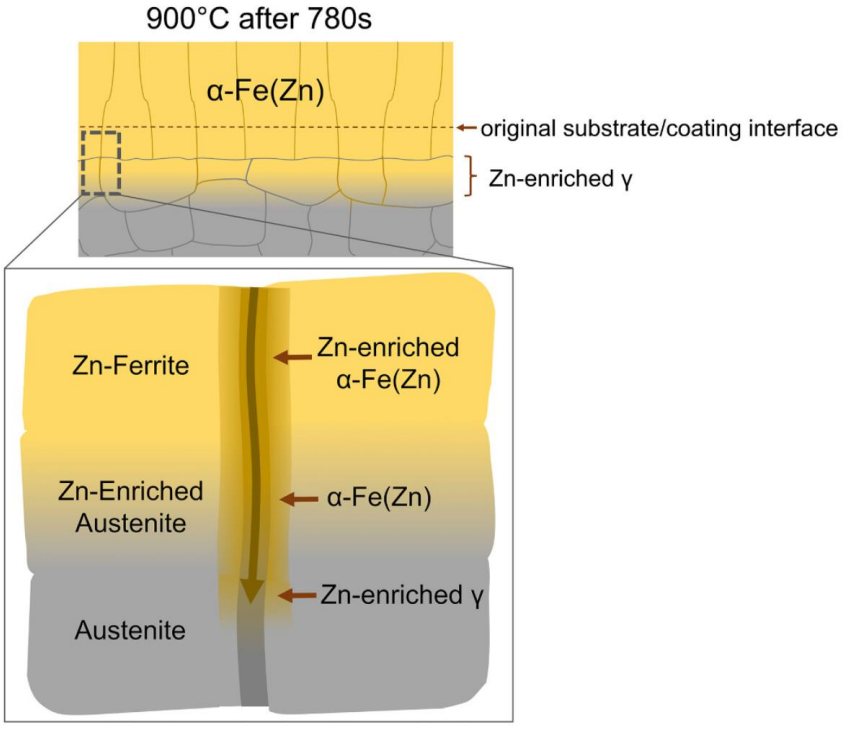

Figure 2.18: Schematic mechanism for solid state diffusion of Zn along coincident α-Fe(Zn)/γ-Fe(Zn) grain boundaries [51].

Based on these results, Maleki et al. [51], [86] proposed a mechanism for crack initiation, growth and blunting in microcracking, the schematic of which is shown in Figure 2.19. It has been stated

that due to the mechanism in Figure 2.18, a thin α-Fe(Zn) layer is present at the austenite grain boundaries. These Zn-enriched grain boundaries were proven to be more susceptible to crack initiation by electron backscatter diffraction (EBSD) maps along the microcracks. The increased susceptibility was attributed to a reduction in grain boundary cohesion. It was suggested that microcracks initiate at Zn-enriched α-Fe(Zn) grain boundaries in the coating, and propagate into the Zn-enriched substrate prior austenite grain boundaries, where the α-Fe(Zn) film is situated. The microcracks eventually blunt as the Zn enrichment along the prior austenite grain boundary is exhausted [51], [86].

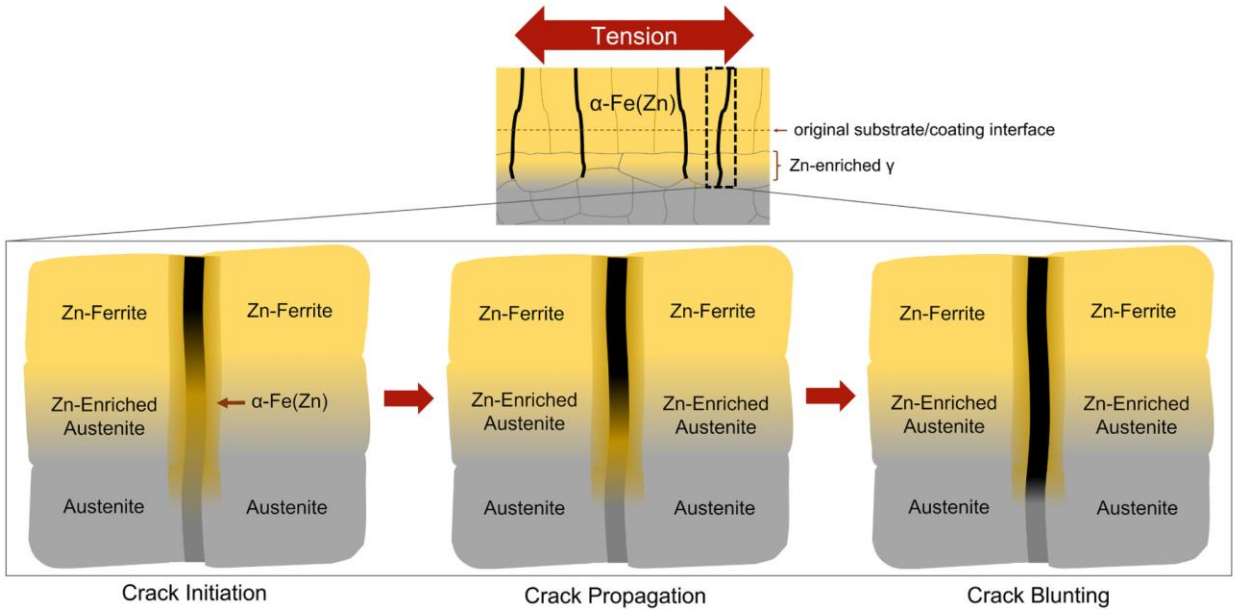

Figure 2.19: Schematic of the proposed mechanism by Maleki et al. for microcracking upon the application of tensile stress [51].

2.7 Corrosion Properties of Zinc Coated Press Hardened Steel

As discussed earlier (§2.4.2), the austenitization step in DHPF alters the microstructure of zinc coatings, ultimately creating Γ-Fe_3Zn_{10} and α-Fe(Zn). Given that each of these phases exhibits

different corrosion properties, it is crucial to identify which one is favorable for optimum corrosion protection.

Electrochemical methods such as open circuit potential, potentiostatic polarization, potentiodynamic polarization or galvanostatic polarization tests were utilized to evaluate the coating [12], [13], [50]. Dever et al. [12] studied the effect of austenization time on the electrochemical properties of a DHPF GI70 coating as a function of austenitization time. Potentiodynamic polarizations tests revealed that increasing austenitization time corresponds to an increase in mixed potential, as it results in a higher fraction of α-Fe(Zn), and Γ-Fe_3Zn_{10} is known to have a lower elechtrochemical potential in comparison to α-Fe(Zn) [13], [16]. Since the driving force for cathodic protection is approximately defined as the difference in E_{corr} between the substrate and the coating, lower elechtrochemical potential translates to possession of improved cathodic corrosion protection properties.

Figure 2.20 shows an Evan's diagram for a ferritic substrate, a mixed phase α-Fe(Zn) + Γ-Fe_3Zn_{10} coating and a single α-Fe(Zn) phase coating. These coatings were obtained using 60 s and 360 s annealing times at 900 °C, respectively [12]. This diagram highlights two primary observations. Firstly, it shows the necessity for having Γ-Fe_3Zn_{10} to have robust cathodic corrosion protection since the mixed coating has a lower electrochemical potential. Secondly, it shows that having a mixed phase coating provides cathodic corrosion protection for longer times. This is due to the fact that the anodic current density of the mixed phase coating is comparatively lower than that of the coating consisting solely of α-Fe(Zn), thereby indicating a slower dissolution rate and a prolonged duration of cathodic protection [12]. This observation implies that the coating needs to undergo the peritectic reaction (Equation ($\alpha\text{-Fe(Zn)} + \text{Zn(Fe)}_{liq} \rightarrow \alpha\text{-Fe(Zn)} + \Gamma - \text{Fe}_3(\text{Zn})_{10}$

(2.1)), which makes the Γ-Fe_3Zn_{10} from the Fe- Zn liquid, to have robust cathodic corrosion protection.

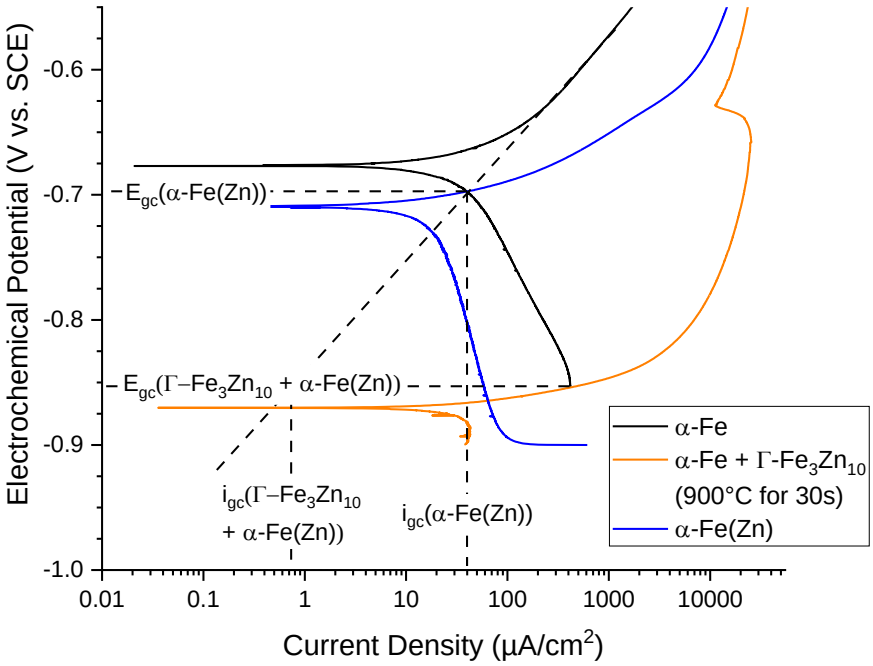

Figure 2.20: Potentiodynamic curves and galvanic couple corrosion currents (i_{gc}) for the 22MnB5 substrate (α-Fe), a mixed Γ-Fe_3Zn_{10} + α-Fe(Zn) coating and a 100% α-Fe(Zn) coating [13].

Dever et al. [12], conducted galvanostatic polarization tests to determine the minimum necessary Γ-Fe_3Zn_{10} that would yield in robust cathodic corrosion protection, Figure 2.21. It can be seen that having a 15 vol% of Γ-Fe_3Zn_{10} is sufficient to produce a low electrochemical potential [12]. This range corresponds to the Γ-Fe_3Zn_{10} phase as α-Fe(Zn) contains about 17-44 wt.% of Zn [2].

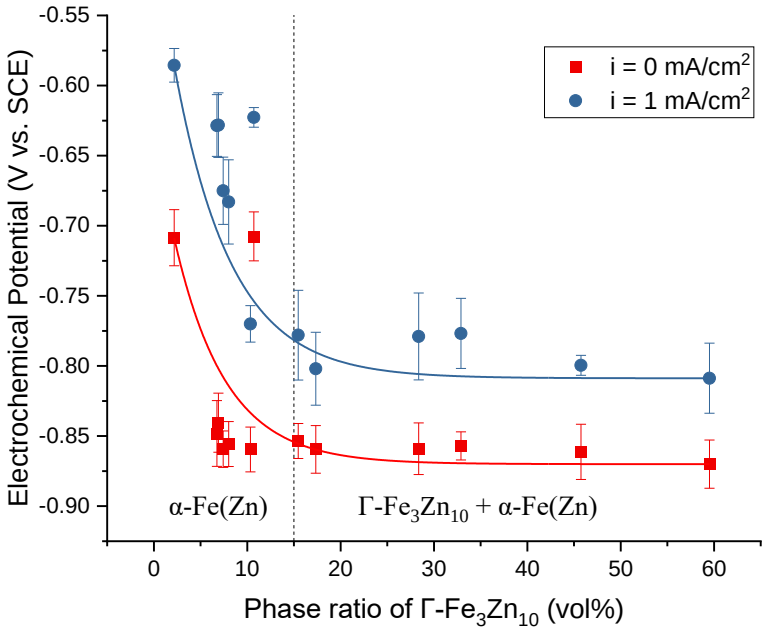

Figure 2.21: Galvanostatic characteristics of the Zn-coated PHS as a function of Γ-Fe_3Zn_{10} fraction [13].

2.8 New Prototype PHS Grades

Thomsen et al. [15] have done extensive research to develop new prototype PHS grades with the compositions of 0.20C-2.01Mn-0.26Si-0.005B and 0.19C-2.5Mn-0.26Si-0.005B (wt.%) that can effectively mitigate LME through stamping at lower temperatures. As discussed earlier, stamping conventional 22MnB5 at lower temperatures will not yield in a martensitic microstructure [14], [78]. Thus, the prototype steels had increased Mn content, specifically 2%Mn and 2.5%Mn, as means to increase hardenability [15]. Their CCT diagrams were determined using quench dilatometry to identify the critical cooling temperature that would result in a fully martensitic microstructure, shown in Figure 2.22. It was determined that the critical continuous cooling rate, resulting in a fully martensitic microstructure, for the 2%Mn and 2.5%Mn were

approximately -10°C/s and –5°C/s, respectively. These values are significantly lower than the critical cooling rate of -25°C/s for 22MnB5.

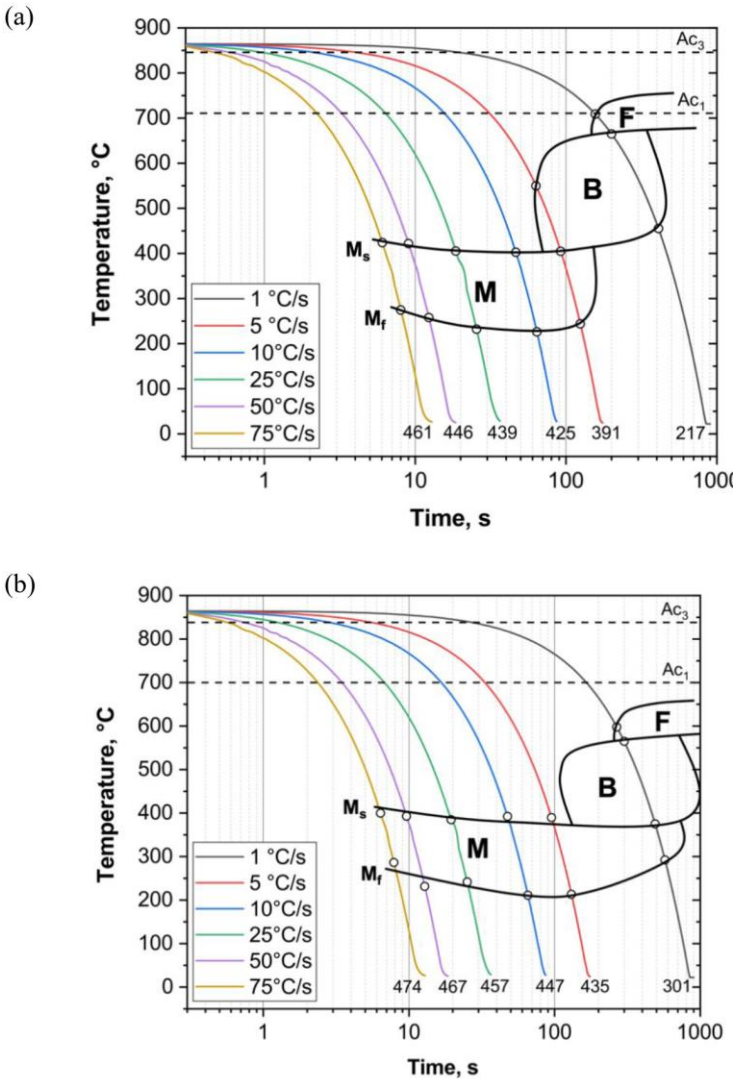

Figure 2.22: CCT diagrams of prototype steels: (a) 2%Mn and (b) 2.5%Mn [15].

Furthermore, the impact of deformation on the M_s and M_f temperatures was determined. It was found that deformation reduced the hardenability and decreased the critical temperatures [15]. This is in agreement with other studies indicating the necessity of utilization of high quenching rates to ensure a fully martensitic microstructure [43].

To assess the mechanical properties of the prototype steels, galvanized samples were austenitized at 890 °C and quenched at stamping temperatures of 700 °C, 650 °C, and 600 °C using a U-shaped die (Figure 2.23). It was found that austenitization times of 120 s for the 2%Mn steel and 60 s for the 2.5%Mn steel were sufficient in producing the desired substrate microstructure [17]. Moreover, it was found that all the stamping temperatures resulted in adequate mechanical properties.

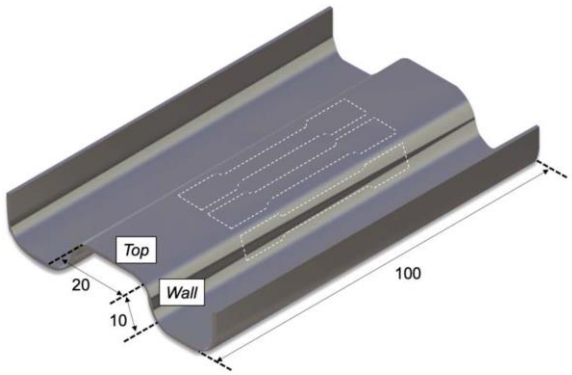

Figure 2.23: Schematic of DHPF part highlighting tensile coupons locations [17].

Figure 2.24 shows UTS and YS as a function of various austenitization times for the two prototypes. It should be noted that these values are averaged across all stamping temperatures as they were found to produce similar results [17]. Aiming to achieve an ultimate tensile strength of 1500 MPa and a yield strength of 1100 MPa [2], the austenization time had to be maintained for at least 60 seconds for the 2%Mn steel and 30 seconds for the 2.5%Mn steel, respectively [17]. Interestingly, it was revealed that the mechanical properties of the top and the wall the U-shape part were comparable [17]. A similar finding has also been reported for the case of 22MnB5 steel by Lee et al. [87]. Based on the analysis, it is understood that the U-shaped DHPF part possesses uniform mechanical properties across its various regions.

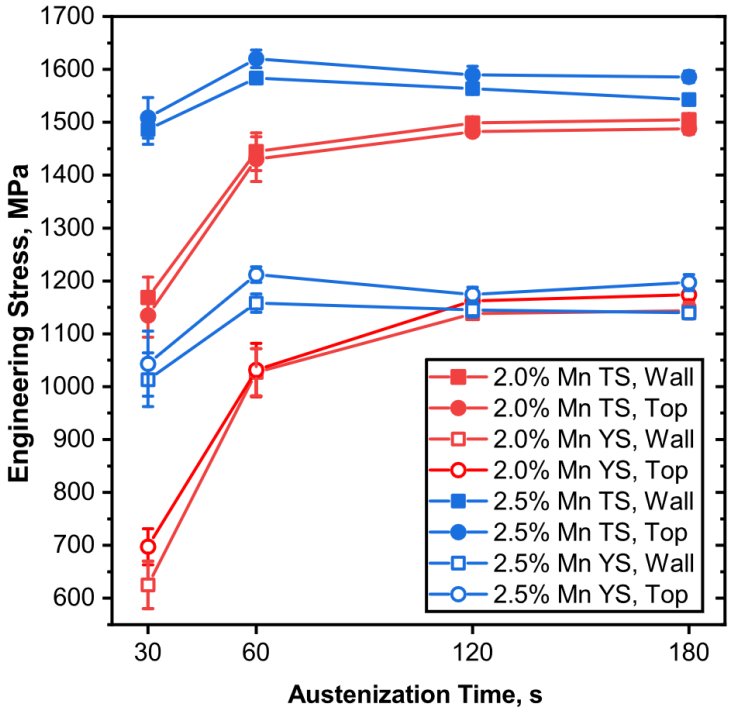

Figure 2.24: Mechanical properties for the 2%Mn and 2.5%Mn prototype PHS averaged over stamping all temperatures [17].

Uniform elongation (UE) and post uniform elongation (PUE) are summarized in Figure 2.25. It can be seen that UE decreased with an increase in UTS, as expected. Conditions resulting in higher ferrite content in the substrate exhibited higher UE. For a fully martensitic substrate, the elongations of both the 2%Mn and 2.5%Mn grade match the values for PHS reported in literature [5], [17], [88]. Moreover, a ductile fracture was observed in the tensile coupons. From these results, it can be concluded that LME was successfully avoided for all the conditions of this study [17].

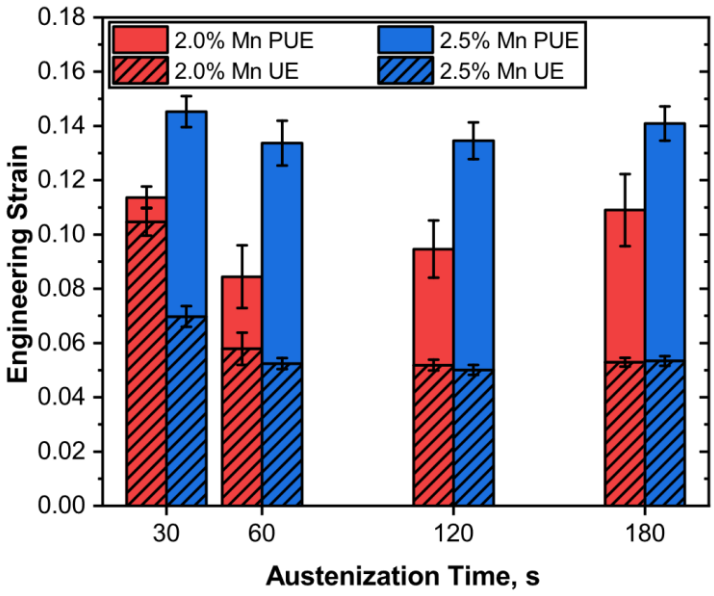

Figure 2.25: Uniform elongation (UE) and post uniform elongation (PUE) for the 2%Mn and 2.5%Mn prototype PHS averaged over stamping all temperatures [17].

Jewer [16] investigated the effects of DHPF parameters on the ability of a Zn-based coatings to provide robust cathodic protection for the prototype steels designed by Thomsen et al. [15]. Figure 2.26 summarizes the potentiodynamic polarization results across all conditions, which were austenitization times of 30-180 s at 890 °C and stamping temperature of 700 °C [16]. It can be seen that the various austenitization times did not have a significant impact on E_{corr}. It is noteworthy that different sections of the U-shaped part exhibited similar corrosion potential[16]. Moreover, the driving force for cathodic protection was slightly lower for the coated DHPF 2.5%Mn steel in comparison to the 2%Mn steel [16]. This was attributed to the higher Mn content which is known to be detrimental to the corrosion properties of steel as it increases the dissolution current density [89]. Although, this effect has not been observed for lower Mn contents such as 1.5 wt.% [90]. Furthermore, it was determined by XRD that 15 vol% of Γ-Fe_3Zn_{10} was present at all the conditions , as was deemed necessary by Dever et al. [12], [16].

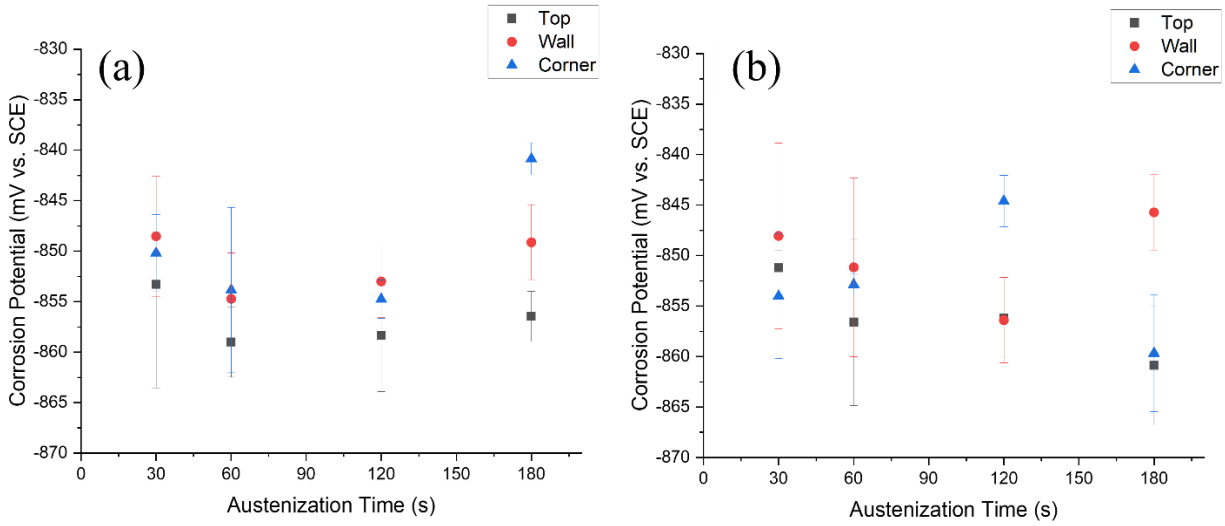

Figure 2.26: Corrosion potential as a function of austenitization time for (a) 2%Mn and (b) 2.5% Mn [16].

The duration of cathodic protection can be determined by dissolution kinetics of coating phases, as shown by galvanostatic scans. As coating thickness increases with annealing time, it is important to consider results from the same annealing time when comparing the two prototypes. Figure 2.27 shows the galvanostatic scans for the two prototypes after austenitization at 890 °C for 120 s and stamping at 700 °C [16]. The length of the first plateau, which is associated with the dissolution of Γ-Fe_3Zn_{10} , determines the length of robust cathodic corrosion protection. It can be seen that both of the prototypes can provide long-term cathodic corrosion protection of the substrate, however, 2%Mn seems to provide protection for longer times. Figure 2.28 shows a summary of the Γ-Fe_3Zn_{10} plateau length for all conditions [16]. It is evident that after 180 s of annealing, robust cathodic corrosion protection cannot be expected. For the annealing times lower than that, robust cathodic corrosion protection was achieved. Moreover, there was a slight difference between the different regions of the part which can be associated with die wiping

exposing the α-Fe(Zn) phase. Nevertheless, robust cathodic corrosion protection was achieved for all the regions [16].

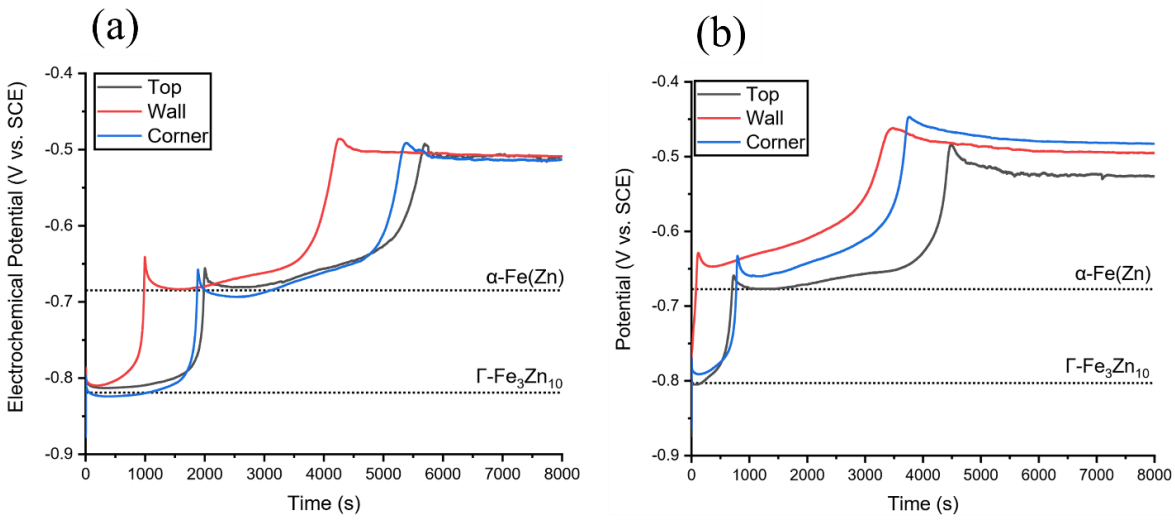

Figure 2.27: Galvanostatic scans (+ 10 mA/cm^2) for the (a) 2%Mn and (b) 2.5%Mn austenitized at 890 °C for 120 s and stamped at 700 °C [16].

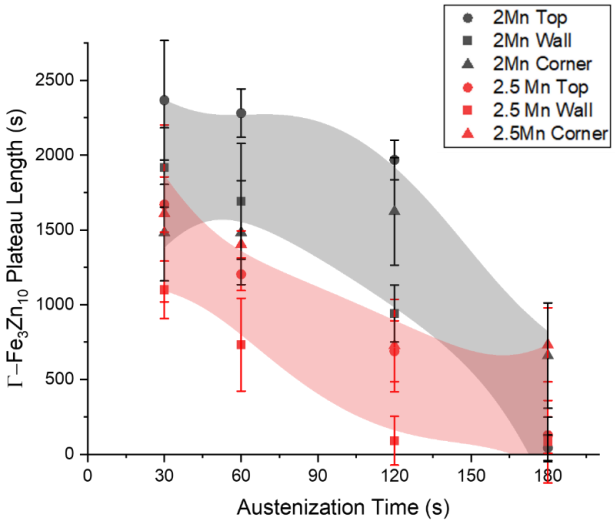

Figure 2.28: Γ-Fe_3Zn_{10} plateau length as function of austenization time for the Zn-coated 2%Mn (black) and 2.5%Mn (red) substrate after DHPF at 700°C with respective 95% confidence intervals [16].

3 Research Objectives

In previous work, utilizing extended transfer times as a method to mitigate Liquid Metal Embrittlement (LME) for two prototype galvanized press hardening steels (PHSs) with increased Mn content (0.20C-2.0Mn-0.26Si-0.005B and 0.19C-2.5Mn-0.26Si-0.005B (wt.%)) has been investigated [15], [17]. Having an extended transfer time results in press hardening happening at a temperature lower than the Fe-Zn peritectic temperature of 782 °C; thus, avoiding LME by eliminating the liquid metal in the coating. It was shown that by using this technique, not only was LME prevented, but also a desirable microstructure for both the coating and substrate were formed. As a result, the target mechanical property of UTS ≥ 1500 MPa was met and the coating exhibited robust cathodic corrosion properties [15]–[17]. The primary objective of this work was to determine the feasibility of using an extended transfer time to mitigate LME for a galvannealed (GA) prototype PHS steel. The galvanneal coating, in addition to a different chemical composition such as lower B content, have not been previously studied. Thus, it is interesting to determine if the process is feasible on the new prototype steel. Moreover, from the industrial perspective, it was aimed to determine a process window for the coated steel and determine the potential for scaling through pilot-scale trials for it.

In order to test these objectives, initially, a bare prototype steel and a GA80 coated (i.e., 80 g/m^2/side coating weight) prototype PHS steel with the compositions of 0.20C-1.96Mn-0.25Si-0.003B-0.01Ti, and 0.19C-1.92Mn-0.20Si-0.003B-0.03Ti (wt.%), respectively, were compared. To this end, they were austenitized at 890 °C for 120 s and press formed at 650 °C. Their mechanical properties were compared by tensile testing. Subsequently, panels of the GA-coated steel were austenitized at 890 °C for 120 s and subjected to direct hot press forming (DHPF) at four different temperatures of 550 °C, 600 °C, 650 °C, and 700 °C. The DHPF temperatures were

obtained by increasing the transfer time from the furnace to the die. The target properties for the GA-coated PHS were UTS ≥ 1400 MPa and YS ≥ 1000 MPa. The mechanical properties and microstructural evolution were determined as a function of DHPF temperature by tensile testing, scanning electron microscopy (SEM), microhardness, and X-ray diffraction (XRD). Furthermore, to assess the cathodic corrosion protection with the objective of attaining ≥ 15 vol% Γ-Fe_3Zn_{10} in the coating, the volume fraction of Γ-Fe_3Zn_{10} was determined by XRD. The coating microstructure and the presence of microcracks were analyzed by SEM.

Pilot-scale trials were conducted on the GA-coated steel and consisted of austenitization at 890 °C for four different times of 60 s, 120 s, 180 s, and 240 s. The panels were subsequently subjected to DHPF at temperatures of 550 °C, 600 °C, 650 °C, and 700 °C. Their mechanical properties were analyzed as a function of austenitization time and DHPF temperature by tensile testing and were compared to the results from the laboratory-scale testing.

4 Experimental Methods

4.1 Steel

Two steels were used in this study, the compositions of which can be seen in Table 4.1: Composition of alloys used (wt.%). The values were determined using chemical analysis according to ASTM E1019-18 [91], ASTM E1097-12 [92] and ASTM E1479-16 [93]. Their composition is similar to 22MnB5 with added Mn to allow for stamping at temperatures below the peritectic temperature of 782 °C as a means to avoid LME by eliminating liquid zinc in direct hot press forming process.

The as-received steel K sheets had a thickness of 1.2 mm. Steel K had a 80 g/m^2/side galvannealed coating. The sheets were provided as in-kind donation from voestalpine stahl LLC. The as-received steel I sheets had a thickness of 1.2 mm. These sheets are not coated. Steel I was produced at U.S. Steel R&D Munhall, Pennsylvania. The detailed thermomechanical processing cycle of steel I can be seen in Figure 4.1.

Table 4.1: Composition of alloys used (wt.%).

	C	Mn	Si	Ti	B	S	Fe
Steel I	0.20	1.96	0.25	0.01	0.003	0.005	Bal.
Steel K	0.19	1.92	0.2	0.03	0.003	0.005	Bal.

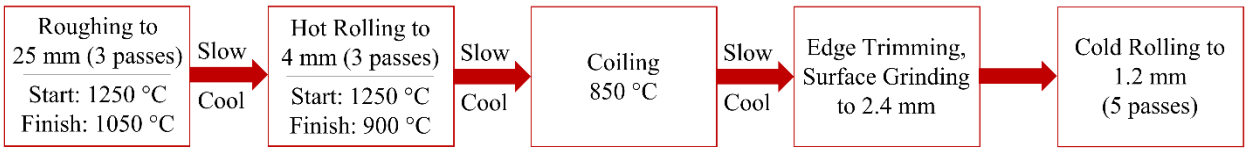

Figure 4.1: The thermomechanical processing cycle for the production of steel I.

The as-received steel I microstructure can be observed in Figure 4.2(a). The microstructure is comprised of elongated grains of ferrite and pearlite with visible banding that is likely the result of Mn segregation during casting. As mentioned in Figure 4.1, the last step in the thermomechanical processing of steel I is cold rolling. The elongated grains which are characteristic of a cold-rolled microstructure are the result of that particular processing step. In the case of the as-received steel K, Figure 4.2(b) revealing an equiaxed microstructure consisting of ferrite and pearlite which is fully recrystallized as a result of the continuous galvannealing process.

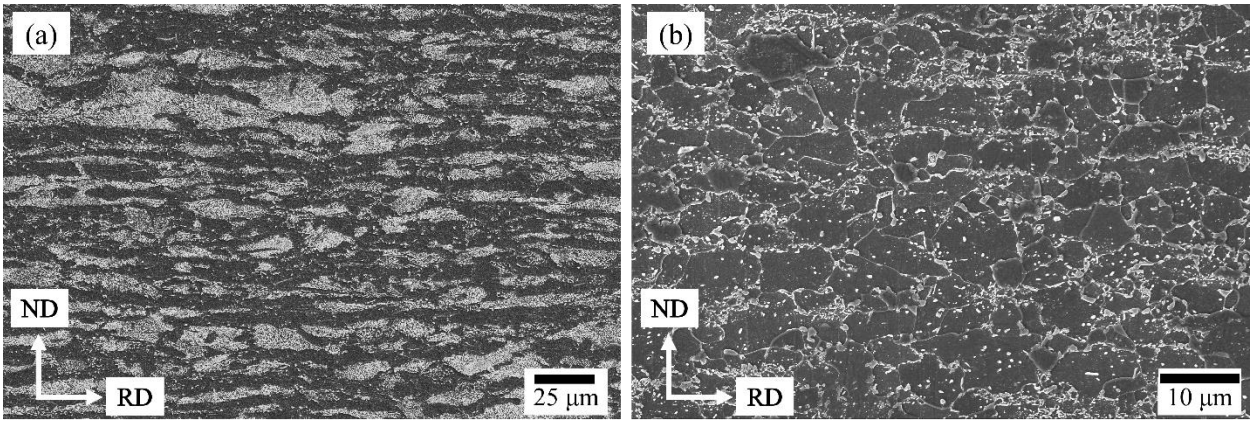

Figure 4.2: SEM micrographs of as received material (a) steel I and (b) steel K.

4.2 Cold Rolling and Dilatometry – Steel I

Cold rolling was performed on a steel I transfer bar prior to dilatometry analysis. The purpose of the cold rolling was to create a relatively high dislocation density in the dilatometry samples that would closely resemble that of the sheets, thus ensuring more representative transformation temperature results from quench dilatometry experiments.

The dimensions of the steel I transfer bar were 25 mm in thickness and 63 mm in width. Subsequently, 25.4 mm-wide sections were cut and subjected to cross cold rolling using a

STANAT TA-215 rolling mill, with a 0.16 mm reduction in thickness per pass. A total of 15 passes were performed on each sample to achieve the desired 20% thickness reduction.

Quench dilatometry tests were carried out to determine the phase transformation temperatures and the continuous cooling transformation (CCT) diagram of steel I. Samples in the shape of cylinders with diameter of 5 mm and the height of 10 mm were cut from the cold rolled transfer bar. Quench dilatometry was done using a BÄHR DIL 805 dilatometer.

To determine the phase transformation temperatures, specifically Ac_1, Ac_3, M_s, and M_f, samples were heated to 1000 °C with heating rates of 5, 10 and 15 °C/s to understand the effect of heating rate on these temperatures. They were subsequently quenched to room temperature with the cooling rate of 160 °C/s. The Ac_1 and Ac_3 were found to be 721 °C and 864 °C, respectively, and to be independent of the heating rates used. Moreover, M_s and M_f were determined to be 396 °C and 294 °C, respectively.

Subsequently, samples were heated to 884 °C (Ac_3 + 20) at a heating rate of 10 °C/s, and held at that temperature for 120 s. The samples were then quenched to room temperature using cooling rates ranging from 0.5°C/s to 75°C/s to determine the critical cooling rate required for the formation of a fully martensitic microstructure. The resulting cooling curves were utilized to construct the Continuous Cooling Transformation (CCT) diagram. To determine the transformations such as B_s and B_f, the microhardness and microstructure of the dilatometry samples were analyzed. Microhardness was measured using a Clemex CMT.HD with a 100 gf load and a dwell time of 10 seconds. To differentiate between the various phases, such as bainite and martensite, color etching using LaPera etchant was performed for 10 to 20 seconds. The LaPera etchant consisted of 30 ± 2 ml of solution #1 and 30 ± 2 ml of solution #2. Solution #1 contained

1 g $Na_2S_2O_5$ (sodium metabisulfite) and 100 ml distilled water. Solution #2 contained 4 g dry picric acid and 100 ml of ethanol.

4.3 Direct Press Hardening

To prepare for direct hot press forming (DHPF), blanks measuring 120 mm x 120 mm were first cut. They were then heated to a temperature of 890 °C for 120 seconds in a conventional box furnace under ambient atmosphere. The austenization temperature was based on previous research indicating that these conditions would yield a desirable coating microstructure consisting of Γ-Fe_3Zn_{10} and α-Fe, as well as suitable mechanical properties. A type K thermocouple was attached using rivets to each blank to monitor the temperature. A representative heating curve can be seen in Figure 4.3. Both Steel I and Steel K exhibit identical heating curves. As shown, the austenization annealing time was measured from the moment the temperature of the samples reached 870 °C, after approximately 67 s. The sample was kept in the furnace for 120 s after this time.

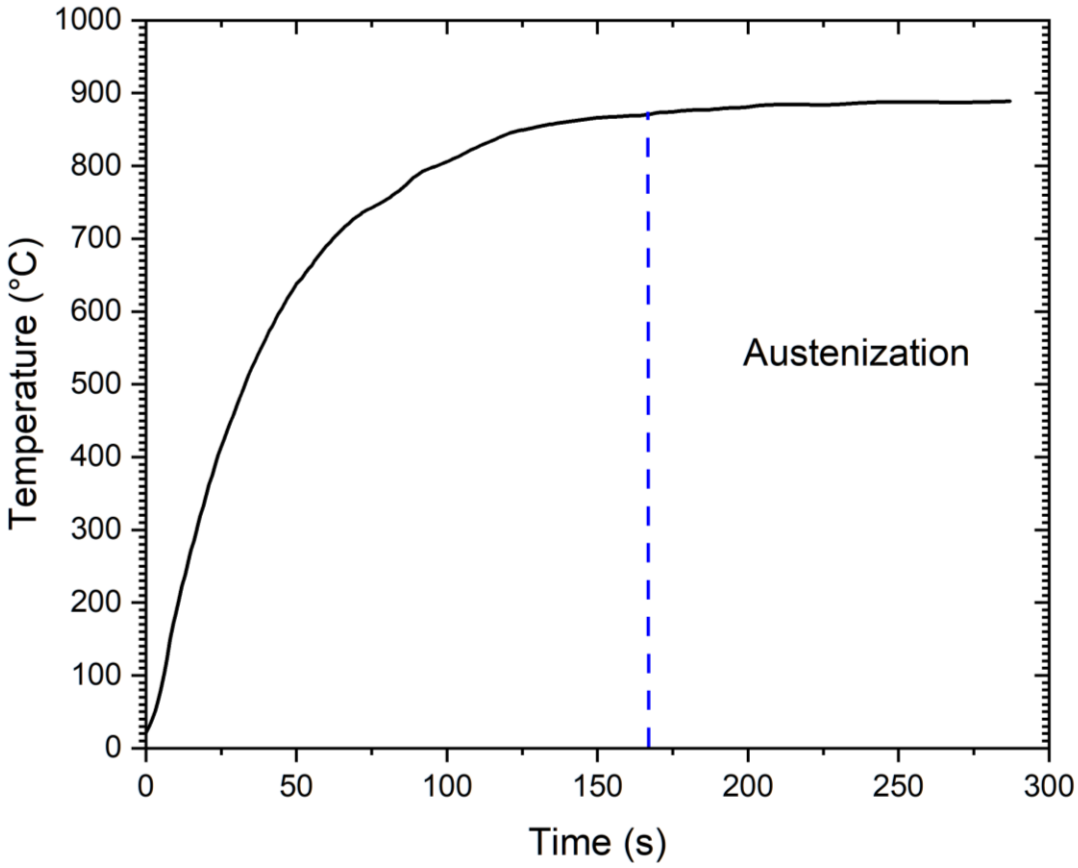

Figure 4.3: Heating curve of steel K annotating the beginning of the austenization step (dashed line).

Following annealing, the blanks were transferred to a water-cooled flat die for hot press forming using a 250 kN Instron frame. An image of the furnace and the die mounted on the machine can be seen in Figure 4.4. Various transfer times from the furnace under ambient conditions to the die were used to DHPF at temperatures ranging from 550 °C to 700 °C, with the goal of determining the process window of the DHPF temperature that would both eliminate the liquid metal (Zn) in the pressing step and yield target mechanical properties ($UTS \geq 1500\ MPa$). Specifically, the transfer times and temperatures used were 9 seconds for 700 °C, 14 seconds for 650 °C, 16 seconds for 600 °C, and 19 seconds for 550 °C. Figure 4.5 shows the cooling curve of a sample stamped at

550 °C. Two regions are labeled on Figure 4.5. The transfer region corresponds to cooling in an ambient environment until the desired stamping temperature was achieved. The other region corresponds to quenching in the water-cooled die. Average quenching rate in the flat die was calculated to be 64 °C/s for all DHPF conditions.

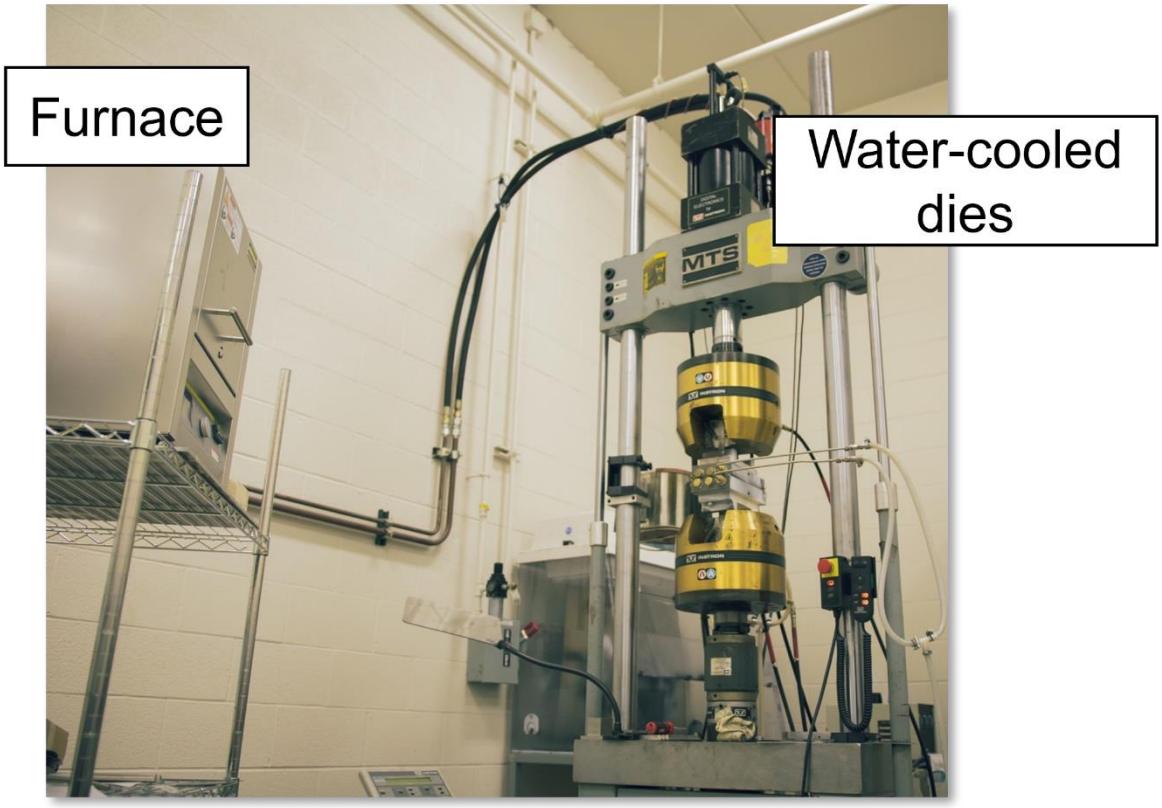

Figure 4.4: Furnace and water-cooled die mounted on a 250 kN Instron frame used for DHPF.

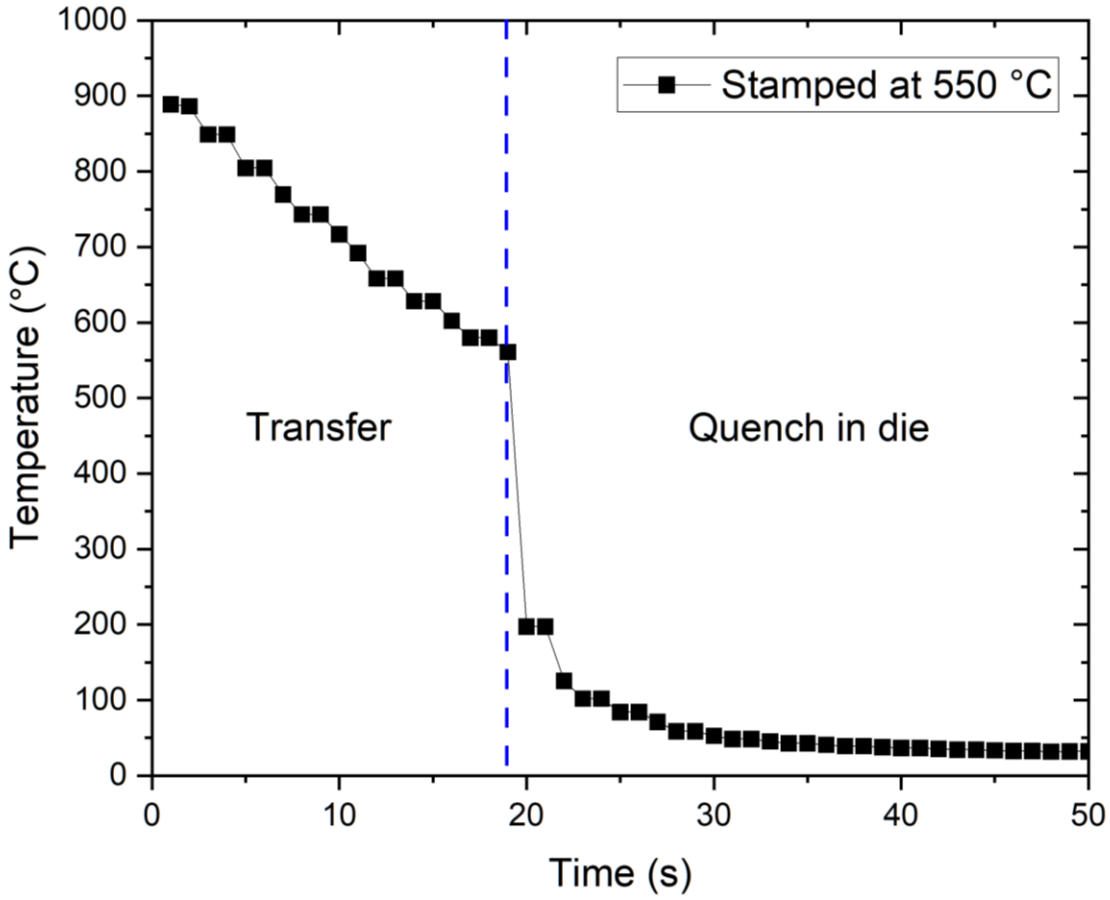

Figure 4.5: Cooling curve of a sample stamped at 550 °C.

4.4 Mechanical Testing

Uniaxial tensile tests and microhardness tests were performed at room temperature to determine the mechanical properties of steel K and steel I as a function of the DHPF temperature. The microhardness of the DHPF substrates was measured using a Clemex CMT.HD with a 100 gf load and a dwell time of 10 seconds. Error bars represent 95% confidence interval of the mean. Tensile tests were performed using a 100 kN Instron frame with a crosshead speed of 1 mm/min. Strain was measured using a contact extensometer with the gauge length of 25.4 mm. Tensile coupons were machined from the uniform temperature portion of the panels as shown in Figure 4.6 into ASTM E8 subsize specimens [94]. All tests were conducted in triplicate to ensure reproducibility

of the results for a total of nine samples for every DHPF temperature. Error bars shown in the results were calculated using the 95% confidence interval of the mean.

Figure 4.6: Tensile coupons in the uniform temperature portion of a DHPF panel.

Equation (4.1) displays the formula for calculating engineering stress, where σ represents engineering stress measured in MPa, F is the tensile force measured in N, and A_0 is the initial cross-sectional area of the tensile gauge in mm² measured using calipers with the resolution of 0.01 mm. Similarly, Equation (4.2) shows the formula for calculating engineering strain, where ε denotes engineering strain, ΔL represents the change in gauge length in mm, and L_0 is the original gauge length prior to testing in mm [4].

$$\sigma = \frac{F}{A_0} \tag{4.1}$$

$$\varepsilon = \frac{\Delta L}{L_0} \tag{4.2}$$

Additionally, Equation (4.3) shows the reduction of area of each fractured tensile coupon which was determined according to ASTM E8 [94], Where A_f represents the area of the fracture surface measured using light optical microscopy. The ultimate tensile strength (UTS) was determined based on the maximum engineering stress for the engineering stress-strain curve. The yield strength (YS) was determined by utilizing the 0.2% offset yield strength method.

$$Z = \frac{A_0 - A_F}{A_0} \tag{4.3}$$

4.5 Scanning Electron Microscopy

The microstructure of both the substrate and the coating as a function of DHPF temperature was evaluated using scanning electron microscopy (SEM). Imaging was conducted using JEOL 6610 LV and JEOL 7000F FEG-SEM microscopes, with an accelerating voltage of 15 keV and a working distance of 10 mm for all the samples. The DHPF blanks were cut into 10 mm × 10 mm samples and mounted cross-sectionally in epoxy resin. All samples were coated with carbon to prevent sample charging.

Secondary electron imaging (SEI) was utilized to image the microstructure of the substrate and determine its correlation to the mechanical properties. Sample preparation involved grinding with silicon paper of varying grits (320, 400, 600, 800, and 1200), followed by polishing with Nap and Dur with 3 and 1 μm diamond suspensions, respectively. To reveal the substrate microstructure, the samples were etched with Nital (2 vol% nitric acid in ethanol), rinsed with water and ethanol, and subsequently blown dry. Finally, they were cleaned in an ultrasonic bath using ethanol for 10 minutes.

The coating microstructure was analyzed using backscattered electron imaging (BEI) to predict the corrosion properties of the steel as a function of DHPF temperature. Previous research has

demonstrated that 15 vol% of Γ-Fe_3Zn_{10} phase can provide robust cathodic protection [13]. Therefore, the presence of the Γ-Fe_3Zn_{10} phase was determined using SEM-BEI. The quality of the coating, specifically the presence of microcracks, was of interest as well. The sample preparation method was similar to the above with a few minor changes. The samples were not etched, as it deteriorates the coating, and in order to prevent over-polishing of the coating, the polishing steps were shortened.

4.6 X-Ray Diffraction

The phase analysis of the substrate and coating was determined using 2D X-ray diffraction (XRD2). The diffraction patterns were collected using a Bruker Mo Smart APEX2 diffractometer, with Co $K\alpha_1$ radiation (λ = 1.79026 Å) as the source. To ensure accuracy, both a microslit and collimator were used, both with a diameter of 1 mm. X-rays were generated with a voltage of 35 keV and a current of 45 mA. A coupled $2\theta/\theta$ scan was used with four steps from $45° \leq 2\theta \leq 100°$, and a scan time of 600 s/step. The Eiger 2R detector was used to collect diffracted X-rays.

Phase identification was conducted using Bruker DiffracEva v.5.2 on the raw data. Bruker TOPAS 5 was utilized to model the measured peaks and determine the phase fractions of the coating and substrate. Triplicate measurements were taken randomly from the samples, and error bars were calculated based on the 95% confidence interval of the mean.

4.7 Pilot-scale DHPF of Steel K

A set of pilot-scale DHPF trials of GA steel K was performed at Gestamp. Blanks were austenitized at 890 °C for four different annealing times of 60 s, 120 s, 180 s, and 240 s. Subsequently, they were direct press hardened at 700 °C, 650 °C, 600 °C and 550 °C. Figure 4.7 shows the U-shaped die configuration used in the trials. The dimensions of the blanks used were 280 x 650 mm. Figure 4.8 shows the resultant part configuration and dimensions. To analyze the mechanical properties,

uniaxial tensile tests were carried out on the parts. Standard-sized ASTM E8 tensile coupons with a gauge length of 50 mm were extracted from the top and side section of the U-shaped die (Figure 2.23) [94]. The tensile tests were conducted in accordance with the ASTM E8, ASTM E646, and ASTM E517 standards [94]–[96].

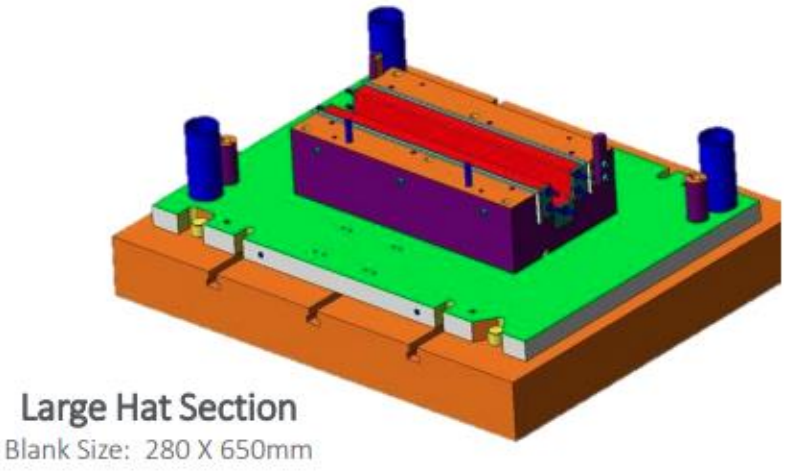

Figure 4.7: Die configuration of the pilot-scale DHPF trial [97].

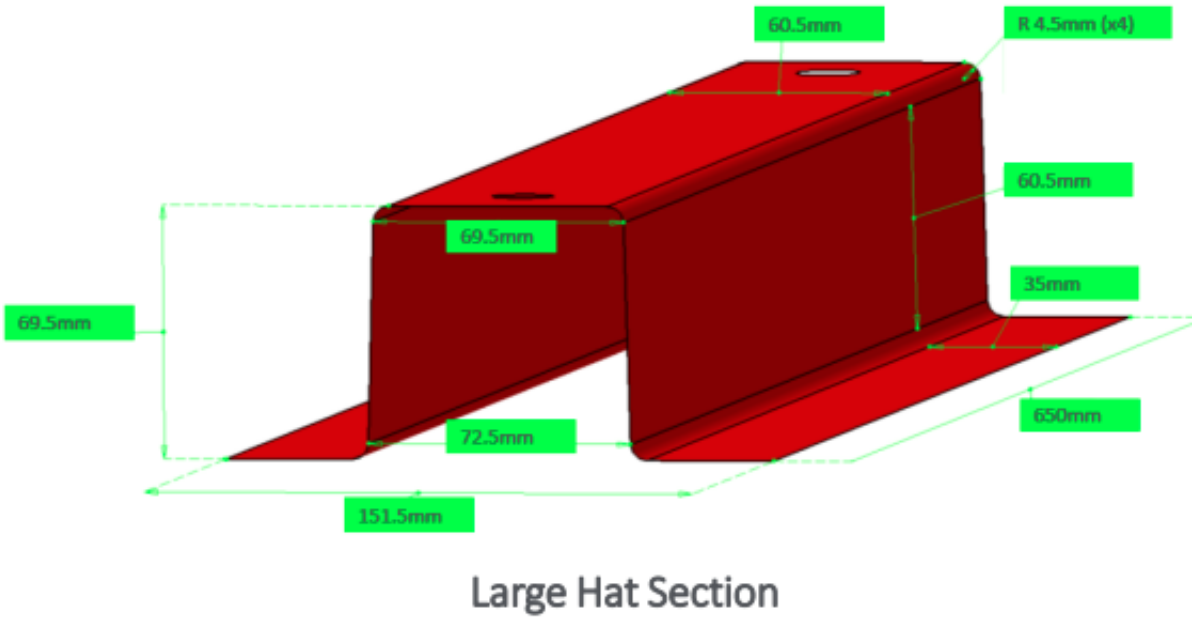

Figure 4.8: Part configuration and dimensions of the pilot-scale DHPF trial [97].

5 Results

5.1 Dilatometry of Steel I

Dilatometry was conducted on steel I with the objective of establishing its continuous cooling transformation (CCT) diagram. The dilatometry curve obtained from a sample subjected to a heating rate of 15 °C/s, as described in §4.2, is presented in Figure 5.1 (a). This curve aimed to investigate the influence of the heating rate on the critical transformation temperatures, namely Ac_1, Ac_3, M_s, and M_f. It should be noted that the thermal expansion coefficients of different constituents, such as ferrite and austenite, vary. The change in the crystal structure from BCC to FCC and the subsequent dilation causes changes in the slope of the linear portion of the curve [98].

The initiation of a phase change is characterized by a deviation from linearity in the curve, whereas the termination of the phase change is indicated by the curve returning to a linear behavior. Figure 5.1 (b) shows the variation in heating rate depicted in Figure 5.1 (a) during the heating process. In order to determine Ac_1 and Ac_3, the points at which the curve deviates from linearity were identified through a combined approach involving both analysis of the derivative curve and the tangent method. The derivative of the dilatometric curve with respect to temperature is represented by the red curve. The blue lines represent the tangent to the graph to aid in identifying the linear portion of the curve. Similarly, for the determination of M_s and M_f, the non-linear section of the cooling portion in the dilatometry curve (Figure 5.1 (c)) was subjected to analysis. It can be seen that by employing these techniques, a comprehensive evaluation of the dilatometry curve facilitated the calculation of the desired critical temperatures.

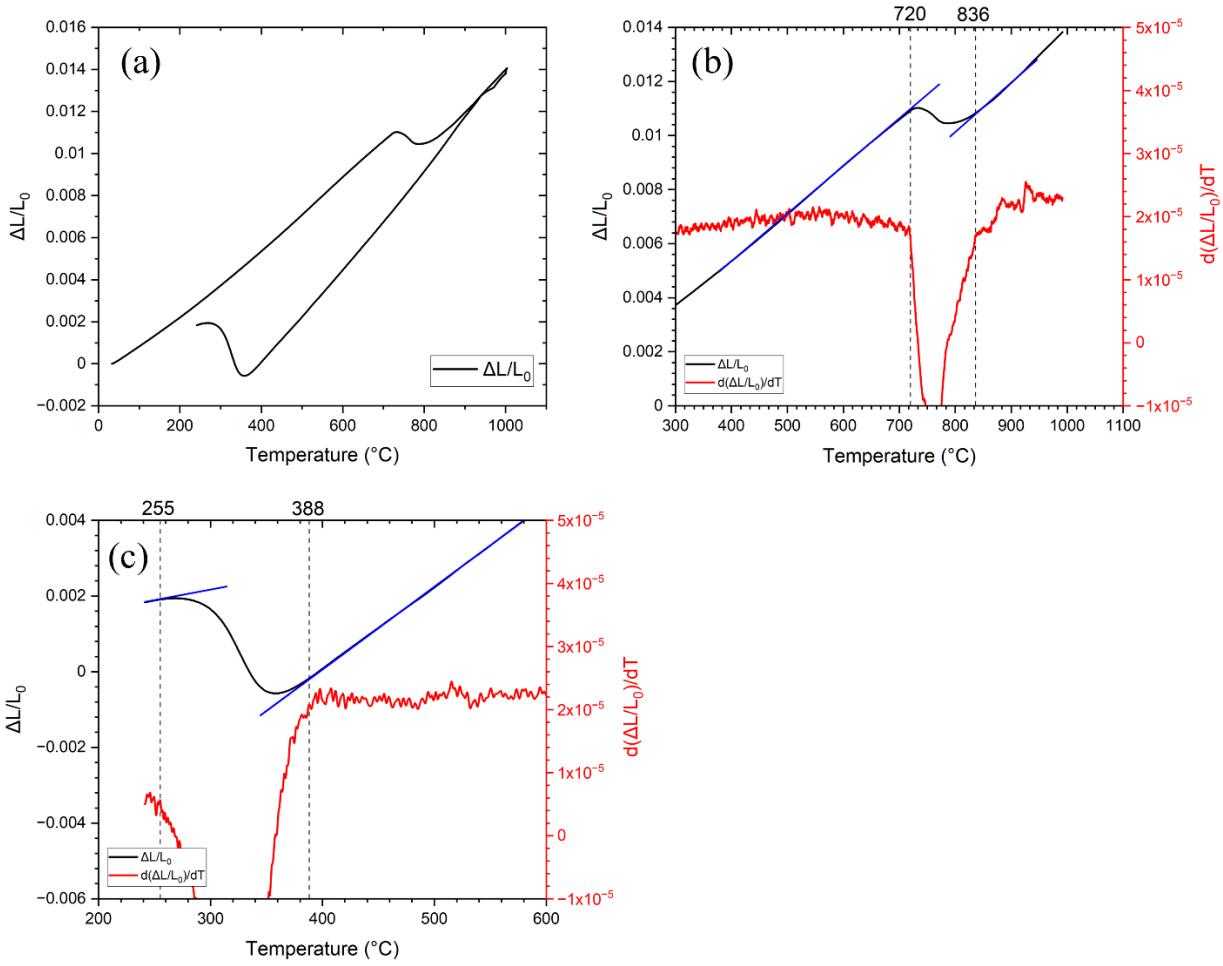

Figure 5.1: (a) Dilatometry curve of a sample heated at 15 °C/s, (b) the heating portion of the dilatometry curve (c) the cooling portion of the dilatometry curve.

Figure 5.2 shows the critical temperatures that were calculated from quench dilatometry for this steel. The average values for Ac_1 and Ac_3 were 721 °C and 864 °C, respectively. It can be seen from Figure 5.2 (a) that the heating rate did not affect Ac_1 and Ac_3. The average M_s and M_f values are 396 °C and 254 °C. These values were independent of the heating rate as well, which is shown by Figure 5.2 (b).

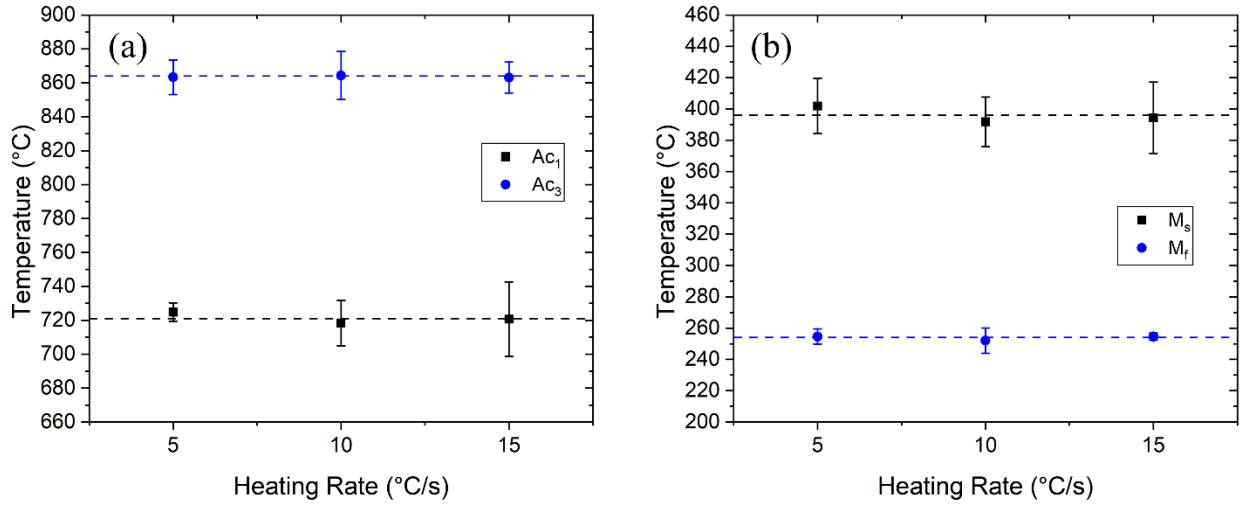

Figure 5.2: Effect of heating rate on critical temperatures of steel I (a) Ac_1 and Ac_3, (b) M_s and M_f.

Figure 5.3 shows the CCT diagram constructed from the cooling curves derived from the dilatometric tests. It can be seen that the microhardness values, which are written on the bottom of each curve, increase as the cooling rate increases, which is an indication of different constituents present. The microhardness values correspond well to the microstructural zones that have been determined using the cooling curve analysis. As a fully martensitic microstructure is of interest, it is observed that cooling rates higher than 10 °C/s produce a fully martensitic microstructure. Moreover, cooling rates of 3 °C/s and 5 °C/s will result in a bainitic microstructure. Cooling rates lower than 1 °C/s result in a ferrite-pearlite microstructure. Thus, a critical cooling rate of 10 °C/s needs to be used during direct press forming to achieve a fully martensitic microstructure.

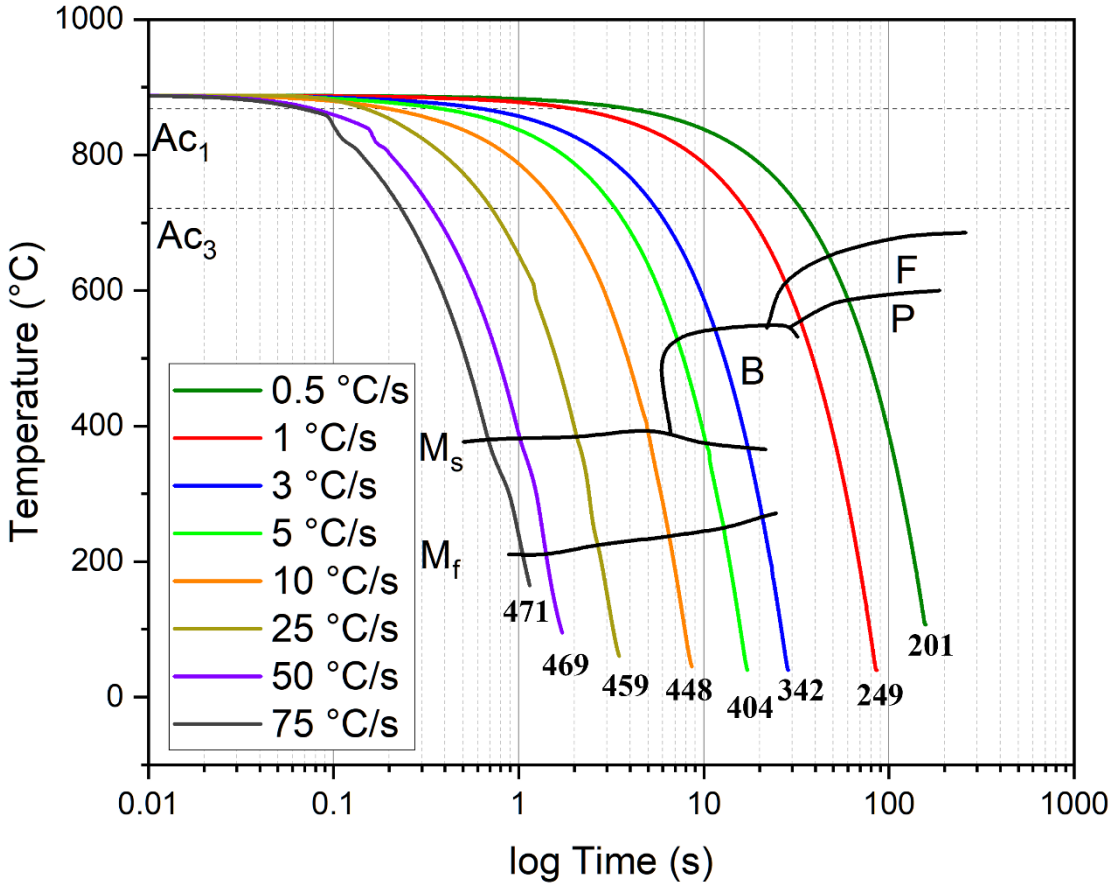

Figure 5.3: Continuous cooling transformation (CCT) diagram of steel I with microhardness values expressed in HV for every experimental cooling rate.

Figure 5.4 shows optical microscopy microstructures of quench dilatometry samples that were etched using LaPera etchant. A fully martensitic microstructure can be observed for cooling rates higher than 10 °C/s. The darker regions highlighted for the cooling rates of 3 °C/s and 5 °C/s are indicative of bainite, and the lighter regions show martensite. Beige and white toned regions have been identified for cooling rates lower than 1 °C/s which are indicative of ferrite and pearlite, respectively. These microstructures are in agreement with the phases identified by analysis of the dilatometric curves during cooling, as shown in Figure 5.3.

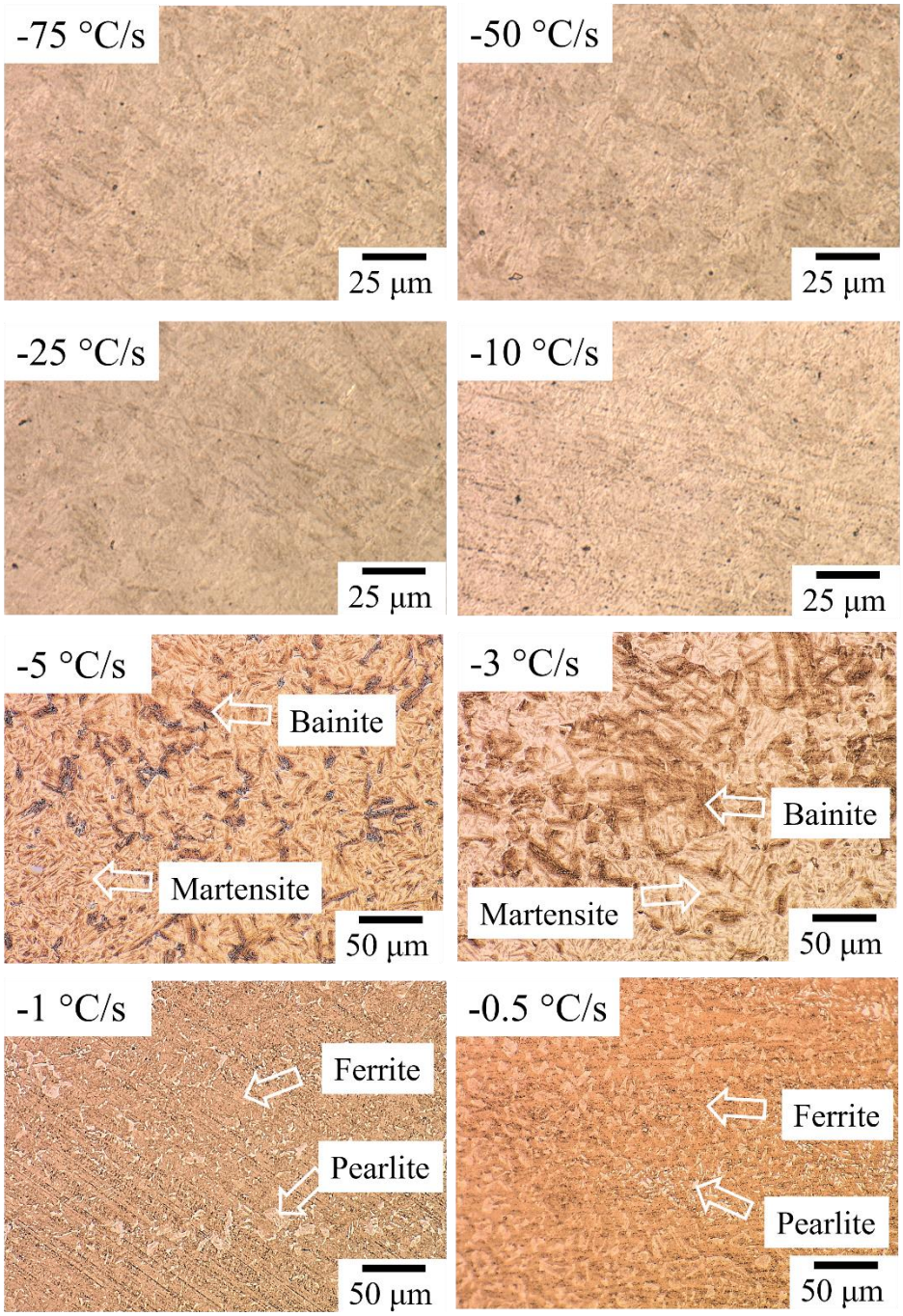

Figure 5.4: Microstructure of the quench dilatometry samples of steel I.

5.2 Microstructural analysis of steel K

Figure 5.5 shows the microstructure of the steel K substrate following DHPF. The microstructures appear largely similar, characterized predominantly by martensite with some discernible ferritic regions. Interestingly, the microstructure is independent of the DHPF temperature.

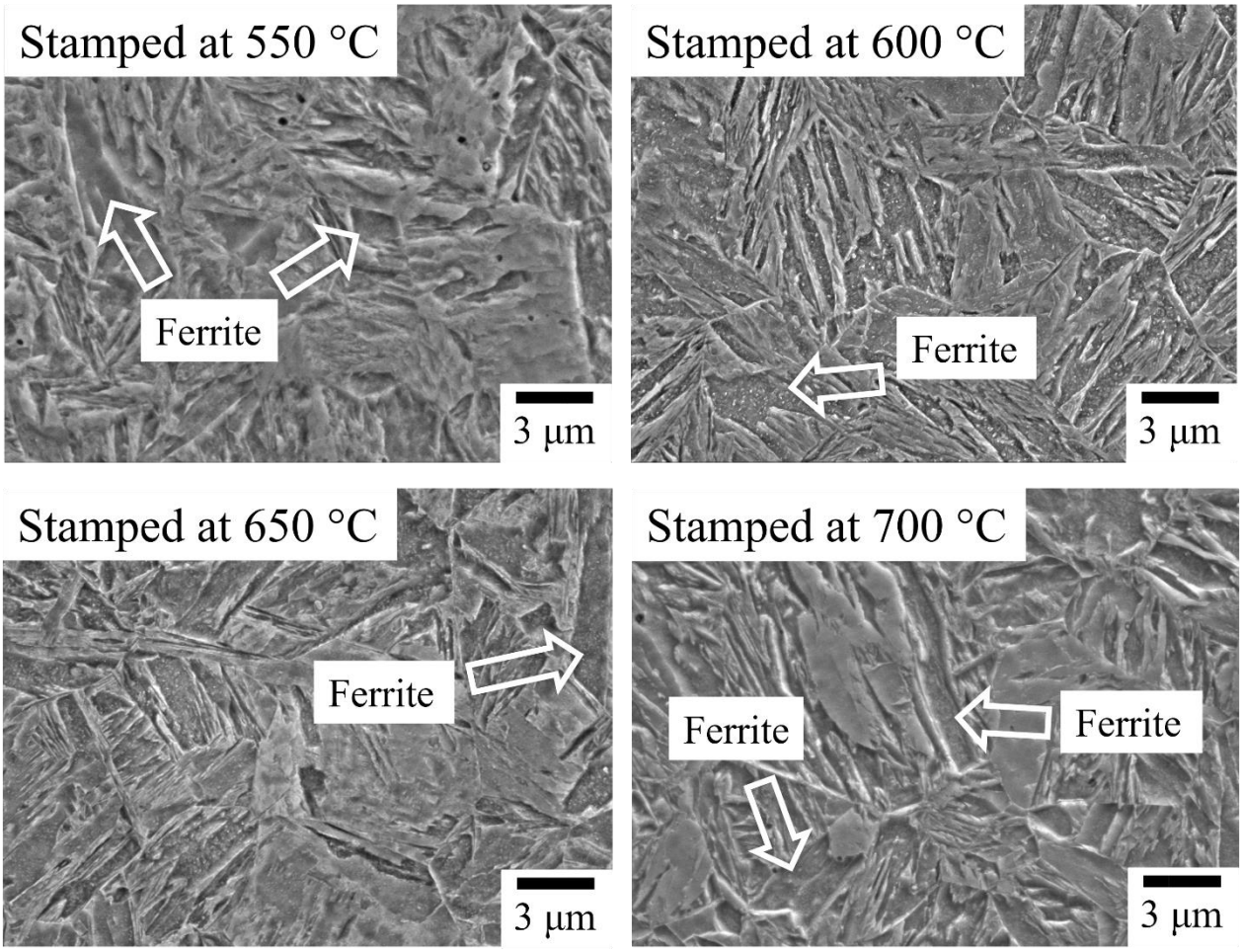

Figure 5.5: Microstructure of steel K after DHPF.

The microhardness results are presented in Figure 5.6.Figure 5.6: Microhardness values of steel K and steel I after DHPF. Notably, all the values observed corresponded with the presence of martensite with small amounts of ferrite. Moreover, no significant differences were observed between the various DHPF temperatures tested in steel K. Steel I had a slightly higher

microhardness than steel K, hinting at the probability of having a slightly higher ultimate tensile strength (UTS). Furthermore, the microhardness results are in agreement with the SEM micrographs, further supporting the findings.

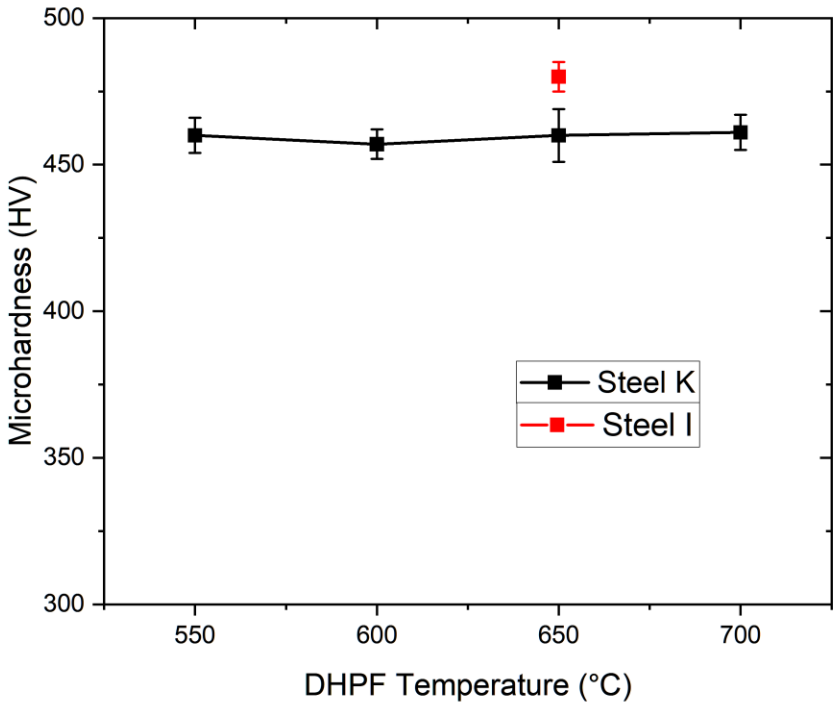

Figure 5.6: Microhardness values of steel K and steel I after DHPF.

Figure 5.7 shows the raw XRD spectra of the DHPF steel K. It is noteworthy that the peaks attributed to martensite represent both martensite and ferrite. Given the low carbon content of steel K (0.2 wt.%), the difference between the lattice parameters c and a in martensite is minimal as it is dependent on the carbon content [7]. Consequently, the observed peaks are sharp and overlap considerably with those of ferrite, making it impractical to differentiate between the two constituents using XRD. The phase fractions of DHPF steel K obtained using XRD as a function of DHPF temperature can be seen in Figure 5.8. It shows that the substrate is mostly comprised of martensite and has small amounts of retained austenite. The retained austenite is caused by the

transformation of austenite (fcc) into martensite (bcc) in low carbon steels [99]. It is known that martensite transformation can never be truly complete. Thus, small volume fractions of interlath retained austenite, depending on the composition of the steel, are present at lath grain boundaries [99], [100]. The interlath films are typically very thin, and cannot be detected by SEM. However, they can be determined by XRD [99], [100], as shown in Figure 5.8. It can be seen that austenite fraction for steel K is negligible, and more importantly, not a strong function of DHPF temperature.

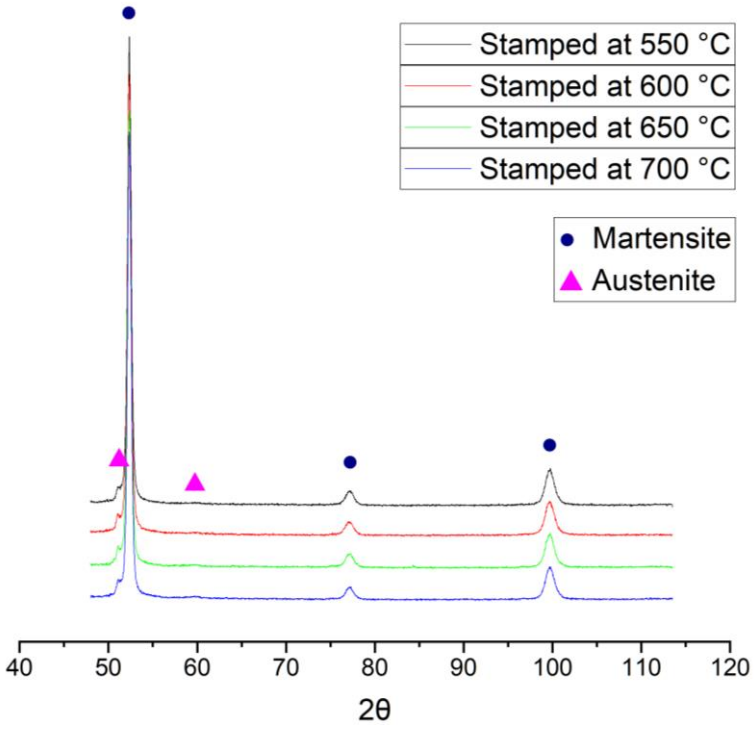

Figure 5.7: XRD spectra from steel K substrate as a function of DHPF temperature.

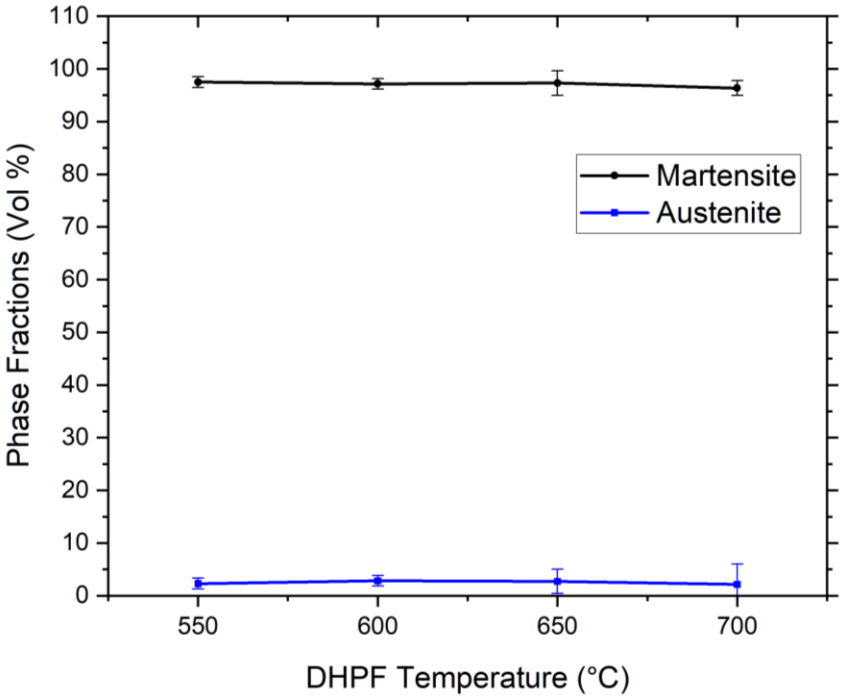

Figure 5.8: Phase fractions of steel K vs DHPF temperature with a 95% confidence interval.

5.3 Coating analysis of Steel K

The microstructural evolution of the coatings was evaluated by conducting SEM-BSE analysis as a function of DHPF temperature. Figure 5.9 (a) shows the cross section of the etched as-received galvannealed coating revealing the microstructure. Two phases have been identified from the SEM micrograph. The coating comprises δ -$FeZn_{10}$ and Γ-Fe_3Zn_{10} in the regions close to the substrate, typical of an industrial galvannealed (GA) coating [47]. Cracks in the coating are attributed to temper rolling, and tension leveling after coating as they are also present in unetched sample, Figure 5.9 (b). DHPF was performed on the as-received panels, as explained in §4.3. The resultant coating microstructures can determine the occurrence of LME or microcracking and help hypothesize about corrosion properties.

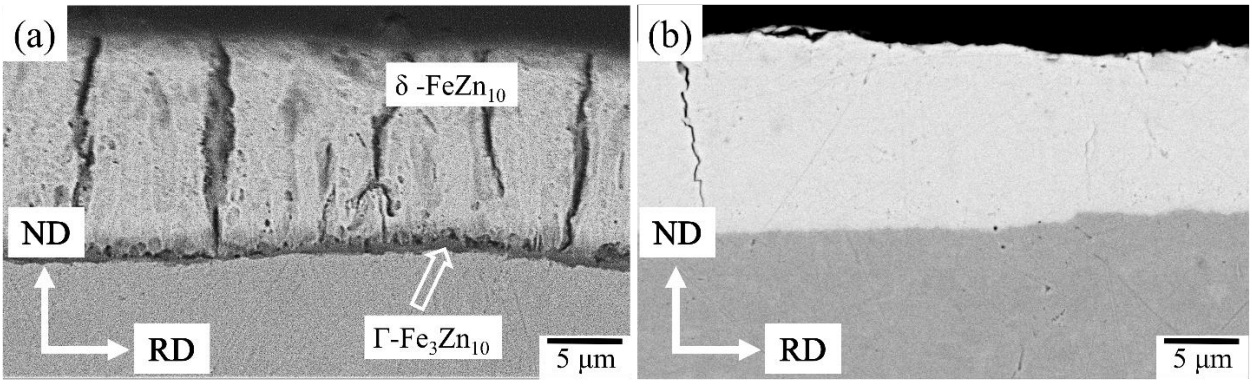

Figure 5.9: Coating microstructure of as received steel K obtained using SEM-BSE (a) etched, (b) uneteched.

In Figure 5.10, the cross-sectional coating microstructure obtained using SEM-BSE for every DHPF temperature is shown. The coatings consist of two phases, Γ-Fe_3Zn_{10} (darker regions) and α-Fe(Zn) (brighter regions), and the substrate is martensitic, as mentioned previously. There were no noticeable differences in the microstructure of the coatings with varying DHPF temperatures. This is attributed to the utilization of transfer times with low duration to achieve DHPF temperatures, which did not allow for adequate time for the diffusion-controlled phase transformation processes to occur. It is evident that the coating exhibits cracks; however, these cracks do not extend into the martensitic substrate – i.e. there was no significant evidence of microcracking or LME. It is important to understand the reason for the observed cracks. Those cracks could be caused by the difference in thermal expansion of the coating and substrate panels during the quenching step since a flat die was used [75]. Moreover, intergranular cracking can be dependent on the α-Fe(Zn) grain boundaries. These grain boundaries are weakened because of a Zn-enriched layer present on the grain boundaries as a result of annealing [51]. This Zn-enriched layer is known to be a preferred path for intergranular cracking in Zn-coated PHS [51].

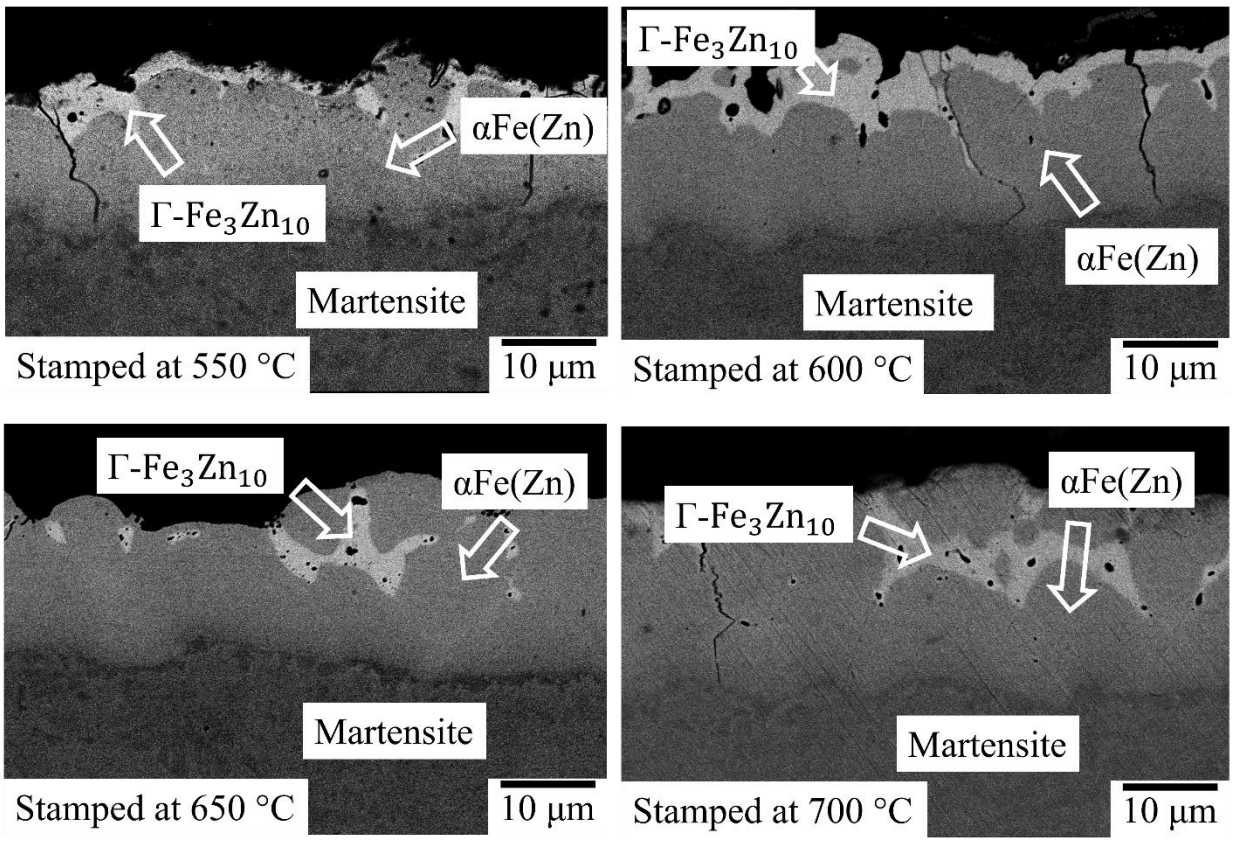

Figure 5.10: Coating microstructure of steel K after DHPF obtained using SEM-BSE.

The phases present in the coatings are produced due to the peritectic reaction, as shown in Equation (5.1), between the α-ferrite phase rich in zinc (α-Fe(Zn)) and the liquid zinc phase rich in iron at 782 °C, as shown by the Fe-Zn diagram in Figure 2.6. Since the Γ-Fe_3Zn_{10} phase is solidified from $Zn(Fe)_{liq}$, it seems that this phase is inclined to amass near the coating surface. Additionally, the absence of microcracks in the coating of the DHPF panels indicates that the occurrence of LME has successfully been avoided in all cases.

$$\alpha\text{-Fe(Zn)} + \text{Zn(Fe)}_{liq} \rightarrow \alpha\text{-Fe(Zn)} + \Gamma - \text{Fe}_3(\text{Zn})_{10} \quad (5.1)$$

A quantitative analysis of the coating phases can provide insights into the corrosion properties. It has been shown that 15 vol% of the Γ-Fe_3Zn_{10} phase is sufficient to yield robust cathodic corrosion

protection [12], [13]. Figure 5.11 shows the phase fractions in the coating as a function of DHPF temperature. Γ-Fe_3Zn_{10}, α-Fe(Zn) and smaller amounts of ZnO have been identified. There is no direct relation between any phase fraction and DHPF temperature, consistent with the observations made from the SEM samples (Figure 5.10). It can be seen in Figure 5.11 that all the DHPF conditions contain more than 15 vol% of Γ-Fe_3Zn_{10}. This amount exceeds the criteria set by Dever et al. [12], indicating promising corrosion properties under the DHPF conditions used.

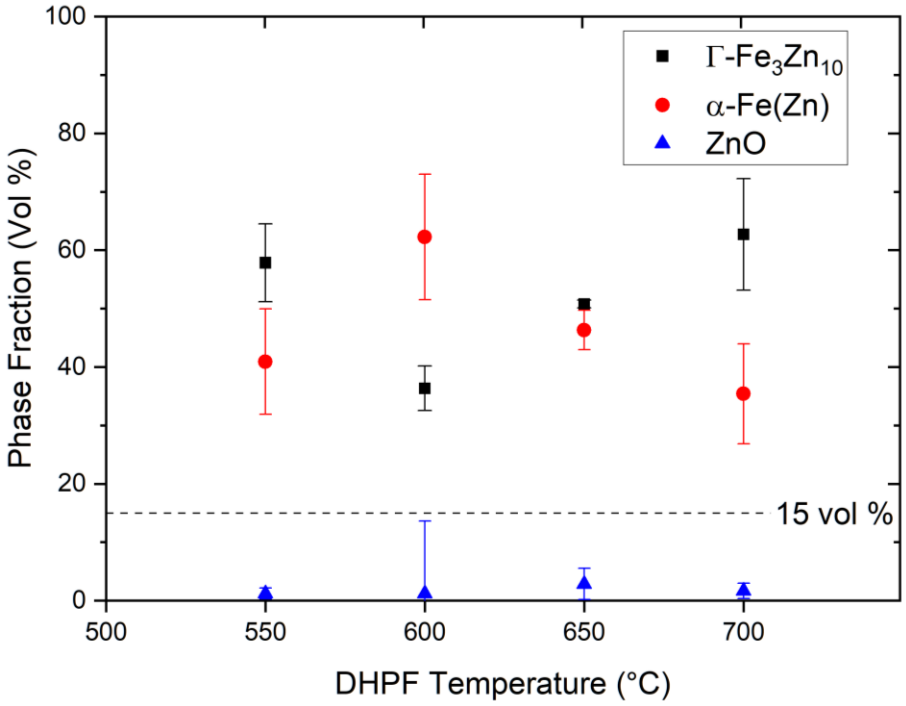

Figure 5.11: Phase fractions of steel K coating vs DHPF temperature.

The obtained microstructure was consistent across all experimental DHPF conditions, which is favorable for three reasons. Firstly, a thorough examination of the SEM micrographs revealed no evidence of LME at any of the DHPF temperatures tested. Thus, all DHPF temperatures with a flat die have avoided LME. Secondly, microcracking was not observed as the microcracks in the coating did not penetrate into the substrate. Lastly, more than 15 vol% of Γ-Fe_3Zn_{10} was

successfully incorporated into the microstructure, which is expected to result in robust cathodic corrosion protection for all DHPF conditions. These observations suggest that the obtained coating microstructure is highly desirable and holds potential for further exploration of corrosion protection by electrochemical testing.

5.4 Mechanical properties

The mechanical properties investigation encompassed the performance of uniaxial tensile tests on the as-received and press formed steel K, as well as press-formed steel I. The purpose of these tests was to assess whether the obtained outcomes met the industrial target properties of an ultimate tensile strength (UTS) exceeding 1400 MPa, a yield strength (YS) of 1000 MPa, and a total elongation (TE) of approximately 5-6%. Figure 5.12 shows the engineering stress strain curve of the as-received steel K prior to DHPF. The as-received steel K exhibited mechanical properties characteristics attributed to an equiaxed ferrite-pearlite microstructure. The material demonstrated an approximate 27% TE, UTS of 644 ± 1.50 MPa, and an average microhardness value of 213 ± 19 HV.

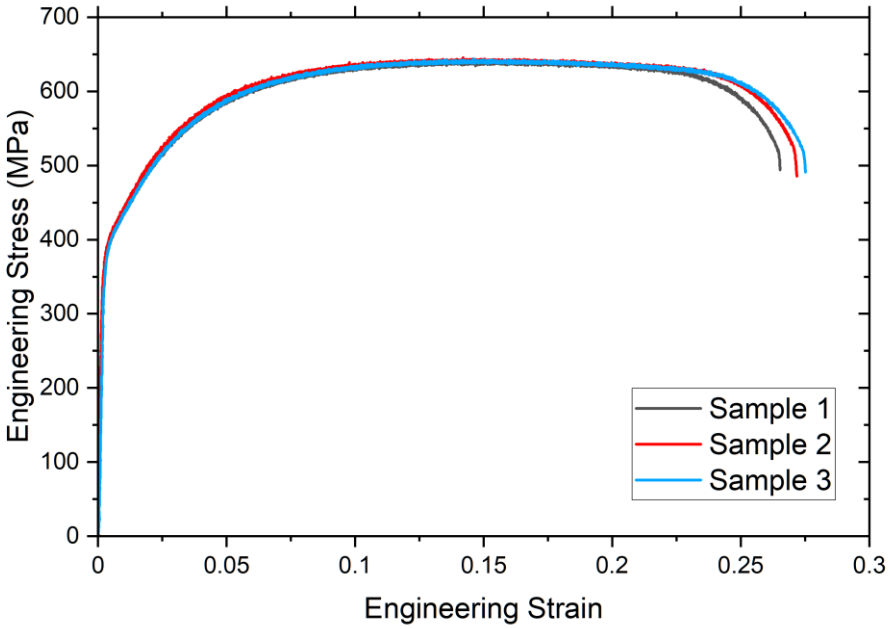

Figure 5.12: Engineering stress-strain curves of as-received steel K.

The engineering stress-strain curves of steel K and steel I for the DHPF temperature of 650 °C are compared in Figure 5.13. Both steels showed similar UTS values of 1501 ± 36 MPa and 1506 ± 13 MPa for steel K and steel I, respectively. The average uniform and total elongation for steel I across all 9 samples were 0.043 ± 0.003 % and 0.089 ± 0.003 %, respectively. These values for steel K were 0.043 ± 0.006 % and 0.081 ± 0.008 %, respectively. This observation indicates similar ductility across both steels. Based on the similarities observed and the fact that the DHPF properties of galvanized steel I have been previously studied by Thomsen [17] and Jewer [16], it was decided to continue with steel K. Moreover, it would be of interest to conduct analysis on the DHPF properties on a galvannealed coating which steel K possesses.

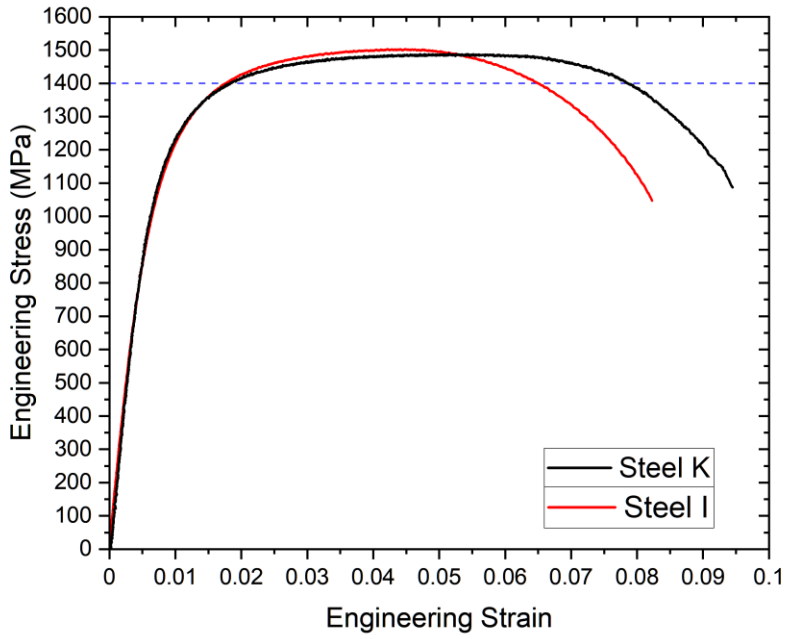

Figure 5.13: Representative engineering stress-strain curves of steel K and steel I at the 650 ℃ DHPF temperature.

Typical uniaxial engineering stress strain curve for the four DHPF temperatures used are plotted in Figure 5.14. The curves are consistent with the industrial UTS target of 1400 MPa, which is indicated by the dashed red line. It is evident from the graph that the sample quenched at 700 °C exhibited a lower tensile curve compared to the others. Further analysis of the mechanical properties can be found in Figure 5.15 (a), where UTS is presented as a function of DHPF temperature. The error bars represent 95% confidence interval of the mean obtained by triplicate testing. It can be seen that, for the samples stamped at 550 °C, 600 °C, and 650 °C, the target UTS of 1400 MPa was achieved as the 1400 MPa target lies below the error bar region. The exact values of which are 1485 ± 29 MPa, 1480 ± 27 MPa, and 1501 ± 36 MPa, respectively. However, the UTS of the sample stamped at 700 °C is 1426 ± 22 MPa. The DHPF temperature of 700 °C meets

the target of 1400 MPa, as well. Furthermore, the UTS values are consistent with the SEM micrographs shown in Figure 5.5, which consisted of a martensitic substrate.

Figure 5.15 (b) shows yield strength (YS) as a function of DHPF temperature. The values of YS for the DHPF temperatures of 550 °C, 600 °C, 650 °C, and 700 °C are 1145 ± 11 MPa, 1104 ± 29 MPa, 1126 ± 38 MPa, and 1096 ± 36 MPa, respectively. It can be observed that YS does not change significantly with varying DHPF temperature. Overall, YS exceeded the industrial target 1000 MPa.

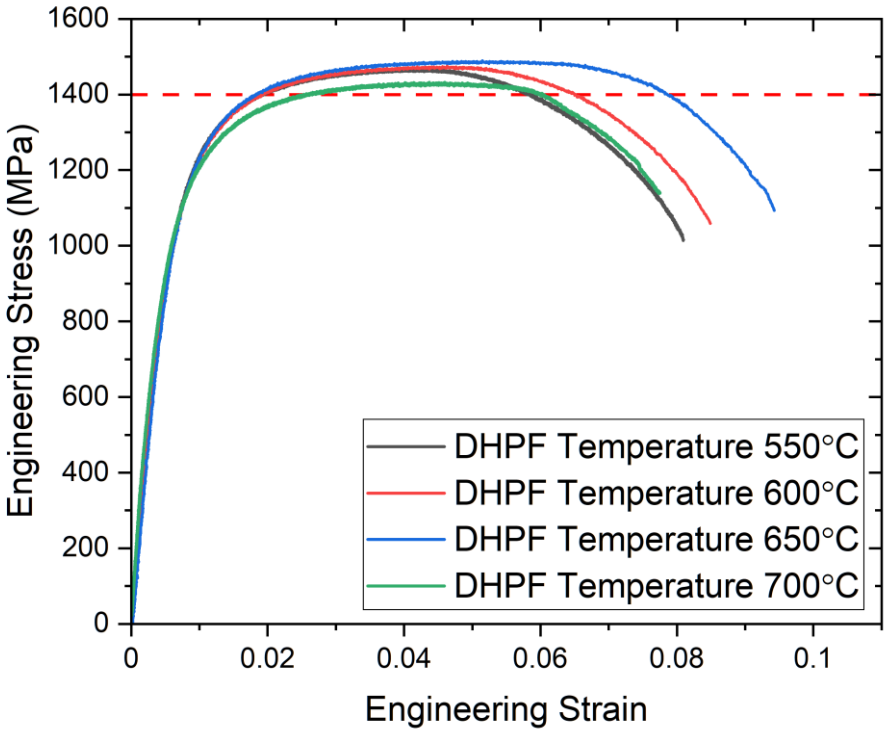

Figure 5.14: Typical engineering stress-strain curves of DHPF temperatures

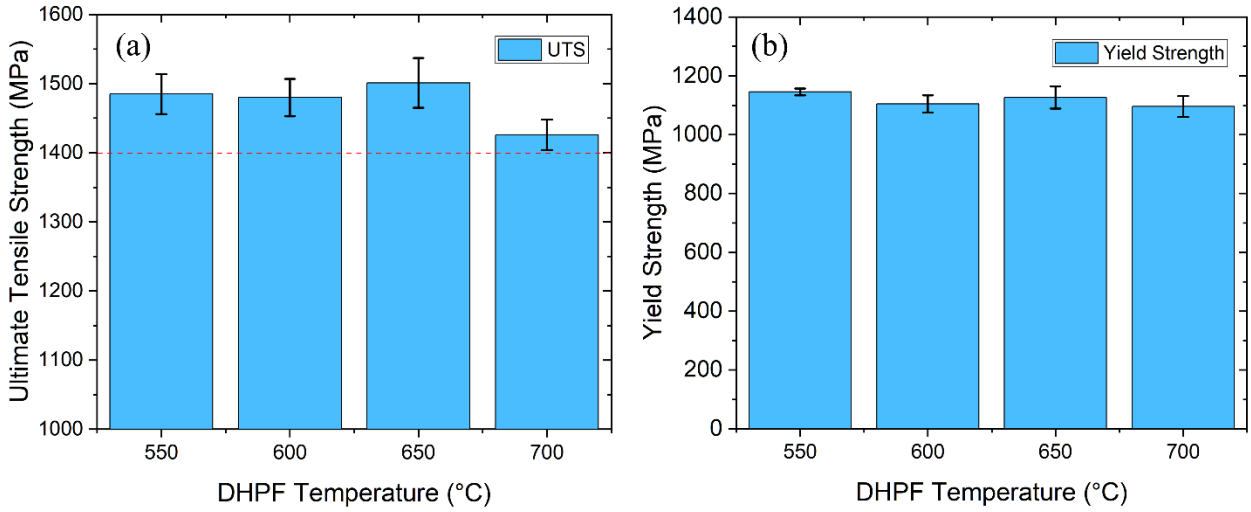

Figure 5.15: (a) Ultimate tensile strength (UTS) and (b) yield strength (YS) of steel K as a function of DHPF temperature.

Uniform elongation and post-uniform elongation of steel K are plotted against DHPF temperature in Figure 5.16 using engineering stress-strain data. As observed, the uniform elongation results are consistent across all DHPF temperatures, with an average value of 0.046 ± 0.003. Notably, the DHPF temperature of 550 °C exhibits a slightly lower uniform elongation compared to the remaining temperatures. Furthermore, the high total elongation with an average of 0.07+ ± 0.004 exhibited by the samples is another indication that LME had been successfully avoided.

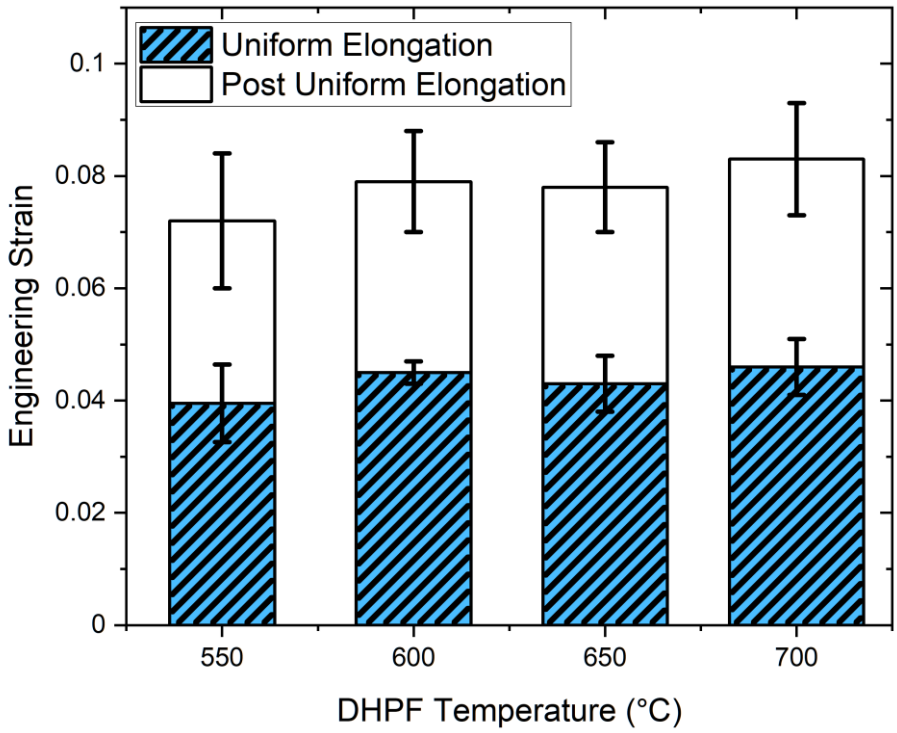

Figure 5.16: Uniform elongation and post uniform elongation of steel K as a function of DHPF temperature.

The graphs in Figure 5.17 display the true stress-strain behavior of steel K under varying DHPF temperatures, along with their corresponding fracture points. Of particular interest is the consistent occurrence of high strain at fracture across all conditions. The substantial plastic deformation observed suggests that failure cannot be attributed to LME, LME leads to catastrophic brittle failure.

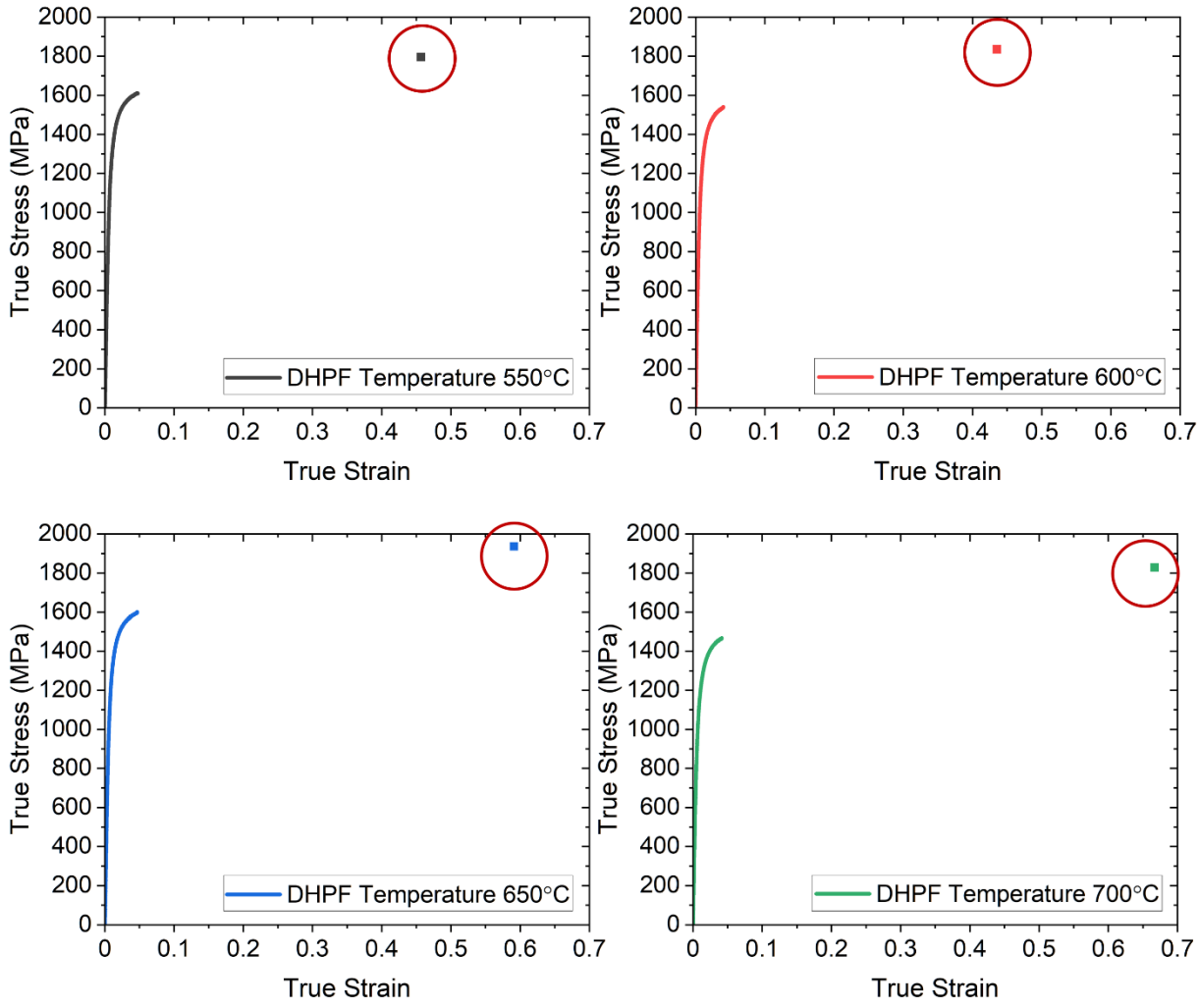

Figure 5.17: True stress-strain curves of steel K for DHPF temperatures used with fracture points highlighted.

To further explore the possibility of LME occurrence, tensile coupons were examined in the SEM. Figure 5.18 displays unetched SEM-BSE micrographs captured from the neck region of the coupons. The micrographs reveal a multitude of cracks in the region, with some propagating into the substrate as a result of high strain that region experiences during tensile testing. It can be seen that these cracks are blunted, which can be explained by microcracking mechanism. It is known that microcracks grow along Zn-enriched prior austenite grain boundaries in the substrate.

Microcracks become blunt when the Zn-enrichment along prior austenite grain boundaries is exhausted [51], [86]. Since the microcracks have not penetrated deep into the substrate it can be said that severe microcracking was not observed. Based on the micrographs in Figure 5.18, no discernible differences among the DHPF temperatures were observed.

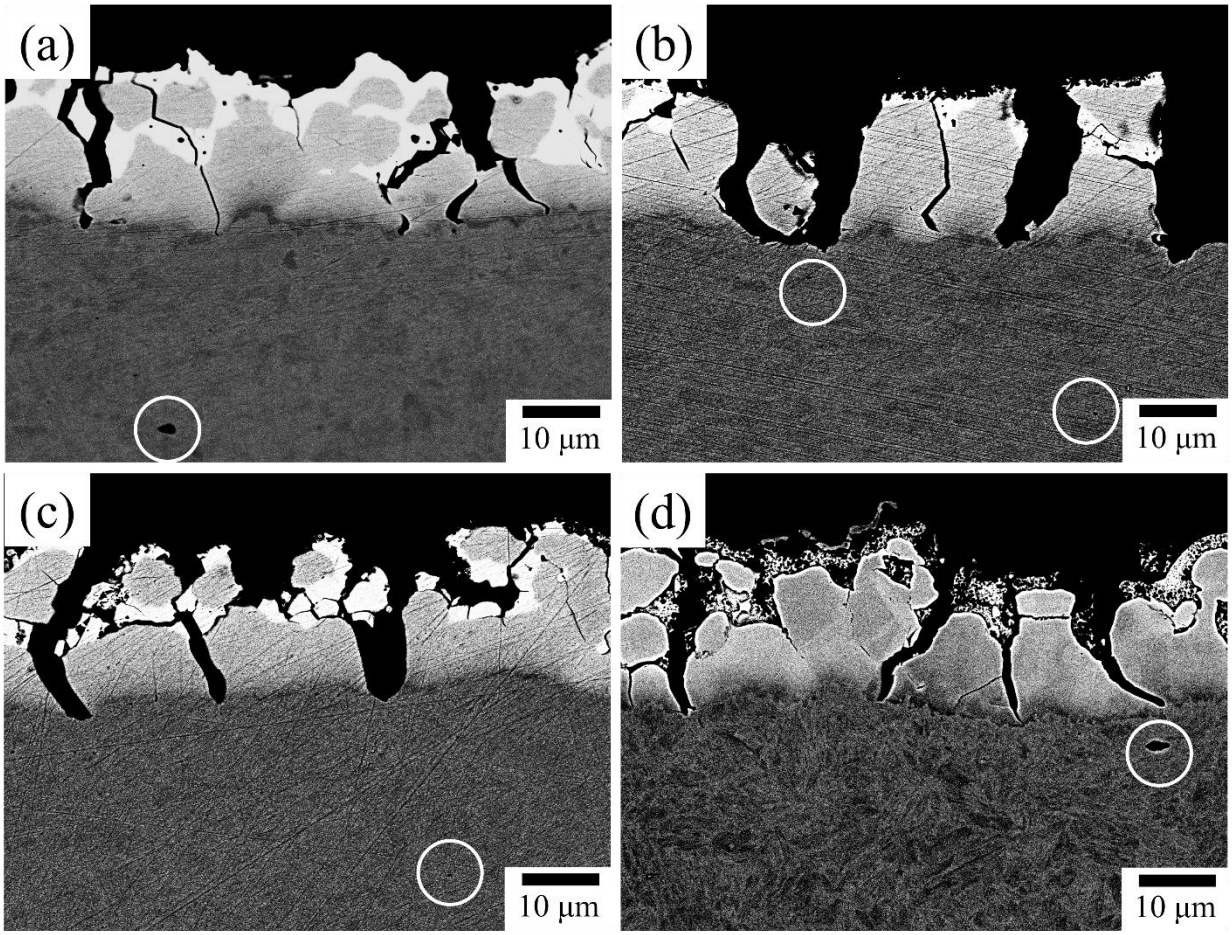

Figure 5.18: SEM-BSE micrographs obtained from the neck region of steel K tensile coupons at following DHPF temperatures: (a) 550 °C, (b) 600 °C, (c) 650 °C, and (d) 700 °C.

Additionally, several voids of varying sizes, including some that have coalesced, can be seen in Figure 5.18. These voids are more easily seen in Figure 5.19, which shows the neck region and fracture line of DHPF steel K at 700 °C. Coalesced voids, which are shown by red arrows, can be

seen in close proximity to the fracture line. Blue arrows show smaller voids prior to coalescence. The fracture is most likely attributed to void coalescence rather than microcrack propagation or especially liquid metal embrittlement.

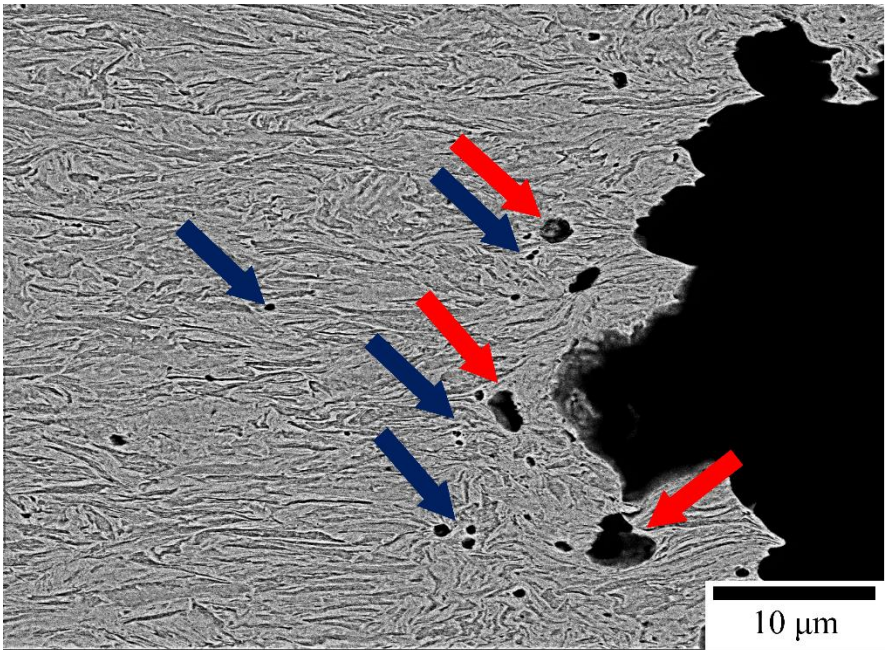

Figure 5.19: SEM-BSE micrograph showing the neck region of tensile coupon of DHPF steel K at 700 °C.

Figure 5.20 presents unetched SEM-BSE micrographs captured from the uniform elongation region of the tensile coupons. In this region, voids are observed, although they are not as prevalent as in the neck region. Cracks on the coating, on the other hand, were narrower and did not propagate into the substrate. Overall, the examination did not reveal any noticeable differences among the DHPF temperatures. By correlating the findings from Figure 5.18 and Figure 5.20 with the analysis on tensile data, it can be concluded that LME and microcracking have not occurred for any of the DHPF temperatures.

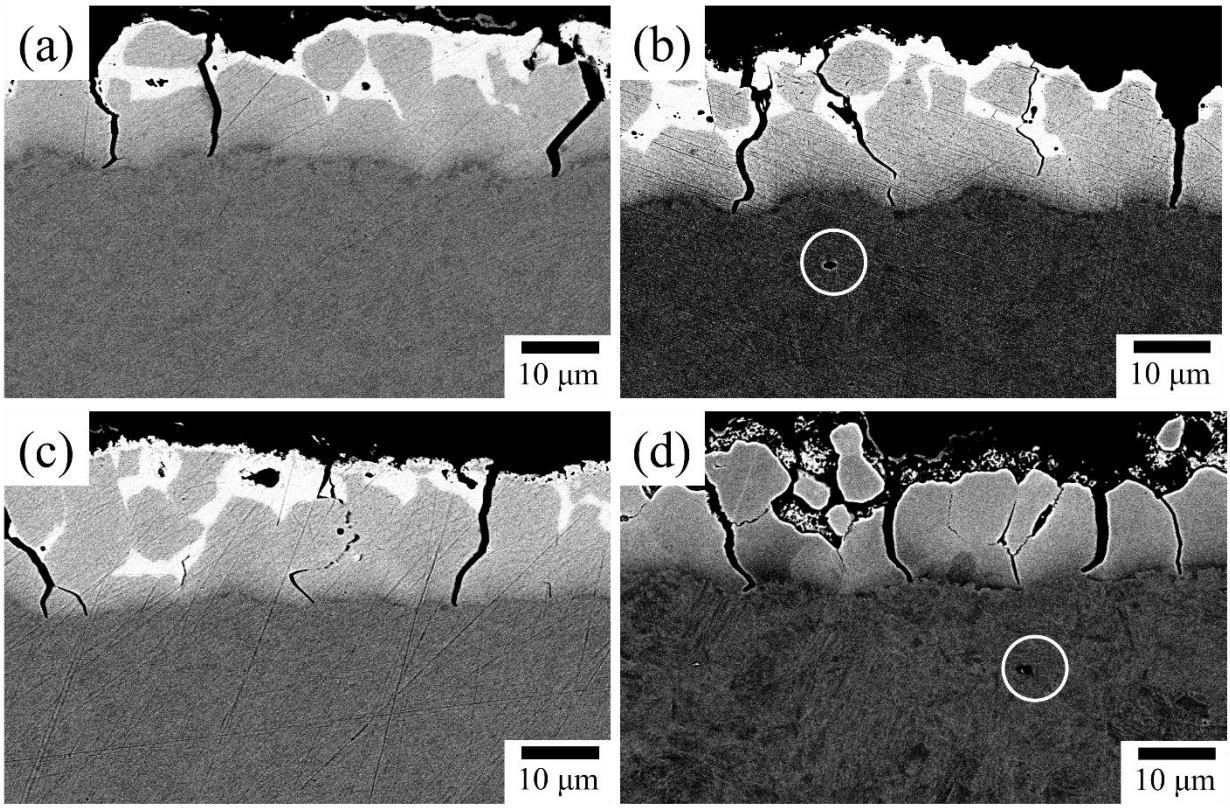

Figure 5.20: SEM-BSE micrographs obtained from the uniform elongation region of steel K tensile coupons at following DHPF temperatures: (a) 550 °C, (b) 600 °C, (c) 650 °C, and (d) 700 °C.

5.5 Mechanical Properties of Pilot-scale DHPF of Steel K

Representative engineering stress-strain curves of pilot-scale DHPF of steel K for austenitization time of 120 s can be seen in Figure 5.21. The curves are similar across all experimental DHPF temperatures. Most importantly, it should be noted all of the DHPF temperatures met the intended UTS target of 1400 MPa. It is interesting to note that the curves from the tensile coupons excised from top of the U-shaped part were similar to those excised from the side of the part. The observed high elongations suggest the absence of LME and microcracking both in the top region of the sample and in the side, where the forming process imposes strains.

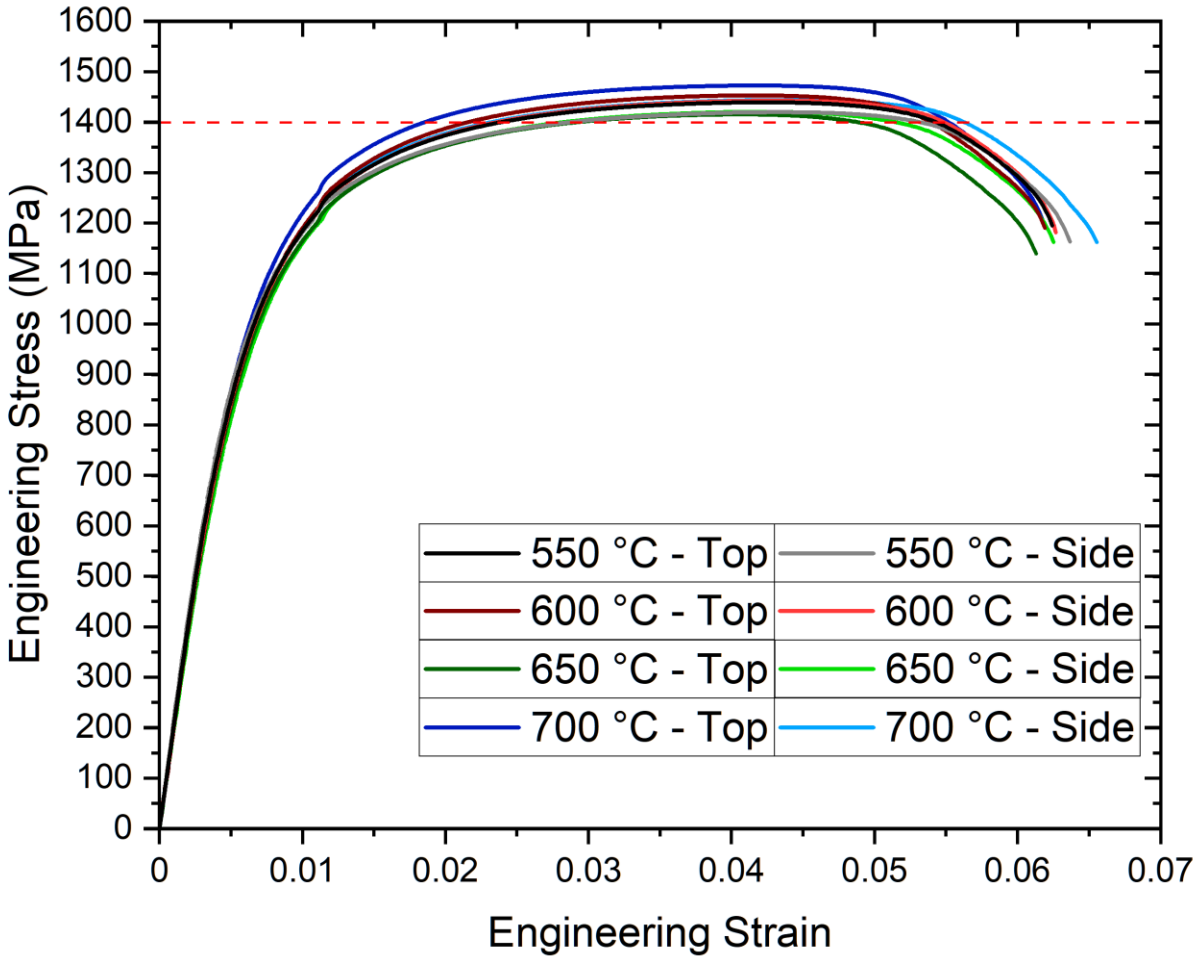

Figure 5.21: Engineering stress-strain curves of pilot-scale DHPF of steel K for austenitization time of 120 s.

Figure 5.22 shows the mechanical properties, specifically UTS and YS, for the austenization times used as a function of DHPF temperature. Error bars represent the standard deviation of the data. It can be seen that the UTS target of 1400 MPa was met for all of the DHPF temperatures for any given austenitization time. The average UTS value for austenitization times of 120 s among all DHPF temperatures was 1430 ± 28 MPa for the top section and 1429 ± 21 MPa for the side section, Figure 5.22 (b). The average YS value for austenitization time of 120 s amongst all DHPF

temperatures was 993 ± 86 for the top region and 1001 ± 35 for the side region. It can be said that YS met the target of 1000 MPa, as well. However, it should be considered that the target is not exceeded by a considerable amount. Furthermore, the UTS and YS values for each DHPF temperature, for a specific austenitization time, exhibit consistency, thereby indicating that the mechanical properties are not affected by the DHPF temperature. Thus, it can be understood that using an extended transfer time for GA-coated steel K is a robust process and can result in the target mechanical properties over a range of austenitization times (60-240 s) and DHPF temperatures (550-700 °C).

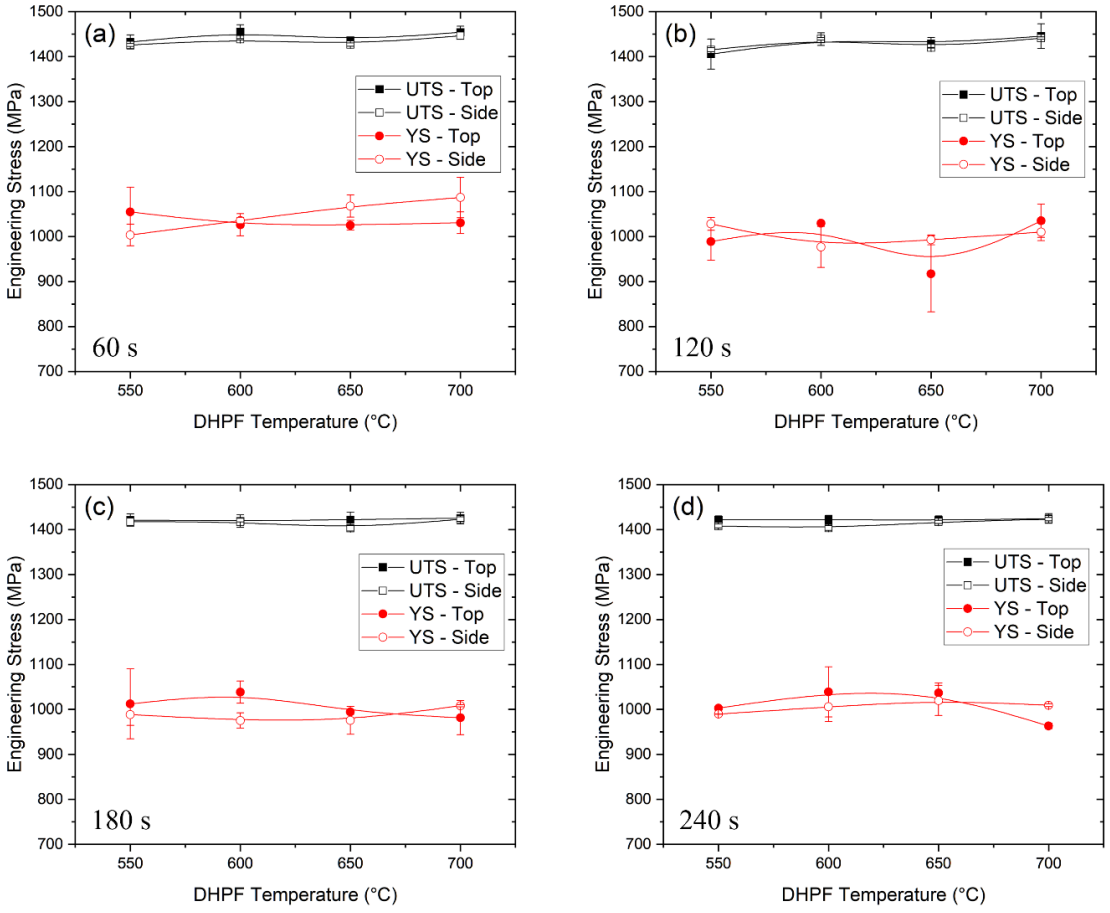

Figure 5.22: Average mechanical properties for pilot-scale DHPF of steel K shown as a function of DHPF temperature for austenitization times of (a) 60 s, (b) 120 s, (c) 180 s, (d) 240 s.

Total Elongation (TE) at fracture is divided into two bars of uniform elongation (UE) and post-uniform elongation (PUE) in Figure 5.23. Elongation is presented as a function of DHPF temperature, and the error bars correspond to the standard deviation of the values. The UE of the top and side of the part were consistent and independent of DHPF temperature. A minimum of 4% UE followed by significant PUE was observed for all the conditions. A slight difference can be observed between TE values from the top and the wall. The average TE for the top was lower than for the side for most of the tested conditions. The high observed PUE in all conditions indicates two things. Firstly, it indicates that microcracking did not occur. Secondly, LME has been avoided, since LME would have resulted in little to no plastic deformation before catastrophic fracture [101].

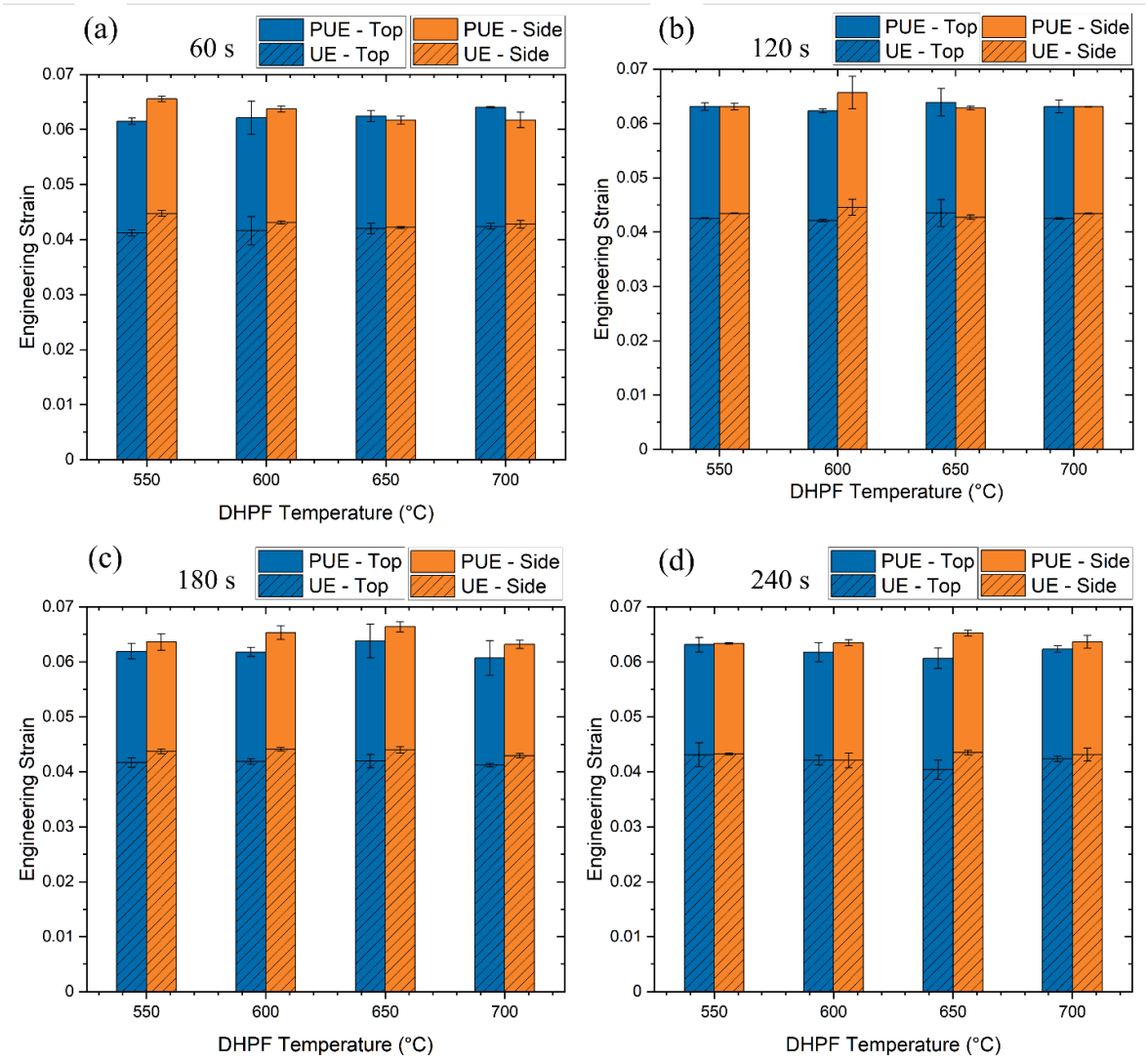

Figure 5.23: Average uniform elongation (UE) and post-uniform elongation (PUE) for pilot-scale DHPF of steel K as a function of DHPF temperature for austenitization times of (a) 60 s, (b) 120 s, (c) 180 s, (d) 240 s.

Figure 5.24 summarizes the mechanical properties as a function of austenitization time at the DHPF temperature of 650 °C for simpler analysis. UTS values, shown in Figure 5.24 (a), were independent of the austenitization time, with an average of approximately 1430 MPa. YS, however, is slightly lower for the austenitization time of 120 s in comparison to other times. YS

and UTS were similar among the top and side region. It can be seen in Figure 5.24. (b) that for austenitization times higher than 120 s, the UE and TE are slightly higher for the side of the sample in comparison to the top. These variations can be investigated by thorough microstructural analysis.

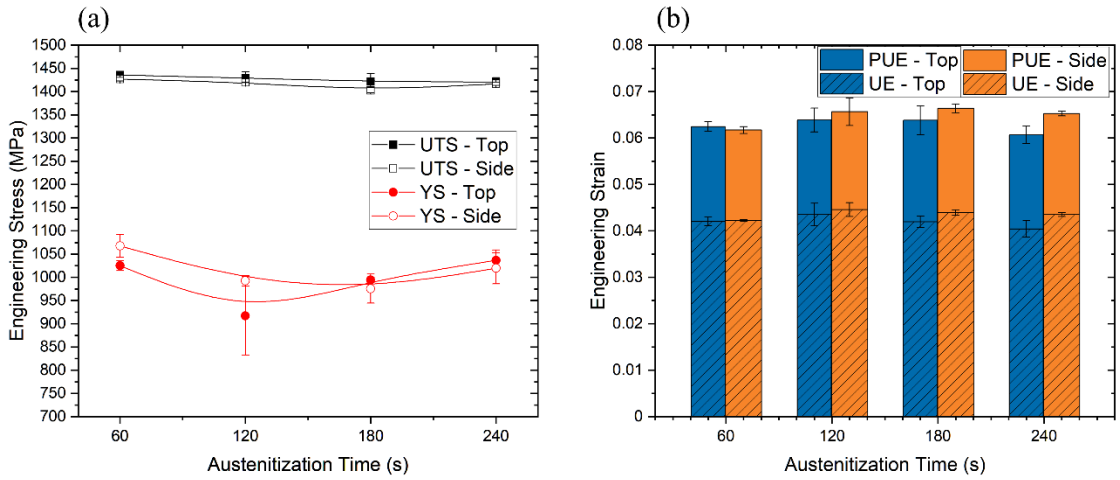

Figure 5.24: Mechanical properties for DHPF steel K at DHPF temperature of 650 °C as a function of austenitization time (a) UTS and YS (b) UE and PUE.

In summary, the GA steel K showed similar mechanical properties across all tested DHPF temperatures with and exception of 700 °C. It was shown that an average UTS value of 1480 MPa was met for DHPF temperatures of 550 °C, 600°C, and 650 °C, which was slightly higher than that of 700 °C (Figure 5.15 (a)). YS values were consistent for all conditions. The UE and PUE were similar for all conditions. Specifically, an average UE of 4.6 % was observed. Mechanical properties were correlated to the microstructure which consisted mainly of martensite with small ferrite regions. A microstructural investigation of the tensile coupons showed blunted microcracks and voids near the fracture surface. Hence, indicating that fracture was not severely affected by DHPF. Coating microstructural analysis revealed that two phases of Γ-Fe_3Zn_{10} and α-Fe(Zn) were

present. Deep microcracks and LME were not observed in the coating. XRD results showed that all the DHPF conditions had more than 15 vol% of Γ-Fe_3Zn_{10}., implying promising corrosion protection [12]. Pilot-scale trials showed a similar trend of independence on DHPF temperature for the mechanical properties. The UTS exceeded the target of 1400 MPa for all the DHPF conditions tested. Moreover, YS met the target of 1000 MPa. Similar to the laboratory-scale study, consistent high values for elongation were observed in the pilot-scale trials. Moreover, the austenitization times tested did not affect the mechanical properties.

6 Discussion

The feasibility of producing GA-coated prototype PHS parts (0.19C-1.92Mn-0.2Si-0.003B (wt.%)) with adequate mechanical properties that avoid LME by using an extended DHPF transfer time was determined. To this end, panels were austenitized at 890 °C for 120 s and stamped at temperatures between 550 – 700 °C. The substrate transformed into a lath martensite microstructure with small amounts of ferrite, due to the high cooling rate and chemical composition of the prototype alloy. The effect of process parameters on the properties is discussed below.

6.1 Effect of DHPF Temperature on Mechanical Properties

Two alloys, steel I and steel K, were considered for this study, the chemical compositions of which were 0.20C-1.96Mn-0.25Si-0.003B-0.01Ti, and 0.19C-1.92Mn-0.20Si-0.003B-0.03Ti (wt.%), respectively. The primary difference between these alloys was the galvannealed coating present on steel K, in contrast to the absence of any coating on steel I and their Si content, which was higher for steel I by 0.05 wt.%. The CCT diagram of steel I was shown in Figure 5.4. It was shown that a critical cooling rate of 10 °C/s was necessary for a full martensite transformation. By comparing the CCT diagram of steel I (Figure 5.3) to the CCT diagram of 22MnB5 (Figure 2.2), it can be seen that the hardenability has been significantly improved. The critical cooling rate for 22MnB5 for producing a fully martensitic microstructure was 30 °C/s, whereas the critical cooling rate for steel I was 10 °C/s. This was supported by the microhardness data that was provided in the diagram and the microstructures shown in Figure 5.5. Interestingly, microhardness continued increasing in the fully martensitic region by roughly 20 HV between the cooling rates of 10 – 75 °C/s. A similar trend was observed in the literature [14], [15], [17]. Thomsen et al. [17] reported an increase of 17 HV between the cooing rates of 25 – 75 °C/s for their 2.5%Mn prototype alloy

(§2.8). Kurz et al. [14] likewise reported an increase of 13 HV between the cooing rates of 40 °C/s and 220 °C/s for 20MnB8 (§2.5.4). This can be explained by subtle microstructural variations. Figure 5.5 shows slight amounts of bainite present in the microstructure at cooling rates of 10 °C/s and 25 °C/s. Thus, the importance of using a high cooling rate during DHPF is emphasized.

A comparison of the engineering stress-strain curves of steel I and steel K after austenitization at 890 °C for 120 s and a DHPF temperature of 650 °C is shown in Figure 5.13. It was shown that these alloys exhibited comparable tensile properties, namely similar tensile strengths and ductilities. The microhardness was slightly higher for steel I than steel K, Figure 5.6. This can be attributed to the higher Si content, which provides solid solution strengthening [33]. This shows that the mechanical properties such as UTS are linked to the microstructure of these alloys, which is predominantly martensite in both cases. Thus, it was interesting to continue with the GA coating in various DHPF temperatures to determine a process window for this technique, especially as GI coatings have previously been studied [15]–[17]. Furthermore, a pilot-scale DHPF trial of GA steel K was conducted at Gestamp, the details of which were provided in §5.5.

The tensile properties including UTS and YS for laboratory-scale testing for steel K were shown in Figure 5.15. It was observed that YS was not a strong function of DHPF temperature, with the average values for each DHPF temperature ranging between 1096 – 1145 MPa. The UTS for the DHPF temperatures of 550°C, 600 °C, and 650 °C was not a strong function of the temperature, as the average ranged between 1480 – 1501 MPa. The UTS and YS both significantly exceeded the targets set, specifically 1400 MPa for UTS, and 1000 MPa for YS, for all DHPF temperatures. Thus, it can be said that the relatively wide temperature range of 550 – 700 °C provides a suitable process window for the DHPF of GA steel K. As seen in Figure 5.15., the UTS for the DHPF temperature of 700 °C was slightly lower than the DHPF temperatures. Comparing the mechanical

properties of the laboratory-scale tests for the GA-coated steel K in conjunction with the pilot-scale results can offer valuable insights and elucidate the matter at hand. Furthermore, both uniform and post-uniform elongations were comparable among all DHPF temperatures, Figure 5.16. The relatively high amounts of total elongation observed (~ 0.075) is desirable as it means that LME did not occur [34], [58], [59].

Pilot-scale trials for the GA-coated steel K, Figure 2.23, showed that UTS and YS are not significantly dependent on DHPF temperature, regardless of whether samples were excised from the top or the side of the U-shaped part (Figure 2.25). The consistent and high values of UTS, as shown in Figure 2.23, indicate that austenitization has been completed for times higher than 60 s. This is in agreement with the work of Thomsen et al. who stated that austenitization had been completed for two GI prototype PHS alloys with Mn contents of 2% and 2.5%, as discussed in §2.8 (Figure 2.24). Similarly, all the samples shared consistent levels of ductility as a function of DHPF temperatures. Most importantly, it is evident from these results that the UTS target of 1400 MPa was met for all the DHPF temperatures and the austenitization times tested, as the UTS values ranged from 1403 – 1455 MPa with an average of 1430 MPa. Ductility and tensile strength were not affected by the austenitization times tested, as shown in Figure 5.24. The slight variations can be investigated by microstructural analysis. The TE values suggest that LME and severe microcracking were not observed in the pilot-scale, either. The independence of mechanical properties on DHPF temperature is in agreement with Thomsen et al. [15]. They performed DHPF on two prototype steels on temperatures ranging from 600 – 700 °C and did not see a significant dependance of the mechanical properties. Overall, it can be said that, for steel K, the UTS values for the four DHPF temperatures tested were relatively similar, and most importantly, the specified target mechanical properties were met.

Figure 6.1 shows representative engineering stress-strain curves for lab-scale and pilot-scale trials for steel K, which were both austenitized at 890 °C for 120 s and stamped at 650 °C. The pilot-scale trial curve shown is from the top of the part as it has experienced similar forming stress to the laboratory flat die. It is evident from Figure 6.1 that UTS and YS are significantly lower for the pilot-scale in comparison to the lab-scale. Figure 6.2 provides a comprehensive comparison between the steel K mechanical properties for all DHPF temperature for an austenitization time of 120 s. Figure 6.2 (a) shows that the UTS for DHPF temperatures of 550 °C, 600 °C, and 650 °C were slightly higher for the lab-scale tests compared to the pilot-scale tests. However, the UTS of the sample stamped at 700 °C is consistent in both conditions. The average uniform elongation is similar between both pilot and lab scale across all DHPF temperatures, as shown in Figure 6.2 (b). Total elongation (TE), however, was significantly lower in the pilot-scale trials.

The differences between the lab-scale and pilot-scale steel K trials can be attributed to various causes. The sample size used in the pilot-scale had a gauge length of 50 mm as opposed to 25 mm for the subsize samples which were used in the laboratory. All the samples were excised according to ASTM E8 [94]. It is known that the specimen dimensions can affect the elongation as the probability of having flaws in larger samplers is higher [102]. ASTM E8 [94] suggests that the ratio of $L/\sqrt{A}$ should be constant to ensure comparable elongations, where L is the gauge length of the specimen and A is the original cross-sectional area of the specimen. It also states that specimens with lower $L/\sqrt{A}$ ratios generally produce higher elongation values. This ratio for laboratory-scale and pilot-scale tests for steel K were 9.1 and 12.9, respectively. Furthermore, ISO 6892-1 [103] suggests keeping a constant value of between 4 – 5 for the L/W ratio, with L being the gauge length and W being the width of the specimen. The L/W ratio for laboratory-scale tests

and pilot-scale tests for steel K were 4.2 and 4, respectively. Thus, the difference in the elongation values can be explained.

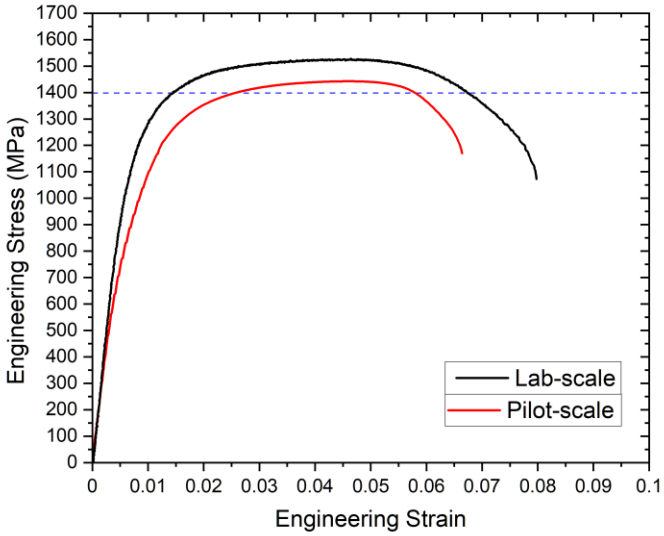

Figure 6.1: Representative engineering stress-strain curves for steel K for lab-scale and pilot-scale trials both austenitized at 890 °C for 120 s and stamped at 650 °C.

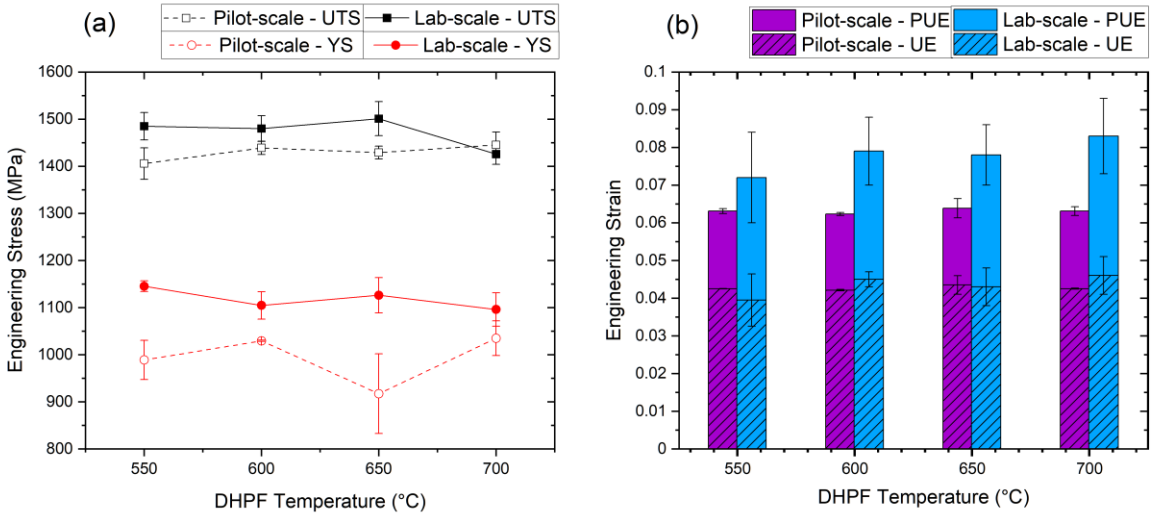

Figure 6.2: Comparison of mechanical properties for steel K between pilot-scale and lab-scale tests both of which were austenitized at 890 °C for 120 s: (a) UTS and YS comparison, (b) UE and PUE comparison.

It should be emphasized that LME or microcracking have not occurred based on several key reasons. Firstly, high total elongation was observed for both laboratory-scale tests and pilot-scale tests that is not characteristic of LME-induced failure, as shown in Figure 5.16 for laboratory-scale testing and Figure 5.23 for pilot-scale testing [53], [54]. The second reason would be the lack of microcracks in the coating micrographs, as shown in Figure 5.10. The lower UTS level cannot be caused by microcracking because no cracks penetrating the substrate were observed in Figure 5.10. This is in agreement with the observations by Thomsen et al. [15], [17] as they did not report LME or microcracking for their prototype alloys after DHPF at lower temperatures.

Furthermore, from the SEM micrographs obtained from the tensile samples (Figure 5.19), it was observed that voids were present in the region close to the neck, indicating that void coalescence was the present failure mechanism, characteristic of ductile failure [99]. This is in agreement with the observation of cup and cone features in the fracture surface by Thomsen et al. for a GI 2%Mn prototype steel [15], [17]. It should be noted that some blunted microcracks were observed as well, however, they were not deep. They were associated to both the high tensile strains experienced by the samples and weak Zn-enriched α-Fe(Zn) and prior austenite grain boundaries [51], [86]. In summary, it was observed that LME was successfully avoided for all DHPF temperatures.

6.2 Effect of DHPF Temperature on Coating Properties

It is known that during austenitization at 890 °C Zn coatings melt and alloy with the substrate. These phase transformations affect the coating microstructure significantly and have been the subject of many studies [2], [4], [48]. SEM micrographs of GA steel K after DHPF, Figure 5.10, showed that the coating had transformed to Γ-Fe_3Zn_{10} and α-Fe(Zn). It was observed that Γ-Fe_3Zn_{10} was located mostly on the outer layer of the coating. The is can be explained by transformations during DHPF. It has been shown that upon heating, Zn coatings transform into Γ-

Fe_3Zn_{10} by 700 °C. Thus, after the peritectic temperature of 782 °C, the coating consists of a liquid Zn(Fe) with the composition of Γ-Fe_3Zn_{10}. As a result of inward diffusion of Zn from the liquid Zn(Fe) during annealing, α-Fe(Zn) is formed [2], [4], [48]. Hence, α-Fe(Zn) is interfacing with the substrate. This was expected as other studies indicate that austenitization time of 120 s is not sufficient for the full transformation of Γ-Fe_3Zn_{10} into α-Fe(Zn) for GI70 coatings. Dever et al. have shown that 15 vol% of Γ-Fe_3Zn_{10} in Zn-coated 22MnB5 is required for robust cathodic corrosion protection, as shown by galvanostatic corrosion kinetics in Figure 2.23 (§2.8) [12], [13]. XRD results in conjunction with micrographs, Figure 5.11 and Figure 5.10, showed that at least 35 vol% Γ-Fe_3Zn_{10} was present in the coating after DHPF, which exceeds the 15 vol% criterion. Thus, desirable corrosion properties are expected for all DHPF temperatures tested.

Another feature observed in SEM micrographs for the coating in Figure 5.10 was cracks. They were partly associated with the thermal expansion coefficient difference in the coating and the substrate, which during quenching in the flat die can cause cracks [75]. Evidence for LME and microcracking was not found since the cracks did not propagate into the substrate. An additional reason for the observed cracks can be intergranular cracking on the α-Fe(Zn) grain boundaries. It was shown by Maleki et al. [51], [86] that Zn diffuses into the α-Fe(Zn) grain boundaries in the coating, as well as austenite grain boundaries in the substrate during austenitization, forming a Zn-enriched layer on the grain boundaries. Hence, it is suggested that after DHPF in a flat die, cracking occurs on the α-Fe(Zn) grain boundaries in the coating; however, they do not propagate to the prior austenite grain boundaries (PAGBs) in the substrate, as the forming stress is not sufficiently high.

Jewer et al. [16] stated that robust cathodic corrosion protection was achieved for GI 2%Mn and 2.5%Mn PHS prototypes after austenitization times of 30 – 180 s at 890 °C for DHPF temperature of 700 °C (§2.8). The primary distinction between GI and GA is their microstructure caused by

the annealing step [8], [104], [105]. It is known that the transformation of a GI70 coating to Γ-Fe_3Zn_{10} is completed during heating of the coating to 700 °C, as shown in Figure 2.8 [50]. This transformation occurs more quickly for a GA coating, such as the coating for steel K. Thus, it can be said that the resultant quenched coating microstructure after DHPF is similar for both coatings. It was shown by XRD results (Figure 5.11) that greater than 36 vol% of Γ-Fe_3Zn_{10} was found in the coating for all DHPF temperatures tested. This can be attributed to the coating weight of 80 g/m^2/side for steel K. Higher coating weight indicates better corrosion protection as it yields a higher volume fraction of Γ-Fe_3Zn_{10} for a specific austenitization time and temperature. As stated earlier (§2.7), Γ-Fe_3Zn_{10} provides excellent cathodic corrosion protection, while α-Fe(Zn) offers barrier corrosion protection and poor cathodic corrosion protection. The thicker coating enhances the barrier corrosion protection by increasing the dissolution time for the coating [13], [16], [50]. Figure 6.3 is derived from images in Figure 5.10, and shows coating thickness as a function of DHPF temperature for austenitization at 890 °C for 120 s. It can be seen that the coating thickness almost doubled after DHPF. This implies that barrier corrosion protection was improved after DHPF. It should be noted that the coating thickness did not vary significantly as a function of DHPF temperature. Since coating thickness increases as a result of the diffusion of Zn into the substrate, austenitization parameters are expected to affect it more significantly [12], [50], [75].

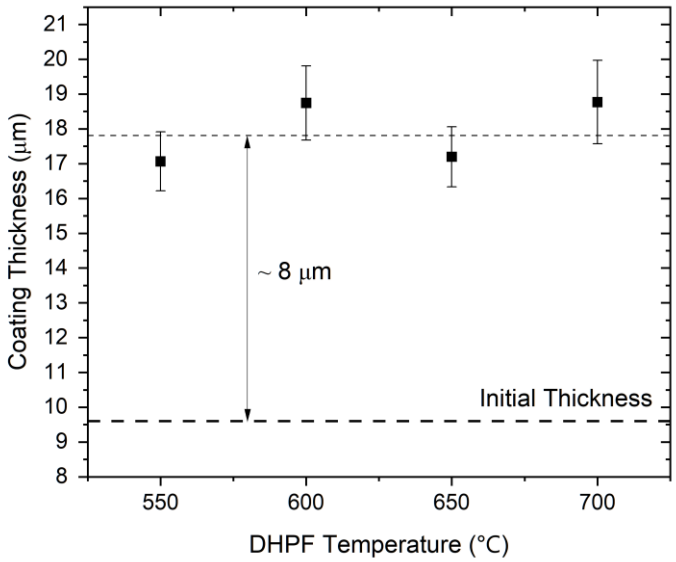

Figure 6.3: Coating thickness of steel K as a function of DHPF temperature for austenitization at 890 °C for 120 s.

Another implication of having a thicker coating is that the annealing time can be increased to ensure full austenitization, if needed. An increase in annealing time can be detrimental to cathodic corrosion protection in Zn-coated steel because it allows for Γ-Fe_3Zn_{10} to fully transform into α-Fe(Zn), increasing the total E_{corr} to a value closer to that of the substrate. As shown by Jewer. et al., an austenitization time of 180 s resulted in 10 vol% of Γ-Fe_3Zn_{10} for a coating weight of 75 g/m^2/side which would not yield robust cathodic corrosion protection [16].

Figure 6.4 summarizes the microstructural evolution of steel K after each processing step. It is shown that substrate starts with an equiaxed ferrite-pearlite microstructure. Upon austenitization, it fully transforms into austenite. After DHPF, the substrate consists of martensite and small amounts of ferrite (shown in red). The GA coating transforms into Γ-Fe_3Zn_{10} at 700 °C during heating. The Γ-Fe_3Zn_{10} eventually turns into a liquid Zn-Fe alloy prior to austenitization. Subsequently, α-Fe(Zn) and liquid Zn-Fe alloy are formed after austenitization. It is shown that

after transferring to the die and just before stamping, the liquid Zn in the coating fully solidifies, making Γ-Fe_3Zn_{10} by going through the Fe-Zn peritectic reaction. The α-Fe(Zn) grain boundary cracking in the coating occurs during this cooling step; however, it is not significant.

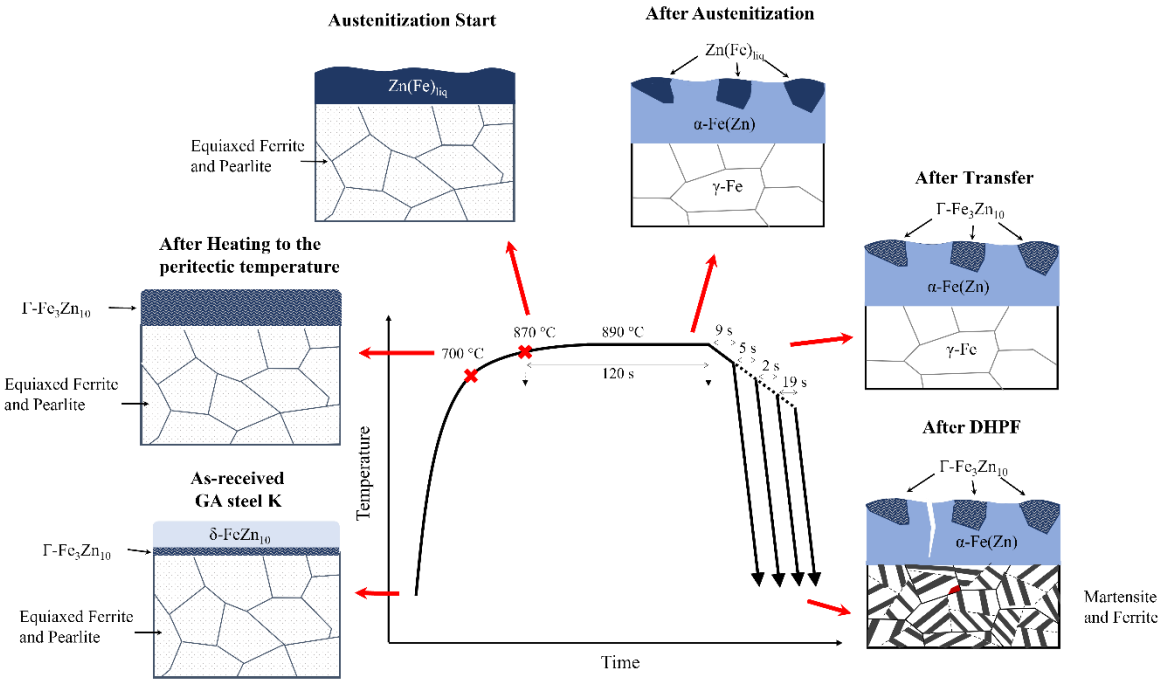

Figure 6.4: Summative schematic of the microstructural evolution of the coating and substrate after each processing step.

7 Conclusions and Future Work

7.1 Conclusions

Two prototype PHS grades with increased Mn contents and nominal compositions of 0.20C-1.96Mn-0.25Si-0.003B (wt.%, steel I) and 0.19C-1.92Mn-0.2Si-0.003B (wt.%, steel K) were considered for this study. Aiming to determine the feasibility of conducting DHPF at lower temperatures to avoid LME, their tensile properties at DHPF temperature of 650 °C were investigated. Based on their similar mechanical properties, namely similar tensile strengths and ductilities, and the GA coating on steel K, it was decided to conduct DHPF at various temperatures for steel K. In order to identify a suitable process window for steel K, the targets for this process were set as attaining fully martensitic microstructure in the substrate, which would yield UTS ≥ 1400 MPa, YS ≥ 1000 MPa; and more than 15 vol% of Γ-Fe_3Zn_{10} in the coating for robust cathodic corrosion protection. The most important conclusions are as follows:

1. The CCT diagram of steel I revealed a significant enhancement in hardenability due to the addition of Mn in comparison to 22MnB5. Furthermore, it was determined that a critical cooling rate of 10 °C/s is adequate for achieving a fully martensitic microstructure.

2. Laboratory-scale tensile testing for DHPF steel K revealed that the mechanical properties such as YS, UE and PUE, were not a strong function of the DHPF temperature. The UTS was similar for DHPF temperatures of 550 °C, 600 °C, and 650 °C, with the exact values of 1485 ± 29 MPa, 1480 ± 27 MPa, and 1501 ± 36 MPa, respectively. However, it decreased for the DHPF temperature of 700 °C to 1426 ± 22. Nonetheless, the targets of UTS ≥ 1400 MPa, and YS ≥ 1000 MPa were surpassed for all DHPF temperatures of 550°C – 700 °C. Furthermore, the substrate microstructure

of DHPF steel K for all DHPF temperatures consisted predominantly of martensite with small amounts of ferrite.

3. Tensile testing for the pilot-scale DHPF for steel K demonstrated that the previously specified targets for tensile strengths (UTS and YS) were met for all conditions including austenitization at 890 °C for 60 – 240 s and DHPF temperatures of 550 – 700 °C. Thus, indicating that DHPF of GA steel K at lower temperatures is industrially feasible and can provide desirable mechanical properties.

4. The coating microstructure for GA80-coated steel K did not change significantly as a function of DHPF temperature and exhibited Γ-Fe_3Zn_{10} phase fractions exceeding 15 vol.%. Thus, robust cathodic corrosion protection can be expected for DHPF GA80-coated steel K. Overall, promising corrosion properties including both barrier and cathodic corrosion protection are expected for steel K.

5. No evidence of LME or severe microcracking was detected for DHPF steel K. No microcracks propagating to the substrate were seen in the microstructure after DHPF temperatures of 550 – 700 °C. The high total elongation observed in tensile testing is a sign that catastrophic failure associated with LME has not occurred. Furthermore, SEM analysis of the tensile coupons provided evidence for ductile fracture.

6. In summary, a wide process window for DHPF at lower temperatures by extending the transfer time was determined for GA80-coated steel K. The target was to achieve a fully martensitic microstructure with UTS ≥ 1400 MPa, YS ≥ 1000 MPa; and more than 15 vol% of Γ-Fe_3Zn_{10} in the coating for robust cathodic corrosion protection while avoiding LME and microcracking. The process window for achieving all these targets

was an austenitization time 120 s at 890 °C and DHPF temperatures of 550–700 °C. In this window, LME was successfully avoided and microcracking was not severe. Furthermore, pilot-scale trials for steel K showed that using an extended transfer time is an industrially feasible robust process and can result in the target mechanical properties (YS and UTS) for austenitization times of 60-240 s and DHPF temperatures of 550-700 °C.

7.2 Future Work

The following recommendations are made to both improve this alloy and fully analyze all the aspects of industrial scaling of steel K.

- For the pilot-scale trials for steel K, comprehensive microstructural characterization can be conducted using SEM, OM with color etching, and XRD for both the top and side of the U-shaped part. This approach ensures a thorough examination of the microstructure, confirming the presence of martensite and other constituents at a larger scale.

- The corrosion properties for GA-coated steel K in the suggested process window must be investigated to ensure adequate corrosion protection. Potentiodynamic and galvanostatic polarization tests can be utilized to determine the driving force for cathodic protection and the corrosion kinetics. Moreover, accelerated cyclic corrosion tests (SAE J2334) could be employed to evaluate the performance of both the U-shaped part and the flat blank under accelerated corrosion conditions.

- In order to compare the formability of steel K to other commercially available PHS, bending tests such as VDA238-100 could be conducted.

- Further analysis can be conducted to gain a better understanding of the effect of the lower B content in comparison to 22MnB5, and to determine optimal amount of B in PHS. For instance, segregation of B to prior austenite grain boundaries could be analyzed using TEM and be related to ferrite nucleation.

- In order to achieve higher UTS values, the effect of increased carbon content for steel K can be studied and an optimal amount of carbon can be established. Increasing the UTS can further enhance passenger safety and promote vehicle lightweighting.

8 References

[1] H. Karbasian and A. E. Tekkaya, "A review on hot stamping," *Journal of Materials Processing Technology*, vol. 210, no. 15, pp. 2103–2118, Nov. 2010, doi: 10.1016/j.jmatprotec.2010.07.019.

[2] D. W. Fan and B. C. De Cooman, "State-of-the-Knowledge on Coating Systems for Hot Stamped Parts," *steel research int.*, vol. 83, no. 5, pp. 412–433, May 2012, doi: 10.1002/srin.201100292.

[3] M. Mikolaiczik, "2021 Mustang Mach-E," [Online]. Available: https://www.steel.org/wp-content/uploads/2021/06/GDIS-2021-_-Track-1_01_Mikolaiczik_Mustang-Mach-E-.pdf

[4] L. Dosdat, J. Petitjean, T. Vietoris, and O. Clauzeau, "Corrosion Resistance of Different Metallic Coatings on Press-Hardened Steels for Automotive," *steel research int.*, vol. 82, no. 6, pp. 726–733, Jun. 2011, doi: 10.1002/srin.201000291.

[5] D. W. Fan, H. S. Kim, and B. C. De Cooman, "A Review of the Physical Metallurgy related to the Hot Press Forming of Advanced High Strength Steel," *steel research international*, vol. 80, no. 3, pp. 241–248, 2009, doi: 10.2374/SRI08SP131.

[6] T. Taylor and A. Clough, "Critical review of automotive hot-stamped sheet steel from an industrial perspective," *Materials Science and Technology*, vol. 34, no. 7, pp. 809–861, May 2018, doi: 10.1080/02670836.2018.1425239.

[7] D. W. Fan, H. S. Kim, J.-K. Oh, K.-G. Chin, and B. C. D. Cooman, "Coating Degradation in Hot Press Forming," *ISIJ International*, vol. 50, no. 4, pp. 561–568, 2010, doi: 10.2355/isijinternational.50.561.

[8] E. Billur, Ed., *Hot Stamping of Ultra High-Strength Steels: From a Technological and Business Perspective*. Cham: Springer International Publishing, 2019. doi: 10.1007/978-3-319-98870-2.

[9] M. H. Razmpoosh, C. DiGiovanni, Y. N. Zhou, and E. Biro, "Pathway to understand liquid metal embrittlement (LME) in Fe-Zn couple: From fundamentals toward application," *Progress in Materials Science*, vol. 121, p. 100798, Aug. 2021, doi: 10.1016/j.pmatsci.2021.100798.

[10] B. C. De Cooman, W. jung, K. R. Jo, D. H. Sulistiyo, and L. Cho, "Zinc Liquid Metal Embrittlement of a High Strength Steel," presented at the Galvatech, 2017, pp. 790–795.

[11] H. Mohrbacher, "Martensitic Automotive Steel Sheet - Fundamentals and Metallurgical Optimization Strategies," *AMR*, vol. 1063, pp. 130–142, Dec. 2014, doi: 10.4028/www.scientific.net/AMR.1063.130.

[12] C. Dever, J. Kish, and J. McDermid, "Corrosion Properties of Hot Dip Galvanized Coatings on 22MnB5 Press Hardened Steels," in *GALVATECH 2017: 11th International Conference on Zinc and Zinc Alloy Coated Steel Sheet*, 2017.

[13] C. E. Dever, “Effect of Coating Microstructure on the Electrochemical Properties of Continuous Galvanized Coatings on Press Hardened Steels”.

[14] T. Kurz, P. Larour, J. Lackner, T. Steck, and G. Jesner, “Press-hardening of zinc coated steel - characterization of a new material for a new process,” *IOP Conf. Ser.: Mater. Sci. Eng.*, vol. 159, no. 1, p. 012025, Nov. 2016, doi: 10.1088/1757-899X/159/1/012025.

[15] C. Thomsen, J. R. McDermid, and F. Goodwin, “Development of a New Grade of Zinc-Coated Press-Hardenable Stee,” presented at the MS&T19, Portland, OR.

[16] J. D. L. Jewer, “THE EFFECT OF DIRECT HOT PRESS FORMING ON THE ELECTROCHEMICAL PROPERTIES OF NEXT GENERATION ZN-COATED PRESS HARDENABLE STEELS”.

[17] C. Thomsen, “DEVELOPMENT OF NEW GRADES OF ZINC COATED DIRECT PRESS-HARDENABLE STEEL WITH ROBUST CATHODIC PROTECTION”.

[18] Wang, B., “Modelling of Melt Flow and Solidification in the Twin-Roll Strip Casting Process,” *Steel Research International*, no. 80 (2009) No. 3 218-222, Mar. 2009, doi: 10.2374/SRI08SP131.

[19] G. Venturato, M. Novella, S. Bruschi, A. Ghiotti, and R. Shivpuri, “Effects of Phase Transformation in Hot Stamping of 22MnB5 High Strength Steel,” *Procedia Engineering*, vol. 183, pp. 316–321, Jan. 2017, doi: 10.1016/j.proeng.2017.04.045.

[20] R. A. Grange, “Effect of microstructural banding in steel,” *Metall Trans*, vol. 2, no. 2, pp. 417–426, Feb. 1971, doi: 10.1007/BF02663328.

[21] “Current Challenges and Opportunities in Microstructure-Related Properties of Advanced High-Strength Steels | SpringerLink.” https://link.springer.com/article/10.1007/s11661-020-05947-2 (accessed May 01, 2023).

[22] T. G. Digges, C. R. Irish, and N. L. Carwile, “Effect of boron on the hardenability of high-purity alloys and commercial steels,” *J. RES. NATL. BUR. STAN.*, vol. 41, no. 6, p. 545, Dec. 1948, doi: 10.6028/jres.041.043.

[23] M. Sharma, I. Ortlepp, and W. Bleck, “Boron in Heat-Treatable Steels: A Review,” *steel research international*, vol. 90, no. 11, p. 1900133, 2019, doi: 10.1002/srin.201900133.

[24] T. S. Prithiv *et al.*, “Austenite grain boundary segregation and precipitation of boron in low-C steels and their role on the heterogeneous nucleation of ferrite,” *Acta Materialia*, vol. 252, p. 118947, Jun. 2023, doi: 10.1016/j.actamat.2023.118947.

[25] T. Taylor, G. Fourlaris, and A. Clough, “Effect of carbon and microalloy additions on hot-stamped boron steel,” *Materials Science and Technology*, vol. 33, no. 16, pp. 1964–1977, Nov. 2017, doi: 10.1080/02670836.2017.1342018.

[26] R. C. Sharma and G. R. Purdy, "Nucleation limitation and hardenability," *Metall Trans B*, vol. 5, no. 4, pp. 939–947, Apr. 1974, doi: 10.1007/BF02643152.

[27] B. Hwang, D.-W. Suh, and S.-J. Kim, "Austenitizing temperature and hardenability of low-carbon boron steels," *Scripta Materialia*, vol. 64, no. 12, pp. 1118–1120, Jun. 2011, doi: 10.1016/j.scriptamat.2011.03.003.

[28] A. R. Marder, "The metallurgy of zinc-coated steel," *Progress in Materials Science*, vol. 45, no. 3, pp. 191–271, Jun. 2000, doi: 10.1016/S0079-6425(98)00006-1.

[29] E. A. Silva, "Private Communications," 2005.

[30] S. Alibeigi, R. Kavitha, R. J. Meguerian, and J. R. McDermid, "Reactive wetting of high Mn steels during continuous hot-dip galvanizing," *Acta Materialia*, vol. 59, no. 9, pp. 3537–3549, May 2011, doi: 10.1016/j.actamat.2011.02.027.

[31] J. R. McDermid, M. H. Kaye, and W. T. Thompson, "Fe Solubility in the Zn-Rich Corner of the Zn-Al-Fe System for Use in Continuous Galvanizing and Galvannealing," *Metall Mater Trans B*, vol. 38, no. 2, pp. 215–230, Apr. 2007, doi: 10.1007/s11663-007-9028-3.

[32] E. Baril and G. L'Espérance, "Studies of the morphology of the Al-rich interfacial layer formed during the hot dip galvanizing of steel sheet," *Metall Mater Trans A*, vol. 30, no. 13, pp. 681–695, Mar. 1999, doi: 10.1007/s11661-999-1000-1.

[33] B. Çetin and H. Meço, "Metallurgy of Steels," in *Hot Stamping of Ultra High-Strength Steels: From a Technological and Business Perspective*, E. Billur, Ed., Cham: Springer International Publishing, 2019, pp. 19–29. doi: 10.1007/978-3-319-98870-2_2.

[34] C. W. Lee, D. W. Fan, I. R. Sohn, S.-J. Lee, and B. C. De Cooman, "Liquid-Metal-Induced Embrittlement of Zn-Coated Hot Stamping Steel," *Metall Mater Trans A*, vol. 43, no. 13, pp. 5122–5127, Dec. 2012, doi: 10.1007/s11661-012-1316-0.

[35] R. Neugebauer *et al.*, "Press hardening-An innovative and challenging technology," *Archiv.Civ.Mech.Eng*, vol. 12, no. 2, pp. 113–118, Jun. 2012, doi: 10.1016/j.acme.2012.04.013.

[36] M. Tisza, "Hot Forming of Boron Alloyed Manganese Steels," *Materials Science Forum*, vol. 885, pp. 25–30, 2017, doi: 10.4028/www.scientific.net/MSF.885.25.

[37] Y. Chang, Z. Meng, L. Ying, X. Li, N. Ma, and P. Hu, "Influence of Hot Press Forming Techniques on Properties of Vehicle High Strength Steels," *Journal of Iron and Steel Research, International*, vol. 18, no. 5, pp. 59–63, May 2011, doi: 10.1016/S1006-706X(11)60066-6.

[38] M. Nikravesh, M. Naderi, G. H. Akbari, and W. Bleck, "Phase transformations in a simulated hot stamping process of the boron bearing steel," *Materials & Design*, vol. 84, pp. 18–24, Nov. 2015, doi: 10.1016/j.matdes.2015.06.108.

[39] C. Allély, L. Dosdat, O. Clauzeau, K. Ogle, and P. Volovitch, "Anticorrosion mechanisms of aluminized steel for hot stamping," *Surface and Coatings Technology*, vol. 238, pp. 188–196, Jan. 2014, doi: 10.1016/j.surfcoat.2013.10.072.

[40] R. W. Richards, R. D. Jones, P. D. Clements, and H. Clarke, "Metallurgy of continuous hot dip aluminizing," *International Materials Reviews*, vol. 39, no. 5, pp. 191–212, Jan. 1994, doi: 10.1179/imr.1994.39.5.191.

[41] M. Windmann, A. Röttger, and W. Theisen, "Formation of intermetallic phases in Al-coated hot-stamped 22MnB5 sheets in terms of coating thickness and Si content," *Surface and Coatings Technology*, vol. 246, pp. 17–25, May 2014, doi: 10.1016/j.surfcoat.2014.02.056.

[42] F. Jenner, M. E. Walter, R. Mohan Iyengar, and R. Hughes, "Evolution of Phases, Microstructure, and Surface Roughness during Heat Treatment of Aluminized Low Carbon Steel," *Metall Mater Trans A*, vol. 41, no. 6, pp. 1554–1563, Jun. 2010, doi: 10.1007/s11661-009-0105-x.

[43] R. Grigorieva, P. Drillet, J. M. Mataigne, and A. Redjaïmia, "Phase Transformations in the Al-Si Coating during the Austenitization Step," *SSP*, vol. 172–174, pp. 784–790, Jun. 2011, doi: 10.4028/www.scientific.net/SSP.172-174.784.

[44] M. Shehryar Khan *et al.*, "The influence of in-situ alloying of electro-spark deposited coatings on the multiscale morphological and mechanical properties of laser welded Al–Si coated 22MnB5," *Materials Science and Engineering: A*, vol. 839, p. 142830, Apr. 2022, doi: 10.1016/j.msea.2022.142830.

[45] K. R. Jo, L. Cho, D. H. Sulistiyo, E. J. Seo, S. W. Kim, and B. C. De Cooman, "Effects of Al-Si coating and Zn coating on the hydrogen uptake and embrittlement of ultra-high strength press-hardened steel," *Surface and Coatings Technology*, vol. 374, pp. 1108–1119, Sep. 2019, doi: 10.1016/j.surfcoat.2019.06.047.

[46] P. Pokorny, J. Kolisko, L. Balik, and P. Novak, "Description of structure of Fe-Zn intermetalic compounds present in hot-dip galvanized coatings on steel," *Metalurgija*, vol. 54, no. 4, pp. 707–710, Oct. 2015.

[47] S. Dionne, "The characterization of continuous hot-dip galvanized and galvannealed steels," *JOM*, vol. 58, no. 3, pp. 32–40, Mar. 2006, doi: 10.1007/s11837-006-0157-y.

[48] K. Han, I. Ohnuma, K. Okuda, and R. Kainuma, "Experimental determination of phase diagram in the Zn-Fe binary system," *Journal of Alloys and Compounds*, vol. 737, pp. 490–504, Mar. 2018, doi: 10.1016/j.jallcom.2017.11.320.

[49] H. Kang, L. Cho, C. Lee, and B. C. De Cooman, "Zn Penetration in Liquid Metal Embrittled TWIP Steel," *Metall and Mat Trans A*, vol. 47, no. 6, pp. 2885–2905, Jun. 2016, doi: 10.1007/s11661-016-3475-x.

[50] R. Autengruber, G. Luckeneder, S. Kolnberger, J. Faderl, and A. W. Hassel, "Surface and Coating Analysis of Press-Hardened Hot-Dip Galvanized Steel Sheet," *steel research international*, vol. 83, no. 11, pp. 1005–1011, 2012, doi: 10.1002/srin.201200068.

[51] K. Maleki, D. M. Pallisco, J. R. McDermid, and N. D. Bassim, "On the origin of micro-cracking in zinc-coated press hardened steels," *Surface and Coatings Technology*, vol. 437, p. 128360, May 2022, doi: 10.1016/j.surfcoat.2022.128360.

[52] C. F. Old and P. Trevena, "Reaction in copper-lithium system and its implications for liquid-metal embrittlement," *Metal Science*, vol. 15, no. 7, pp. 281–286, Jul. 1981, doi: 10.1179/030634581790426778.

[53] M. G. Nicholas and C. F. Old, "Liquid metal embrittlement," *J Mater Sci*, vol. 14, no. 1, pp. 1–18, Jan. 1979, doi: 10.1007/BF01028323.

[54] M. H. Kamdar, "The occurrence of liquid-metal embrittlement," *physica status solidi (a)*, vol. 4, no. 1, pp. 225–233, 1971, doi: 10.1002/pssa.2210040123.

[55] B. Joseph, M. Picat, and F. Barbier, "Liquid metal embrittlement: A state-of-the-art appraisal," *The European Physical Journal - Applied Physics*, vol. 5, no. 1, pp. 19–31, Jan. 1999, doi: 10.1051/epjap:1999108.

[56] A. R. C. Westwood and M. H. Kamdar, "Concerning liquid metal embrittlement, particularly of zinc monocrystals by mercury," *The Philosophical Magazine: A Journal of Theoretical Experimental and Applied Physics*, vol. 8, no. 89, pp. 787–804, May 1963, doi: 10.1080/14786436308213836.

[57] S. P. Lynch, "Mechanisms and Kinetics of Environmentally Assisted Cracking: Current Status, Issues, and Suggestions for Further Work," *Metall Mater Trans A*, vol. 44, no. 3, pp. 1209–1229, Mar. 2013, doi: 10.1007/s11661-012-1359-2.

[58] L. Cho, H. Kang, C. Lee, and B. C. De Cooman, "Microstructure of liquid metal embrittlement cracks on Zn-coated 22MnB5 press-hardened steel," *Scripta Materialia*, vol. 90–91, pp. 25–28, Nov. 2014, doi: 10.1016/j.scriptamat.2014.07.008.

[59] C. Béal, "Mechanical behaviour of a new automotive high manganese TWIP steel in the presence of liquid zinc," These de doctorat, Lyon, INSA, 2011. Accessed: May 09, 2023. [Online]. Available: https://www.theses.fr/2011ISAL0029

[60] P. J. L. Fernandes and D. R. H. Jones, "Mechanisms of liquid metal induced embrittlement," *International Materials Reviews*, vol. 42, no. 6, pp. 251–261, Nov. 1997, doi: 10.1179/imr.1997.42.6.251.

[61] K. Wolski and V. Laporte, "Grain boundary diffusion and wetting in the analysis of intergranular penetration," *Materials Science and Engineering: A*, vol. 495, no. 1, pp. 138–146, Nov. 2008, doi: 10.1016/j.msea.2007.10.107.

[62] W. Rostoker, J. M. McCaughey, and H. Markus, "Embrittlement by Liquid Metals," *Reinhold Publ. Corp.*, 1960.

[63] N. V. Pertsov and P. A. Rebinder, "Surface activity of liquid metal coatings and their influence on the strength of metals," in *Doklady Akademii Nauk*, Russian Academy of Sciences, 1958, pp. 1068–1070.

[64] X. Su, N.-Y. Tang, and J. M. Toguri, "450 °C Isothermal Section of the Fe-Zn-Si Ternary Phase Diagram," *Canadian Metallurgical Quarterly*, vol. 40, no. 3, pp. 377–384, Jan. 2001, doi: 10.1179/cmq.2001.40.3.377.

[65] S. Kobayashi, "Effects of Si Solid Solution in Fe Substrate on the Alloying Reaction between Fe Substrate and Liquid Zn," *ISIJ International*, vol. 57, no. 12, pp. 2214–2219, 2017, doi: 10.2355/isijinternational.ISIJINT-2017-410.

[66] K.-C. Lin and C.-S. Lin, "Effect of Silicon in Dual Phase Steel on the Alloy Reaction in Continuous Hot-dip Galvanizing and Galvannealing," *ISIJ International*, vol. 54, no. 10, pp. 2380–2384, 2014, doi: 10.2355/isijinternational.54.2380.

[67] S. Kobayashi, "Effects of Si on the formation of intermetallic phases in alloying reaction between iron substrate and liquid Zn containing 0.2 wt% Al," *SN Appl. Sci.*, vol. 1, no. 1, p. 61, Nov. 2018, doi: 10.1007/s42452-018-0065-0.

[68] J. Wang, X. Su, F. Yin, Z. Li, and M. Zhao, "The 480°C and 405°C isothermal sections of the phase diagram of Fe–Zn–Si ternary system," *Journal of Alloys and Compounds*, vol. 399, no. 1, pp. 214–218, Aug. 2005, doi: 10.1016/j.jallcom.2005.03.043.

[69] D. Bhattacharya *et al.*, "Liquid metal embrittlement susceptibility of two Zn-Coated advanced high strength steels of similar strengths," *Materials Science and Engineering: A*, vol. 823, p. 141569, Aug. 2021, doi: 10.1016/j.msea.2021.141569.

[70] T. Auger, J.-B. Vogt, and I. P. Serre, "Liquid metal embrittlement," in *Mechanics - Microstructure - Corrosion Coupling: Concepts, Experiments, Modeling and Cases*, 2019, pp. 507–534. doi: 10.1016/B978-1-78548-309-7.50022-3.

[71] M. H. Razmpoosh, A. Macwan, F. Goodwin, E. Biro, and Y. Zhou, "Role of Random and Coincidence Site Lattice Grain Boundaries in Liquid Metal Embrittlement of Iron (FCC)-Zn Couple," *Metall Mater Trans A*, vol. 51, no. 8, pp. 3938–3944, Aug. 2020, doi: 10.1007/s11661-020-05857-3.

[72] B. Straumal and B. Baretzky, "Grain Boundary Phase Transitions and their Influence on Properties of Polycrystals," *Interface Science*, vol. 12, no. 2, pp. 147–155, Apr. 2004, doi: 10.1023/B:INTS.0000028645.30358.f5.

[73] G. Jung, I. S. Woo, D. W. Suh, and S.-J. Kim, "Liquid Zn assisted embrittlement of advanced high strength steels with different microstructures," *Met. Mater. Int.*, vol. 22, no. 2, pp. 187–195, Mar. 2016, doi: 10.1007/s12540-016-5579-7.

[74] Ahmadian *et al.*, "Interstitial Segregation has the Potential to Mitigate Liquid Metal Embrittlement in Iron," *Advanced Materials*, p. 2211796, Apr. 2023, doi: 10.1002/adma.202211796.

[75] V. Janik, Y. Lan, P. Beentjes, D. Norman, G. Hensen, and S. Sridhar, "Zn Diffusion and α-Fe(Zn) Layer Growth During Annealing of Zn-Coated B Steel," *Metall and Mat Trans A*, vol. 47, no. 1, pp. 400–411, Jan. 2016, doi: 10.1007/s11661-015-3203-y.

[76] H. Järvinen, S. Järn, E. Lepikko, M. Järvenpää, and P. Peura, "ZnFe Coated 22MnB5 Steels in Direct Press Hardening: The Relationships between Coating Structure and Process Parameters," *Key Engineering Materials*, vol. 674, pp. 331–336, 2016, doi: 10.4028/www.scientific.net/KEM.674.331.

[77] H.-H. Seok, J.-C. Mun, and C. Kang, "Micro-crack in zinc coating layer on boron steel sheet in hot deep drawing process," *Int. J. Precis. Eng. Manuf.*, vol. 16, no. 5, pp. 919–927, May 2015, doi: 10.1007/s12541-015-0120-3.

[78] T. Kurz, G. Luckeneder, T. Manzenreiter, H. Schwinghammer, and A. Sommer, "Zinc Coated Press-Hardening Steel - Challenges and Solutions," presented at the SAE 2015 World Congress & Exhibition, Apr. 2015, pp. 2015-01–0565. doi: 10.4271/2015-01-0565.

[79] K. Isaksson, M. Jönsson, and D. Berglund, "The Direct Press Hardening Process for Zn-Coated Ultra-High Strength Steels," in *Advanced High Strength Steel and Press Hardening*, WORLD SCIENTIFIC, 2016, pp. 556–563. doi: 10.1142/9789813140622_0089.

[80] K. Hu, S. Zhou, R. Han, J. Gao, and Y. Yang, "Microstructure Evolution and Simulation in 22MnB5 Steel during Hot Stamping," *Journal of Materials Science and Chemical Engineering*, vol. 6, no. 8, Art. no. 8, Aug. 2018, doi: 10.4236/msce.2018.68002.

[81] C.-K. ChiuHuang, S.-W. Wang, and P.-K. Lee, "Investigation of the influence of forming parameters on the springback of hot-stamped hat-shaped parts," *IOP Conf. Ser.: Mater. Sci. Eng.*, vol. 651, no. 1, p. 012029, Nov. 2019, doi: 10.1088/1757-899X/651/1/012029.

[82] S. P. Lynch, "Solid-metal-induced embrittlement of aluminium alloys and other materials," *Materials Science and Engineering: A*, vol. 108, pp. 203–212, Feb. 1989, doi: 10.1016/0921-5093(89)90421-8.

[83] J. C. Lynn, W. R. Warke, and P. Gordon, "Solid metal-induced embrittlement of steel," *Materials Science and Engineering*, vol. 18, no. 1, pp. 51–62, Mar. 1975, doi: 10.1016/0025-5416(75)90072-5.

[84] K. Sadananda and A. K. Vasudevan, "Review of Environmentally Assisted Cracking," *Metall Mater Trans A*, vol. 42, no. 2, pp. 279–295, Feb. 2011, doi: 10.1007/s11661-010-0472-3.

[85] S. P. Lynch, "Metal-induced embrittlement of materials," *Materials Characterization*, vol. 28, no. 3, pp. 279–289, Apr. 1992, doi: 10.1016/1044-5803(92)90017-C.

[86] K. Maleki, “On the Origin of Micro-Cracking in Zn-Coated Press Hardened Steels,” McMaster, 2019.

[87] C. W. Lee, W. S. Choi, L. Cho, Y. R. Cho, and B. C. D. Cooman, “Liquid-Metal-Induced Embrittlement Related Microcrack Propagation on Zn-coated Press Hardening Steel,” *ISIJ International*, vol. 55, no. 1, pp. 264–271, 2015, doi: 10.2355/isijinternational.55.264.

[88] M. Pouranvari and S. P. H. Marashi, “Critical review of automotive steels spot welding: process, structure and properties,” *Science and Technology of Welding and Joining*, vol. 18, no. 5, pp. 361–403, Jul. 2013, doi: 10.1179/1362171813Y.0000000120.

[89] S. Fajardo, I. Llorente, J. A. Jiménez, J. M. Bastidas, and D. M. Bastidas, “Effect of Mn additions on the corrosion behaviour of TWIP Fe-Mn-Al-Si austenitic steel in chloride solution,” *Corrosion Science*, vol. 154, pp. 246–253, Jul. 2019, doi: 10.1016/j.corsci.2019.04.026.

[90] H. E. Townsend, “Effects of Alloying Elements on the Corrosion of Steel in Industrial Atmospheres,” *Corrosion*, vol. 57, no. 06, Jun. 2001.

[91] E01 Committee, “Test Methods for Determination of Carbon, Sulfur, Nitrogen, and Oxygen in Steel, Iron, Nickel, and Cobalt Alloys by Various Combustion and Fusion Techniques,” ASTM International. doi: 10.1520/E1019-18.

[92] E01 Committee, “Guide for Determination of Various Elements by Direct Current Plasma Atomic Emission Spectrometry,” ASTM International. doi: 10.1520/E1097-12.

[93] E01 Committee, “Practice for Describing and Specifying Inductively-Coupled Plasma Atomic Emission Spectrometers,” ASTM International. doi: 10.1520/E1479-16.

[94] E28 Committee, “Test Methods for Tension Testing of Metallic Materials,” ASTM International. doi: 10.1520/E0008_E0008M-13A.

[95] E28 Committee, “Test Method for Plastic Strain Ratio r for Sheet Metal,” ASTM International. doi: 10.1520/E0517-19.

[96] E28 Committee, “Test Method for Tensile Strain-Hardening Exponents (n -Values) of Metallic Sheet Materials,” ASTM International. doi: 10.1520/E0646-16.

[97] P. Belanger, “Private communication,” Gestamp, 2022.

[98] P. K. Gallagher, M. E. Brown, and R. B. Kemp, Eds., *Handbook of thermal analysis and calorimetry*. Amsterdam [Netherlands] ; New York: Elsevier, 1998.

[99] R. Abbaschian, L. Abbaschian, and R. E. Reed-Hill, *Physical metallurgy principles*, 4th ed. Stamford, CT: Cengage Learning, 2009.

[100] D. P. Koistinen and R. E. Marburger, "A general equation prescribing the extent of the austenite-martensite transformation in pure iron-carbon alloys and plain carbon steels," *Acta Metallurgica*, vol. 7, no. 1, pp. 59–60, Jan. 1959, doi: 10.1016/0001-6160(59)90170-1.

[101] S. P. Murugan *et al.*, "Role of liquid Zn and α-Fe(Zn) on liquid metal embrittlement of medium Mn steel: An ex-situ microstructural analysis of galvannealed coating during high temperature tensile test," *Surface and Coatings Technology*, vol. 398, p. 126069, Sep. 2020, doi: 10.1016/j.surfcoat.2020.126069.

[102] M. S. Masete, N. S. Muchavi, and S. Chikosha, "The effect of specimen geometry on tensile properties of titanium alloy metal sheet.," *IOP Conf. Ser.: Mater. Sci. Eng.*, vol. 430, p. 012015, Oct. 2018, doi: 10.1088/1757-899X/430/1/012015.

[103] "EN ISO 6892-1:2019—Metallic materials—Tensile testing—Part 1: Method of test at room temperature," Brussels, Belgium, ISO 6892-1, 2019.

[104] P. Gogola, Z. Gabalcová, M. Kusý, and J. Ptačinová, "High-Temperature Behaviour of Zn-Based Galvannealed Coatings on Steel," *Materials*, vol. 16, no. 9, Art. no. 9, Jan. 2023, doi: 10.3390/ma16093341.

[105] J. Faderl, "CHS2 2011 Conference Proceedings: Hot Sheet Metal Forming of High-Performance Steel," presented at the CHS2 2009 Conference Proceedings, Luleå, Sweden, Jun. 2009.